Investigation of mechanisms affecting tool surface during electrochemical machining

Dissertation

zur Erlangung des Grades
des Doktors der Ingenieurwissenschaften
der Naturwissenschaftlich-Technischen Fakultät
der Universität des Saarlandes

von

Mandana Ghasemiansafaei

Saarbrücken, 2023

Abstract

Electrochemical machining (ECM) is a very important technology in the machining of difficult-to-cut materials. Pulsed electrochemical machining (PECM) is a variant of ECM that employs a pulsed voltage at high current density. PECM improves the control of the machining process when compared with direct current ECM. The contactless nature of ECM and PECM by the anodic dissolution of the workpiece propound no tool ablation. Nevertheless, in a few studies, tool damages, namely the formation of pits and geometrical changes, have been observed. The reason for these damages was not fully and properly investigated until now, which turns out to be the objective of investigation in this work. This study considers three hypotheses to research the tool changes during PECM and ECM: Hydrogen embrittlement, cavitation erosion, and cathodic corrosion. A systematic study of monitoring possible changes at martensitic stainless steel 1.4112 tool during ECM and PECM in aqueous $NaNO_3$ electrolyte is performed. Experimental results of this study show that hydrogen embrittlement and cavitation erosion are not the reason for causing changes on the tool. It is identified for the first time that cathodic corrosion is the possible mechanism of causing the changes on the tool in this study. The approach is investigating microstructure before and after the process, as microstructure can store information regarding phenomena happening during the process.

Kurzzusammenfassung

Die elektrochemische Bearbeitung (ECM) ist eine sehr wichtige Technologie für die Bearbeitung von schwer zerspanbaren Materialien. Die gepulste elektrochemische Bearbeitung (PECM) ist eine Variante der ECM, bei der eine gepulste Spannung mit hoher Stromdichte verwendet wird. PECM verbessert die Steuerung des Bearbeitungsprozesses im Vergleich zur Gleichstrom-ECM. Die berührungslose Natur von ECM und PECM durch die anodische Auflösung des Werkstücks bedingt keinen Werkzeugabtrag. Dennoch wurden in einigen Studien Werkzeugschäden, nämlich die Bildung von Pits und geometrische Veränderungen, beobachtet. Der Grund für diese Schäden ist bisher noch nicht vollständig und angemessen untersucht worden, was sich als Ziel der Untersuchung in dieser Arbeit herausstellt. In dieser Studie werden drei Hypothesen zur Erforschung der Werkzeugveränderungen während der PECM und ECM aufgestellt, welche wie folgt lauten: Wasserstoffversprödung, Kavitationserosion und kathodische Korrosion. Es wird eine systematische Studie zur Überwachung möglicher Werkzeugveränderungen bei martensitischem rostfreiem Stahl 1.4112 während der ECM- und PECM-Bearbeitung in wässrigem $NaNO_3$-Elektrolyten durchgeführt. Die experimentellen Ergebnisse dieser Studie zeigen, dass Wasserstoffversprödung und Kavitationserosion nicht die Ursache für Veränderungen am Werkzeug sind. In dieser Studie wird zum ersten Mal festgestellt, dass kathodische Korrosion der mögliche Mechanismus ist, der die Veränderungen am Werkzeug verursacht. Der Ansatz in dieser Studie ist die Untersuchung der Mikrostruktur hinsichtlich verschiedener Aspekte vor und nach dem Prozess, da die Mikrostruktur Informationen, über die während des Prozesses auftretenden Phänomene speichern kann.

Acknowledgments

Publications

Parts of this work have been published as follows:

Ghasemiansafaei, M; Güner, M.; Schäfer, F.; Zeiner, M.; Bähre, D.
Detection of hydrogen in cathode tool during pulse electrochemical machining, Proceedings of the 16th International Symposium on Electrochemical Machining Technology, pp. 21-26, ISBN 978-3-95735-125-8, Chemnitz (Germany), November 24-25, 2020.

Ghasemiansafaei, M; Schäfer, F.; Bähre, D.
Investigation on parameters affecting tool during pulse electrochemical machining, Proceedings of the 18th International Symposium on Electrochemical Machining Technology, pp. 109-115, ISBN 978-4-915698-21-7, Tokyo (Japan), November 14-15, 2022.

Ghasemiansafaei, M.; Schäfer, F.; Hall, T.; Bähre, D.
Analysis of mechanisms affecting the tool in pulsed electrochemical machining, Journal of The Electrochemical Society, vol. 170, no. 6, p. 063504, 2023.

List of Content

LIST OF ABBREVIATIONS

AFM	Atomic Force Microscopy
BCC	Body Center Cubic
CAD	Computer Aided Design
CE	Counter electrode
CFD	Computational Fluid Dynamics
COD	Crystallography Open Database
CP	Cyclic Polarization
CPD	Contact Potential Difference
DC	Direct Current
DIN	Deutsches Institut für Normung
EBM	Electron Beam Machining
EBSD	Electron Backscatter Diffraction
ECM	Electrochemical Machining
EDM	Electro Discharge Machining
EDS	Energy Dispersive X-Ray Spectroscopy
IEG	Inter Electrode Gap
FCC	Face Center Cubic
FESEM	Field Emission Scanning Electron Microscope
HCP	Hexagonal Close pack
JCPDS	Joint Committee on Powder
KAM	Diffraction Standards
LBM	Kernel Average Misorientation
MRR	Laser Beam Machining
PECM	Mass Removal Rate
PEP	Pulse Electrochemical Machining
PLA	Paralloy Ethylene Profiled
PVC	Polylactic Acid
Re	Polyvinyl Chloride
SCE	Reference electrode
SE	Saturated Calomel Electrode
SKPFM	Secondary Electron Scanning Kelvin

	Probe Force Microscopy
SMR	Specific Mass Removal
TDS	Thermal Desorption Spectroscopy
USM	Ultrasonic Machining
WE	Working Electrode
XRD	X-Ray Diffraction

List of Symbols

Symbol	Definition	Unit
A	Area	mm^2
A$^+$/A	Alkali metal cation/ Alkali metal	
Ag	Silver	
Al	Aluminum	
As	Arsenic	
Au	Gold	
b_i	Charge number	
Bi	Bismuth	
C	Carbide	
c_i	Concentration of each ion	M
Ca	Calcium	
Cr	Chromium	
$Cr_2O_7^{2-}$	Dichromate	
$Cr_{23}C_6$	Chromium carbide	
Cu	Copper	
D	Diffusion coefficient	cm^2/s
$\vec{D}$	Vector of electric displacement	C/m^2
e	Electron	
E	Electrode potential	V
E	equivalent weight	
$\vec{E}$	Vector of electric field	V/m
E$_{corr.}$	Corrosion potential	V
E$_{eq}$	Equilibrium potential	V
Et	Ethyl group	
f	Pulse frequency	Hz
f$_{mechanic}$	Mechanical frequency	Hz
f$_{electric}$	Electrical frequency	
F	Faraday constant (= 96.485,3365)	As/mol
F	Volume force	N/m^3
Fe	Iron	

Symbol	Definition	Unit
Ga	Gallium	
H	Hydrogen	
H^+	Proton	
$H_2\uparrow$	Gaseous hydrogen	
HCl	Hydrochloric acid	
HF	Hydrofluoric acid	
Hg	Mercury	
Hg_2Cl_2	Mercury(I) chloride	
H_2O	Water	
h	Removal height	mm
I(t)	Current in time t	A
I	Identity matrix in fluid equation	
In	Indium	
Ir	Iridium	
J	Current Density	A/mm^2
$\vec{J}$	Vector of current density	A/mm^2
$\vec{J}_e$	External vector of current density	A/mm^2
K	Specific resistance electrolyte	Ωcm
KCl	Potassium chloride	
Li	Lithium	
m	Mass of elements	mg
M	Molar mass	g/mol
Me	Metal atom	
Me	Methyl group	
Me^{n+}	n times positively charged metal cation	
$Me(OH)_n\downarrow$	Insoluble metal hydroxide compound	
Mg	Magnesium	
Mn	Manganese	
Mo	Molybdenum	
MRR	Mass removal rate	cm^3/C
n	Amount of transferred electron	
Na	Sodium	

Symbol	Definition	Unit
NaBr	Sodium bromide	
NaCl	Sodium chloride	
$NaClO_3$	Sodium chlorate	
NaF	Sodium fluoride	
$NaNO_3$	Sodium nitrate	
NaOH	Sodium hydroxide	
Nb	Niobium	
Ni	Nickel	
NO_2^-	Nitrite	
NO_3^-	Nitrate	
O	Oxygen	
$O_2\uparrow$	Gaseous oxygen	
$\dot{Q}$	Generated heat	J
P	Phosphorus	
P	Pressure of electrolyte	N/m^2
Pd	Palladium	
Pb	Lead	
Pt	Platinum	
r_i	Radius of the ion	pm
R	Resistance	Ω
R	Organic material	
Re	Rhenium	
Rh	Rhodium	
Ru	Ruthenium	
s	Distance between electrodes	µm
S	Sulfur	
S_x	Initial IEG	µm
Sb	Antimony	
Si	Silicon	
SMR	Specific mass removal	mg/C
Sn	Tin	
t	Time	ms
t_{off}	Pulse pause	ms

Symbol	Definition	Unit
t_{on}	Pulse width	ms
T	Temperature	°C
T_0	Initial temperature	°C
Ta	Tantalum	
Ti	Titanium	
Tl	Thallium	
Q	Charge	C
u	velocity	m/s
u_i	Mobility of the ion	m^2/V s
U	Voltage	V
v	removal rate	mm/s
V	Volume removal	mm^3
V	Vanadium	
V_{CPD}	Contact potential difference	V
v_f	Feed rate	mm/min
W	Tungsten	
WC	Tungsten carbide	
Z	Electrochemical equivalent of the substance	mg/C
$Z_k(t)$	Cathode position in time t	mm
$Z_v(t)$	Vibrator position in time t	mm
$Z_i . e$	Charge number	
η or η_{ac}	Activation or overpotential	V
ρ	Density	g/mm³
ρ	Local electric charge density	C/m^3
σ	Conductivity of electrolyte	mS/cm
σ_0	Initial conductivity	mS/cm
μ	Solution viscosity	kg/m s
β	Temperature coefficient	1/K
$\vec{\nabla} .$	Vector of divergence	
ε_0	Electric field constant	
ε_r	Material-dependent relative permittivity	
ϕ	Work function	eV
ϕ_S	Work function of the sample	eV

Symbol	Definition	Unit
ϕ_T	Work function of the tip	eV

List of Figures

List of Tables

1 Introduction

In the competitive industry, efficient manufacturing processes by considering the minimum costs and the maximum quality of the finished product attract attention. Regarding the product material and the application, the manufacturing process is designed. Among the most complex industrial products, aero engines are in growing demand in the aviation industry. For instance, Rolls-Royce is expecting 68,000 deliveries between 2012-2031 [1]. In this industry, a product with higher reliability, longer service life, higher fuel efficiency, and clean and quiet operation with complex geometry will survive. Consequently, machining accuracy and surface quality are of high importance. Recently, many unconventional manufacturing processes like electrochemical machining (ECM), electro-discharge machining (EDM), laser beam machining (LBM), electron beam machining (EBM), and ultrasonic machining (USM) are widely used in the aviation industry. No tool wear, machining efficiency, and high finish surface quality make ECM a pioneering process in machining hard materials with complex shapes [1]. ECM is not only used in the aviation industry but also in automotive constriction, medical equipment, micro systems, and the power supply industry [2].

ECM originated from electrolytic polishing in 1911 by a Russian chemist E. Shiptalsky. The ECM process was developed in Russia in 1928 by Russian engineers V.N. Gusev and L. Rozhkov for the first time but did not get famous. One reason was that other machining methods were functional for materials available in that era [3]. In 1959, The Anocut Engineering Company in the USA introduced the traditional model of ECM using the direct current. In 1960-1970s, more research was done in the ECM field, and it was used in western Europe and USSR for gas turbine production and tool manufacturing for forging dies. At this time, the development in EDM slowed down ECM research and development. In 1980-1990s, the scheme of impulse and impulse-cyclic processing in passivating oxygen-containing electrolytes was developed, lowering errors in the process and the final surface roughness. At this time, the demand for hard materials in the aerospace, medical, and tool machining industry was increasing, and traditional manufacturing processes were inefficient. The demand for the ECM process became apparent from 1998-2011 by increasing the accuracy with the help of pulse electrochemical machining (PECM). Nowadays, PECM is used by many companies [4, 5].

During ECM and PECM, there is no tool wear due to no contact between the tool and the workpiece. As a result, most studies in this field focus on workpiece condition and process optimization. Observing and investigating the tool damages become the motivation in this study which is explained in chapter 2.2.1.

This work aims to help have a better understanding of the tool during ECM and PECM to find the mechanisms damaging the tool. After reviewing the literature in research and technology as well as the theoretical fundamentals, the experimental part of the work starts on the industrial PECM machine (the machine is explained in chapter 2.2.5) in chapter 2. As the research is more precious by having comparable results with the industrial condition, the first experiments are fulfilled for long-term machining on an industrial PECM. Then the results make the foundation of a laboratorial experiment that is comparable and applicable. There is a lack of knowledge in the tool monitoring in ECM and PECM. Therefore, it is necessary to have a well-founded scientific analysis and investigation. This work is carried out employing numerical, theoretical, and experimental studies.

This study starts by reviewing the publications related to the research topic, followed by an experimental part leading to a comprehensive analytical and metallographic analysis of the materials used. In chapter 2.2, the main experiments with an industrial focus are performed. To conduct the investigation, a developed setup is designed. The machining results are mainly analyzed by microscopic imaging techniques and simulation concepts. The results of these experiments set about the fundamental theories considering the damages on the tool. The theories are hydrogen embrittlement, cavitation erosion, and cathodic corrosion, which are the rest subtopics considered in this study.

Chapter 3 starts by introducing the hydrogen embrittlement principles. Then, a systematic investigation is fulfilled based on the three main perquisites necessary for hydrogen embrittlement: metal condition, atomic hydrogen source, and tensile stress. The results are acquired by microscopy techniques, simulation concepts, X-ray diffraction, and a technique called thermal desorption spectroscopy.

In chapter 4, cavitation erosion theoretically is studied, and some experiments without oscillation of the tool with the industrial PECM machine are done. In this chapter, not only the effect of the tool's oscillation as a parameter of cavitation erosion is investigated, but also the time of the pit's formation on the tool is investigated. This chapter's result helps transfer the experiment from an industrial

machine to a laboratorial setup, as explained in chapter 5.2.3. Laboratorial setup decreases the expenses of the ECM and makes the setup and process control easier.

Chapter 5 suggests a novel field in electrochemistry called cathodic corrosion. So far, it was mostly assumed that cathodes do not undergo any corrosion and oxidation reactions. On the other hand, the new topic of cathodic corrosion considers oxidation and changes on the cathode subjected to a specific condition. This chapter employs different strategies and develops a few setups to find the parameters affecting the changes on the tool. An overview of the work in each chapter is schematically shown in Figure 1-1.
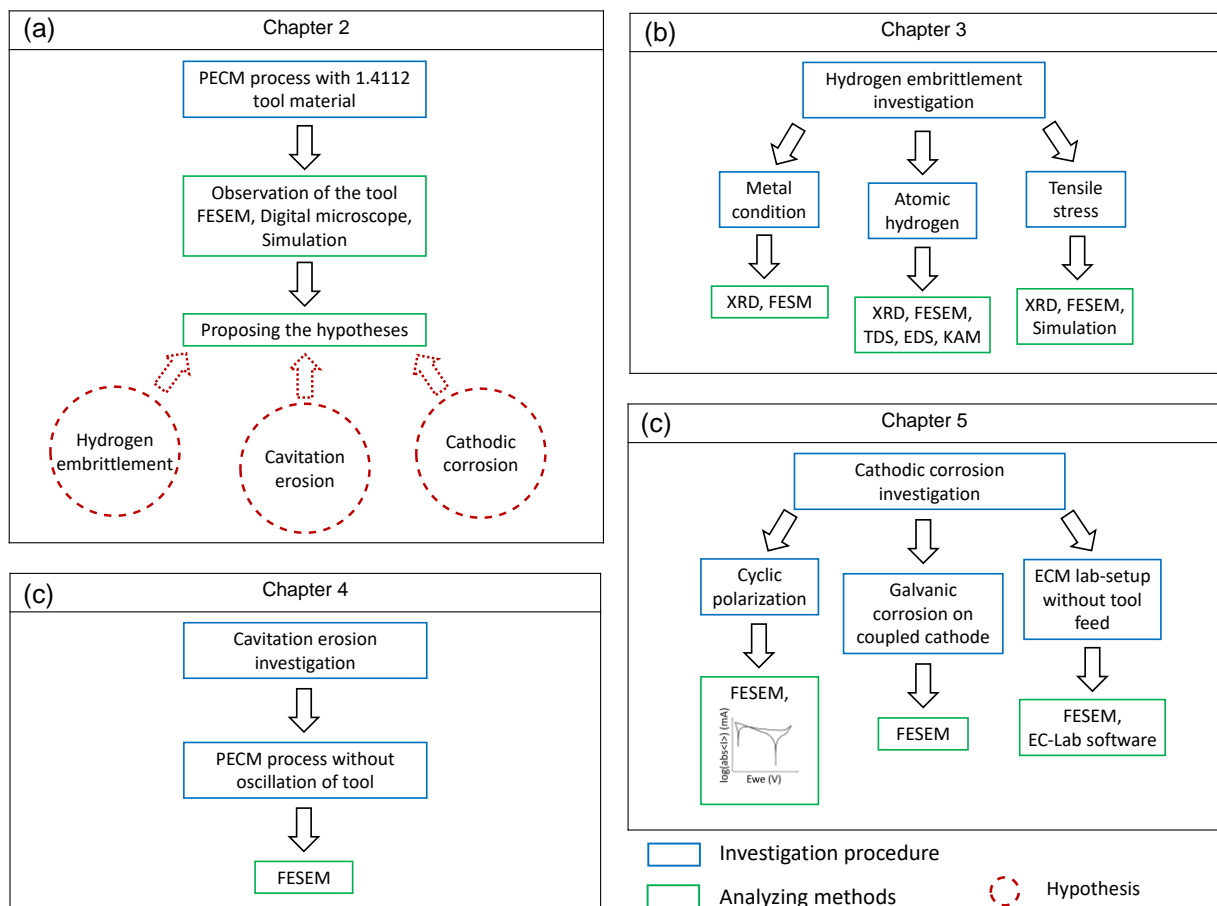
Figure 1-1: An overview of the work in each chapter (a) chapter 2 (b) chapter 3 (c) chapter 4 (c) chapter 5.

2 Principles of electrochemical machining

2.1 Literature review

2.1.1 Electrochemical machining (ECM)

In simple words, ECM is composed of an electrolytic cell that works based on electrolysis and Faraday's law. By connecting the electrodes to the power source, the anode dissolves. Electrolysis uses the passage of current between two electrodes immersed in a conductive solution to perform chemical reactions at the electrodes [6]. Current is passed between a workpiece, which is the positively charged electrode, termed the anode and a tool, which is the negatively charged electrode, termed the cathode. Electrons are carried through the electrolyte in the form of ions. Depending on the potential applied, the material can either be deposited or removed from the electrodes.

Faraday's laws are described [7]:

- First law

  The mass (m) of elements deposited on an electrode is directly proportional to the charge (Q):

$$m \propto Q \qquad \text{2-1}$$

$$\frac{m}{Q} = Z \qquad \text{2-2}$$

  the constant of proportionality, Z, is called the electrochemical equivalent of the substance.

- Second law

  When the same quantity of electricity is passed through different electrolytes, the masses of the ions deposited on the electrodes are proportional to their respective chemical equivalent or equivalent weight (E):

$$E = \frac{\text{Molar mass}}{\text{Valence}} \qquad \text{2-3}$$

A simple schematic representation of basic ECM reactions is shown in Figure 2-1. It shows the dissolution of the anode metal Me, the formation of the hydroxide of the metal $Me(OH)_n$, and hydrogen production on the cathode.
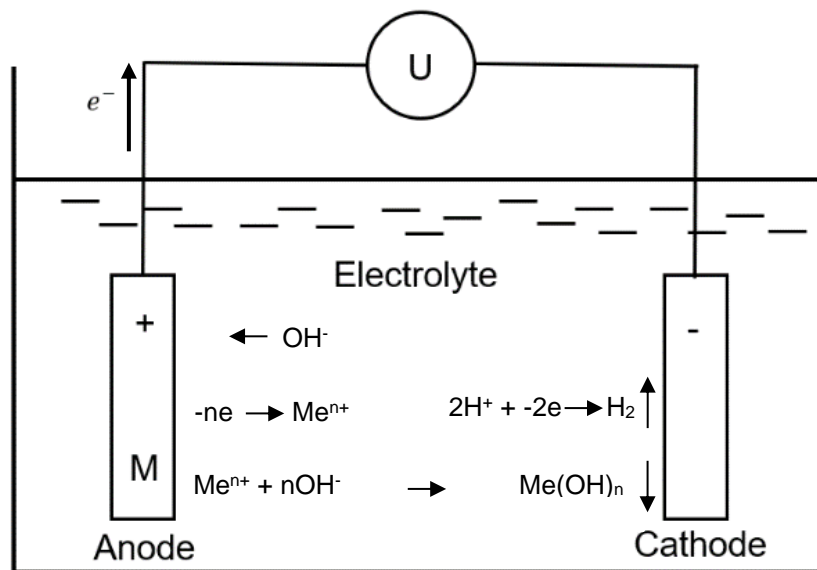
Figure 2-1: Basic reactions of ECM in an electrochemical cell with a power supply. Metal is dissolved from the anode into the electrolyte and the electron is transferred to the cathode. Metal forms hydroxide. At the surface of the cathode, hydrogen is produced.

In DIN8590 [8], ECM is defined as imaging electrochemical removal using an external power source at high active current density caused by a small distance of the shaping tool electrode from the workpiece and the increased flow velocity of the electrolyte solution. The process works based on anodic metal dissolution principles. In an aqueous, electrically conductive medium (NaCl, $NaNO_3$), a DC voltage is applied between the metallic material that would be removed (anode) and a metallic cathode. At the anode, the metal is transferred to the electrolyte solution as ions with the release of electrons.

The most crucial point is having the smallest possible interelectrode gap (IEG) to have efficient machining. During the process, the electrolyte flows in the IEG, removes all the bubbles and products of machining from the IEG, and prevents the boiling of the electrolyte. The IEG size should be kept constant during the process. As a result, the feed movement for the cathode is defined [3].

The current density should be as high as possible to have an excellent working result for ECM. The IEG should be properly defined to have the highest current density and better image accuracy of the tool on the workpiece by having a feed in the tool. The charge exchange occurs between the anode and the cathode in an aqueous electrolyte with a defined IEG and some areas of the anode are targeted. Consequently, the mirror shape of the cathode forms on the anode (Figure 2-2).

The principle of ECM is shown in Figure 2-3. While the tool is constantly fed towards the workpiece $z_k(t)$, the constant current $I(t)$ is applied.

Before ECM   After ECM
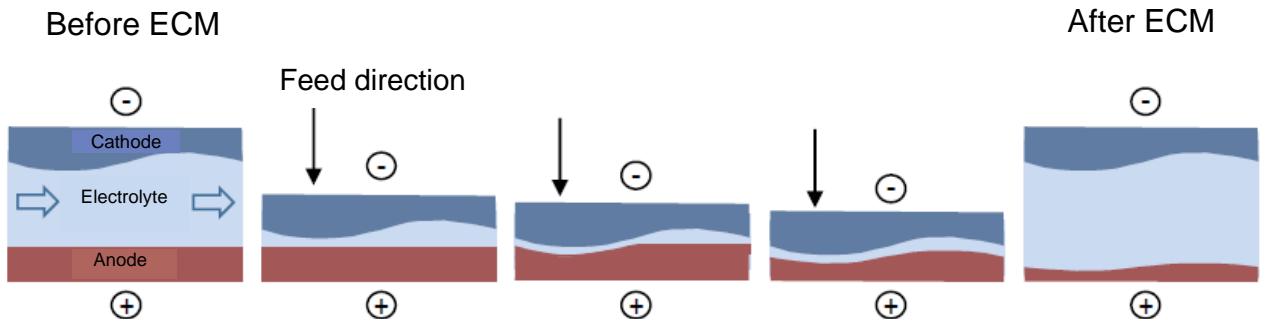
Figure 2-2: Schematic steps in ECM [9]. The cathode gets close to the anode with a constant feed rate while the electrolyte is flowing in IEG and the negative shape of the cathode is produced on the anode.
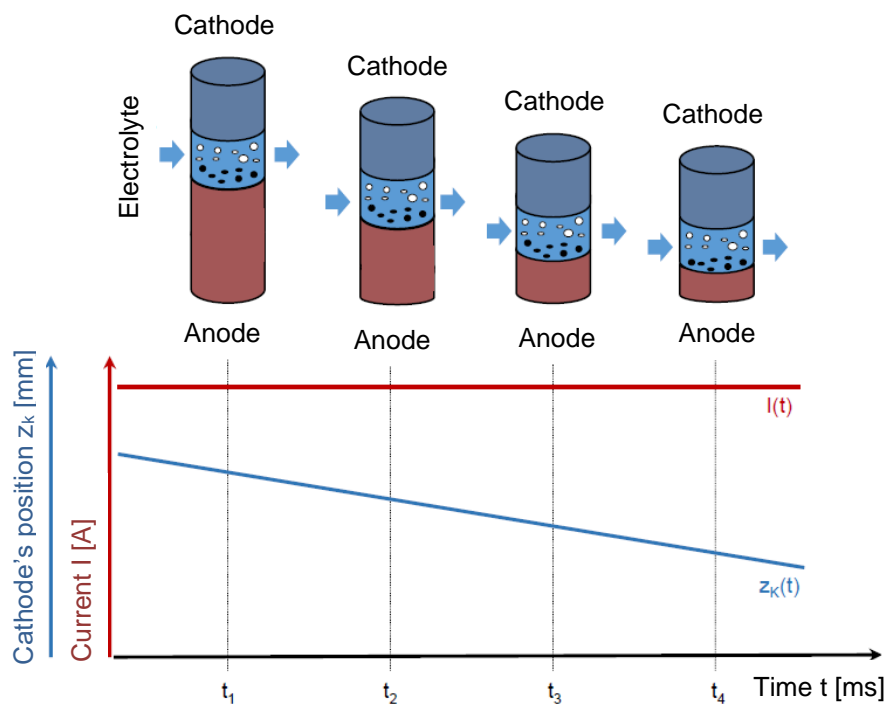
Figure 2-3: The principle of ECM; changes in the current and cathode's position over time [9]. By keeping the IEG constant through a specific feed rate, the current stays constant. The position of the tool is changed to keep the IEG constant by material removal in the anode.

Some advantages lead to choosing ECM as a machining process: the ability to machine complicated shapes, machining different materials with different hardness as it is primarily based on electrochemical reactions [3], high machining efficiency and machining rate, adequate precision, controlled material removal, no heat affected area on the workpiece [10], the excellent surface quality of the workpiece, no tool loss, the high fatigue life of the workpiece [11, 12], no metallurgical alteration of the

workpiece, no burr [13, 14] and no stress [15, 16]. ECM is able to produce a large complex shape in one pass of the tool, which results in an obvious economical advantage by decreasing the machining time [17].

There are some disadvantages as well, which should be always considered next to the advantages: low accuracy in final dimension, stray corrosion [11], high energy consumption, special disposal of electrochemical reaction products and used electrolyte, and complicated process control [13, 18]. Designing a tool electrode is a critical problem for ECM. It should not only have the best dimensional and geometrical design but also should make a suitable flushing path for the electrolyte. A well-designed and developed electrolyte flow across the tool is mandatory to have better machining conditions. Considering the mentioned point, designing the tool is complex and expensive [17]. The tool is not often a perfectly negative mirror image of the workpiece because of electrolyte flow, non-uniform distribution of heat and volume fraction of bubbles, etc. [19-21]. As a result, designing the tool is complex, involving different equations like Laplace, heat conduction, fluid dynamics, and electrochemistry, and needs a good understanding of the process [22, 23].

Five parameters affect ECM results and workpiece shape accuracy, which are shown in Figure 2-4:
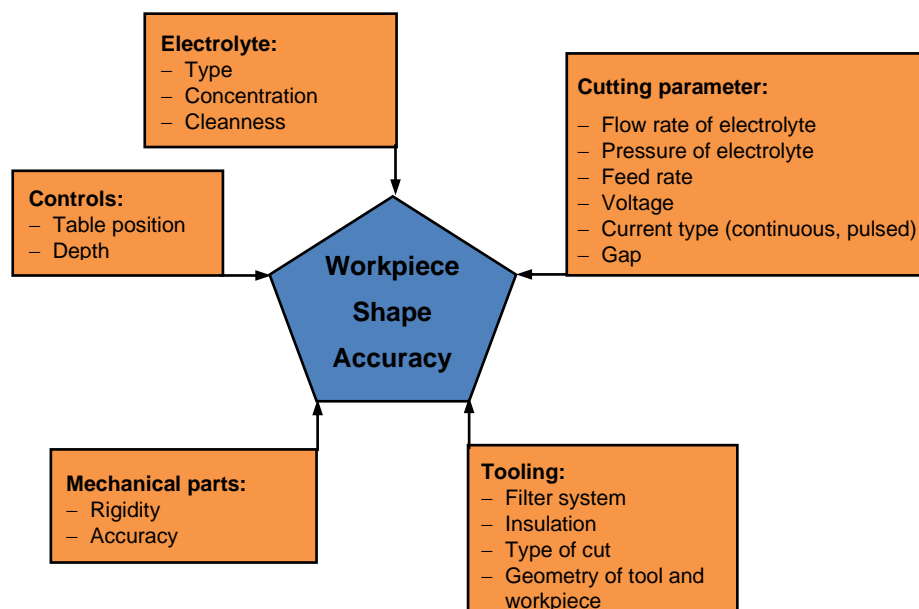
Figure 2-4: Main parameters affecting ECM and workpiece accuracy [24].

A study on ECM shows that between feed rate, electrolyte, flow rate of the electrolyte, and voltage, feed rate affects material removal rate the most [24]. When

choosing a feed rate that is too high, the IEG does not stay constant during machining and decreases. Eventually, a short circuit occurs, creating sparks and damaging the tool and the workpiece [25, 26]. Increasing the feed rate increases the material removal rate, but it could lead to non-uniform dissolution after a specific value due to high-temperature production. As a result, the electrolyte boils or chokes [27, 28]. However, a higher feed rate generally results in less machining overcut due to decreased IEG. In addition, it is reported that roughness at the finished surface of the workpiece decreases [29]. Furthermore, increasing the feed rate leads to an increase in dimensional accuracy [24, 30].

Different components of the ECM process have different roles. The electrolyte is a crucial parameter as it provides the suitable condition needed for reactions, namely a conductive environment [31]. The most important function of the electrolyte is to carry the current between the tool and workpiece, dissipate the heat, remove the machining product from the IEG, and keep the reactions continuous by supplying the necessary elements. Different electrolytes can be used based on the machining parameters like machining rate, material, required dimensional accuracy, and surface integrity. Sodium chloride (NaCl) and sodium nitrate ($NaNO_3$) are used for ferrous alloys like steels, cast irons, and cobalt alloys. Hydrochloric acid (HCl) and a mixture of hydrofluoric acid (HF) with Hydrochloric acid (HCl) are mostly used for nickel alloys, and sodium hydroxide (NaOH) is used for tungsten carbide (WC) [2].

The electrolyte used for ECM should meet other expectations as well [2]:

- The viscosity must be as low as possible.
- The electrolyte must be chemically stable.
- The electrolyte must be chemically active to have a better material removal rate.
- The electrolyte should not form any excess layer on top of the electrolyte, the tool, or the workpiece.
- The electrolyte should not be toxic or corrosive.
- The electrolyte should be economical and readily available.

Table 2-1 shows some electrolytes used for various metals commonly machined with ECM.

Table 2-1: Common electrolytes for a range of metals [32].

Metal	Electrolyte	Remarks
Aluminum and its alloys	$NaNO_3$ (100-400 g dm^{-3})	Excellent surface finishing
Cobalt and its alloys	$NaClO_3$ (100-600 g dm^{-3})	Excellent dimensional control, excellent surface finishing
Molybdenum	NaOH (40-100 g dm^{-3})	NaOH consumed and must be added continuously
Nickel and its alloys	$NaNO_3$ (100-400 g dm^{-3})	good surface finishing
	$NaClO_3$ (100-600 g dm^{-3})	good dimensional control, good surface finishing, and low metal removal rate
Titanium and its alloys	NaCl (180 g dm^{-3}) + NaBr (60 g dm^{-3}) + NaF (2.5 g dm^{-3})	good dimensional control, good surface finishing, and good machining rate
	$NaClO_3$ (100-600 g dm^{-3})	Bright surface finish, good machining rate above 24V
Tungsten	NaOH (40-100 g dm^{-3})	NaOH consumed and must be added continuously
Steel and iron alloys	$NaClO_3$ (100-600 g dm^{-3})	Excellent dimensional control, brilliant surface finish, high metal removal rate, fire hazards when dry
	$NaClO_3$(100-400 g dm^{-3})	Good dimensional control, lower fire hazard, good surface finish, and good machining rate
	$NaNO_3$ (100-400 g dm^{-3})	Good dimensional control, fire hazard when dry, low metal removal rates, rough surface finish

All the electrolytes mentioned above are aqueous. There are some materials used as electrodes that are water sensitive. Then non-aqueous electrolyte like glycerol-based electrolyte is used. The conductivity of this type of electrolyte is lower than aqueous one due to the difficulty of dissolving salt in it. Consequently, the machining rate is lower, but the machining precision is higher. This high-resistance electrolyte is used in electro-polishing, another variant of ECM [33].

Electrolyte concentration is also an important parameter as it determines the electrolyte conductivity. The higher the concentration, the higher the conductivity. Numerous researchers have investigated the effect of concentration. A study showed that with a lower concentration, higher voltage, and a moderate value of pulse-on time, machining accuracy is improved, and the material removal rate is moderate [34]. Another study shows that a higher concentration results in a higher material removal rate and better surface finish. They claim that higher concentrations provide higher ions for ionization, increasing material removal [35, 36]. It is shown that with higher concentration, the dissolution current is higher [3].

Another component necessary for ECM is the DC power supply. The machining rate is proportional to the current density provided by the power supply. High current

density is needed to provide a higher machining rate. At the same time, by having a smaller IEG, a higher current density is achieved. The potential used during ECM is mostly in the range of 5-25 V [2].

With a larger current flowing through the working IEG, the difference in potential between the equilibrium value and the working value is higher. Polarization is defined as the change in the electrode potential from the equilibrium value to the machining value due to the passage of the current in the circuit. The overpotential describes the extent of polarization (η):

$$\eta = E - E_{eq} \qquad\qquad 2\text{-}4$$

The influence of different overpotentials on the total potential drop is shown in Figure 2-5. The current density value is determined by a certain overpotential, as shown in Figure 2-5. This overpotential can be considered as a sum of terms associated with the different reaction steps: the mass transfer, the charge transfer associated with a preceding reaction, etc. [37]. In general, overpotential is the potential used to drive the electrochemical reactions at the cathode and anode surfaces.
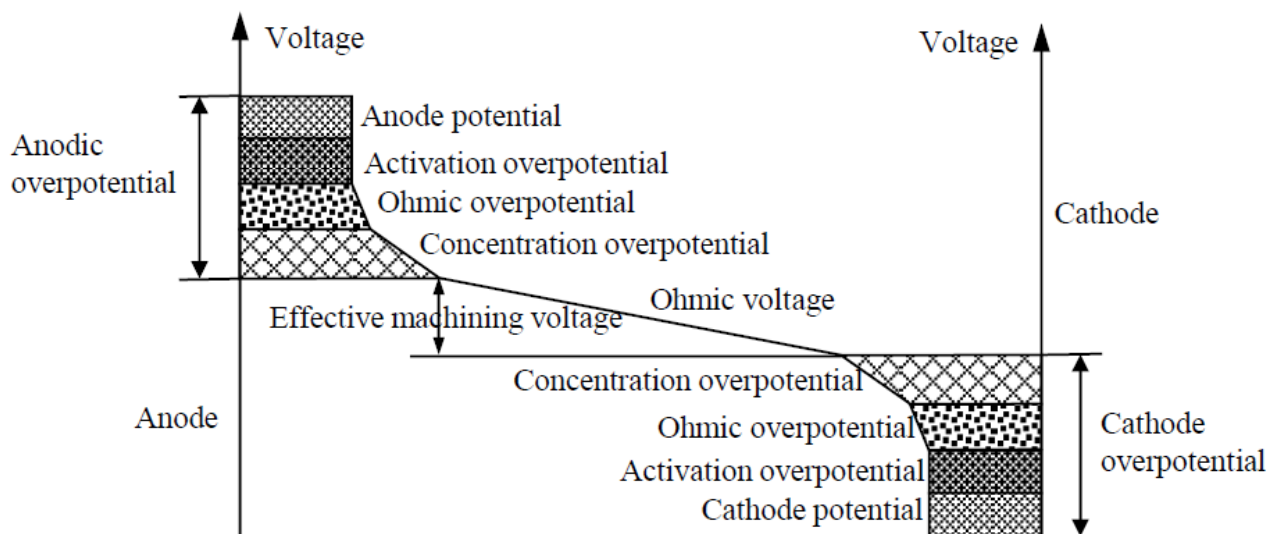
Figure 2-5: Total potential drop during ECM [37].

Electrochemical changes at the electrodes are in equilibrium without applying current by the power source. To have ions discharge and current flowing, additional current must be applied by the power source in the electrochemical cell. With the high activation energy of the charge transfer reaction, an overpotential is needed to drive the reaction in the desired direction to obtain an appreciable rate. It is called activation overpotential (η_{ac}) [37].

There are different types of ions movement in the cell to make electrochemical reactions possible such as migration, convection, and diffusion. The ions move under the influence of potential differences by migration. The physical movement of the electrolyte leads to convection movement. The movement of the ions because of having ions' concentration gradient is called diffusion. Ions usually form a layer of concentrated ions at the surface of the electrode, like a barrier. The charge is transferred only when ions get through this layer. The extra potential needed for the movement of the ions through this layer is called concentration overpotential [37].

In an electrochemical cell, an oxide layer often forms on the surface of the metal, which increases the resistance against the current flowing through the surface. Resistance overpotential is generally regarded as the potential drop across this thin oxide layer on the electrode's surface. The oxide film on the anode, which is the result of passivation, prevents the ions' migration. This can make some difficulties in the ECM process [37].

The applied voltage affects material removal based on $U = IR$, where R is the resistance of the electrolyte. Considering this equation and Faraday's law, it is concluded that applying higher voltage leads to higher current passing and more material removal. In practice, it is proven to be true [36, 38-40].

Depending on the workpiece and electrolyte, the material removal rate becomes constant or decreases by increasing voltage over a specific value. For example, during electrochemical deep hole drilling in nickel-based superalloy with $10\,\text{wt\%}\,NaCl + 2\,\text{wt\%}\,HCl$ electrolyte, the material removal increases sharply between 6-12 V. After 12 V the material removal becomes almost constant. It is explained by increasing the production of hydrogen gas bubbles at a higher voltage which cannot escape the IEG easily. Consequently, the resistance increases, and the current density at the electrode decreases, which leads to a reduction in material removal [41-43].

A circulation system is necessary to have electrolyte flow in the IEG. If the machining products are accumulated in the IEG, the machining rate is reduced and can even lead to a short circuit. The inlet pressure should also be strong enough. Consequently, a strong pump with filtration of the machining products is necessary.

The control system is responsible for setting the electrical parameters, tool feed rate, and electrolyte information like pressure and flow rate. Furthermore, the movement of

the tool at a constant speed is provided by the control system to keep the constant voltage during the process [2].

The mechanical system consists of the working table, working enclosure (to keep the surroundings safe from electrolyte splash), and tool fixture. The tool and workpiece would be placed in this area, or based on the designed process, a particular setup for electrodes and electrolyte flow would be mounted here [2].

2.1.2 Anodic dissolution

ECM process is basically an anodic dissolution process. The workpiece is biased as the anode with respect to the cathode, which is the tool, and both are immersed in the electrolyte. The distance between the tool and the workpiece should be small enough to be able to have a stronger electric field and higher current density, which leads to an increase in the rate of anodic dissolution and material removal. At the anode, metal (Me) is transferred to the electrolyte as the cation, and the released electron moves toward the cathode. In ECM, the goal is to manage the current in such a way that the rate of anodic dissolution stays equal to the feed rate, and the IEG change becomes zero. Current is governed by the migration of ions across the IEG. To have a closed circuit in ECM, the ohmic drop should exist across the electrolyte to let the ions migrate. The ohmic drop results in establishing the electric field, which depends strongly on the distance between electrodes. When the distance between electrodes decreases, the electric field increases. The current density is calculated with the help of potential drop across electrodes, electrolyte conductivity, and the distance between electrodes [17]. The reaction at the anode in a simple form is:

$$Me \rightarrow Me^{n+} + n\ e^{-} \qquad\qquad 2\text{-}5$$

This reaction shows that during anodic dissolution, the workpiece dissolves and produces n electrons transferred to the tool. In reality, the reactions at the anode are more complicated, and some elements are dissolving at the same time. Having stainless steel as the anode leads to the reaction of bi-chromate and makes the electrolyte toxic because of having ions produced by further reactions [44]:

$$2\ Cr + 7\ H_2O \rightarrow Cr_2O_7^{2-} + 14\ H^{+} + 12\ e^{-} \qquad\qquad 2\text{-}6$$
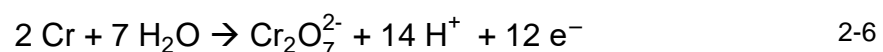
The produced cations stay dissolved or react with the water and make the hydroxide product which precipitates:

$$Me^{n+} + n\ OH^- \rightarrow Me(OH)_n \downarrow \qquad\qquad \text{2-7}$$
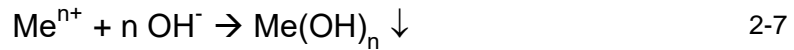
During ECM, voltage is used for both dissolving the anode and producing oxygen (∼15-20%). As a result, pH decreases by the formation of H^+ ions [44]:

$$2\ H_2O \rightarrow 4\ H^+ + O_2\uparrow + 4\ e^- \qquad\qquad \text{2-8}$$
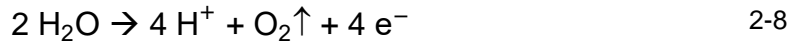
At the cathode's surface, the electrolyte components are reduced. Because of the high-velocity electrolyte flow during the ECM process, the anode cations do not deposit on the cathode. By considering sodium nitrate ($NaNO_3$) as the electrolyte, the reactions are:

$$2\ H_2O + 2\ e^- \rightarrow H_2\uparrow + 2\ OH^- \qquad\qquad \text{2-9}$$

$$NO_3^- + H_2O + 2\ e^- \rightarrow NO_2^- + 2\ OH^- \qquad\qquad \text{2-10}$$
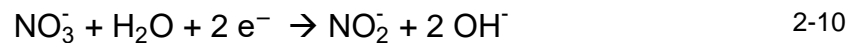
The reactions done on the surface of the cathode and anode in the electrolyte during ECM and PECM processes are shown in Figure 2-6.
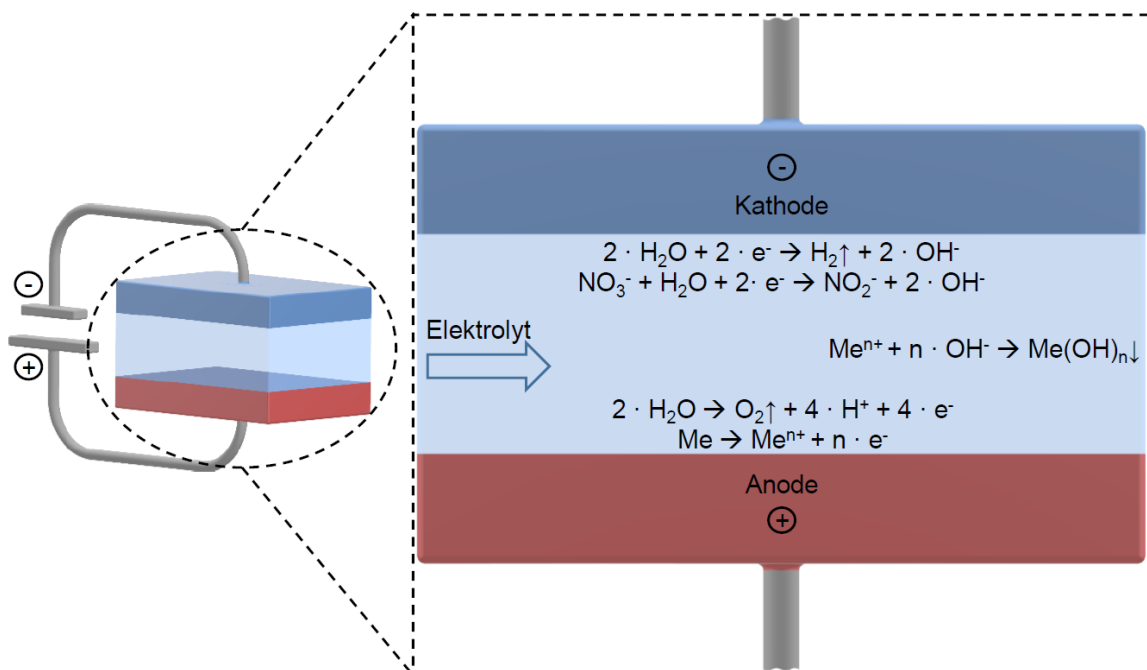
Figure 2-6: Reactions during ECM and PECM in $NaNO_3$ electrolyte [9].

No dissolution and corrosion of cathode metal take place [45, 46]. At the cathode surface, considering Equations 2-9 and 2-10, pH increases. If the current density is high, hydrogen evolution is the principal reaction [44]. Cathodic reaction in the aqueous electrolyte is mostly hydrogen evolution. In some cases, the efficiency of hydrogen evolution is around 100%. By using $NaNO_3$ as the electrolyte, the efficiency

is lower, and less hydrogen is produced as nitrate reduction is the main reaction at the cathode [3]. The side reactions in the $NaNO_3$ electrolyte are responsible for the reduction in efficiency compared to NaCl (Figure 2-7).
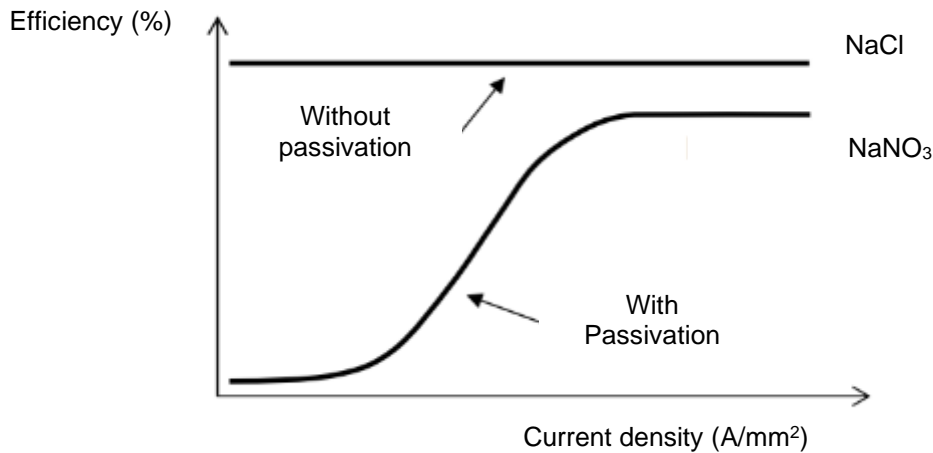
Figure 2-7: Efficiency of NaCl and $NaNO_3$ electrolytes based on the passivation [47]. No passivation occurs in the NaCl electrolyte leading to higher efficiency.

Another important parameter during sinking ECM is side IEG which should be distinguished from frontal IEG. Frontal IEG is the area between the cathode and the anode in the projection direction of the tool feed. The side IEG forms as a result of stray current. The amount of material dissolved and geometric shape with the same proceeding time, initial side IEG S_x, and conductivity for different electrolytes are different (Figure 2-8). It is because of the different efficiency of each type of electrolyte.
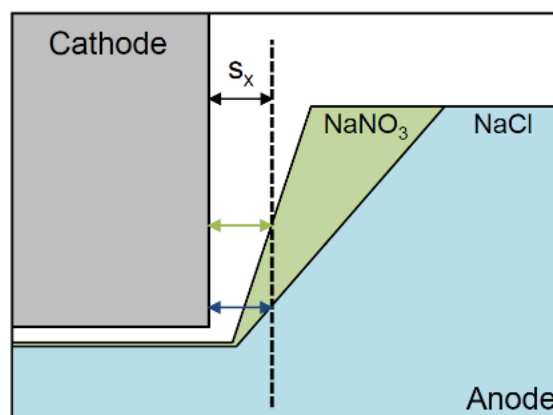
Figure 2-8: Geometric shape and gap evolution using a NaCl and $NaNO_3$-based electrolyte [48]. Passivation in the $NaNO_3$ electrolyte leads to higher precision in the side IEG.

The current production in the ECM system through other processes than the anodic dissolution of the workpiece is considered as inefficiency. These processes are the hydrogen gas bubbles production and different reactions between ECM products. Usually, the current efficiency of 75-90% is acceptable for ECM [17].

In different studies, the dependency of current efficiency is investigated. In Clarke and McGeough's work, increasing the electrolyte's velocity leads to an increase in current efficiency. The anode material is mild steel immersed in nitrate electrolyte. In addition, this experiment shows that by using sodium chloride as the electrolyte, the current efficiency of the same anode is constant (close to 100 %) in different machining conditions [49].

The dependency of current efficiency on the electrolyte velocity for iron dissolution in 5 M NaCl is investigated in a study by Datta and Landolt. The current efficiency is 70% in low velocity up to 1 m/s for iron as the anode in nitrate electrolyte. By increasing the velocity to 10 m/s, the efficiency increases up to 100% because of the increase in current density [50].

Reactions at the cathode and anode depend on electrode and electrolyte properties like pH. Acidic and neutral electrolytes are mostly chosen [3]. Having iron as the anode, soluble ions form up to a pH of 9, and then oxide or hydroxide forms on the surface, which causes passivation [51]. As a result, it is valuable to use Pourbaix diagrams to get more information about electrochemical processes. When the passivity increases, a higher overpotential is needed to overcome it. This is common in metals with lower conductivity, like Al, Ta, and Ti [3].

The existence of aggressive anions like halides leads to the formation of pits. Besides halides, sulfate, perchlorate, and nitrate ions can also lead to pitting in some conditions. Dimensional accuracy is also affected by the passivity of the anode. If NaCl is used as an electrolyte, the passive layer does not form, and the machining accuracy would be less because of the stray current. As a result, sodium nitrate electrolyte leads to better roughness and overcut in the workpiece [3].

Setting the appropriate flow rate and viscosity for the electrolyte prevents the electroplating on the cathode. Lower concentration polarization and sweeping away the machining products are possible with a high fully developed flow rate in the turbulent range (Reynolds number greater than 2000). In this case, cavitation would happen if there is a sudden change in the flow direction and the surface finish is poor [3].

To have a comprehensive understanding of ECM, some specific terms and relations should be introduced. Based on Faraday's law, the removal rate of electrochemical dissolution (v) has a relation to the material molar mass M, valence Z, and density ρ in the normal direction of the machining feed rate and a constant applied current density J (in the normal direction to the anodic surface) [48, 52]:

$$v = \frac{M}{z \cdot F \cdot \rho} \cdot J \qquad \text{2-11}$$

This relationship can be derived from Faraday's law as follows:

$$m = V \cdot \rho = \frac{M}{z \cdot F} \cdot I \cdot t \qquad \text{2-12}$$

$$V = \frac{M}{z \cdot F} \cdot \frac{1}{\rho} \cdot I \cdot t \qquad \text{2-13}$$

$$V = A \cdot h = \frac{M}{z \cdot F} \cdot \frac{1}{\rho} \cdot I \cdot t \qquad \text{2-14}$$

A is the removal surface area, V is the removal volume, and h is the removal height in the case of an ideal cylindrical anode, then further points are taken into consideration:

$$\frac{h}{t} = \frac{M}{z \cdot F} \cdot \frac{1}{\rho} \cdot \frac{I}{A} \qquad \text{2-15}$$

With

$$v = \frac{h}{t} \text{ (assuming t = const.)} \qquad \text{2-16}$$

$$J = \frac{I}{A} \qquad \text{2-17}$$

Then

$$v = \frac{M}{z \cdot F} \cdot \frac{1}{\rho} \cdot J \qquad \text{2-18}$$

The current density J is usually used, either in A/cm² or A/mm², and the current itself is one of the most important and modifiable parameters in Faraday's law when carrying out an experiment.

The material-specific components, sometimes referred to as the electrochemical equivalent for a material, can be derived from Equation 2-14.

$$SMR = \frac{M}{z \cdot F} \qquad \text{2-19}$$

$$MRR = \frac{M}{z \cdot F} \cdot \frac{1}{\rho} \qquad \text{2-20}$$

The specific mass removal (SMR) is in [mg/C], as well as the mass removal rate (MRR) is in [cm³/C]. The MRR in ECM basically depends on the following three factors: 1. Anodic reactions and current efficiency 2. Mass transport effect 3. Current distribution and shape evolution [53]. The relationship between the two introduced removal rates can be written as follows:

$$MRR = SMR \cdot \frac{1}{\rho}$$ 2-21

Therefore Equation 2-18 becomes:

$$v = MRR \cdot J = SMR \cdot \frac{1}{\rho} \cdot J$$ 2-22

It is obvious that an essential factor to be used in production is still missing. While the velocity or removal rate is often synonymous with the feed rate applied in ECM, the factor allowing contemplations towards shaping accuracy comes from Ohm's law:

$$U = R \cdot I$$ 2-23

U is potential in [V], and R is ohmic resistance in [Ω]. Based on Ohm's law, there is a relation between the current and applied voltage in an electrically conductive medium. The conductive medium in ECM is the electrolyte. Ohm's law should be changed in the way that presents ECM setup information. Assuming two parallel and equally sized opposing electrode surfaces at a distance s in [µm], a specific resistance of the electrolyte κ in [Ωcm], the resistance in the enclosed volume, and A cross-sectional area in [cm²] is written as:

$$R = \kappa \cdot \frac{s}{A}$$ 2-24

which

$$\kappa = \frac{1}{\sigma}$$ 2-25

σ is conductivity in [mS/cm]. The overall resistance is:

$$R = \frac{s}{\sigma \cdot A}$$ 2-26

Ohm's law is written as:

$$U = R \cdot I = \frac{s}{\sigma \cdot A} \cdot I = \frac{s}{\sigma} \cdot \frac{I}{A}$$ 2-27

By considering J as the current density in [A/cm²]:

$$U = \frac{s}{\sigma} \cdot J \leftrightarrow s = \frac{U \cdot \sigma}{J} \leftrightarrow J = \frac{U \cdot \sigma}{s}$$ 2-28

Conductivity is calculated considering each type of ion, i:

$$\sigma = \sum_i c_i u_i b_i F \qquad\qquad \text{2-29}$$

where c is the concentration of each ion, u is the ion's mobility, b is the charge number, and F is Faraday's constant. The mobility of the ion is calculated by:

$$u_i = \frac{z_i \cdot e}{6\pi \cdot \mu \cdot r_i} \qquad\qquad \text{2-30}$$

where $z_i \cdot e$ is the charge of the ion, r_i is the radius of the ion, and μ is the solution viscosity. It is clear from Equation 2-30 that smaller, highly charged ions have greater mobility.

The production of soluble and insoluble machining products changes the conductivity by consumption of electrolyte ions. Temperature changes affect the conductivity as well. By increasing the temperature, the mobility of the ions in the electrolyte increases, leading to an increase in conductivity. Mostly the conductivity changes linearly with temperature changes according to:

$$\sigma = \sigma_0 \left[1 + \beta \left(T - T_0\right)\right] \qquad\qquad \text{2-31}$$

where β is the temperature coefficient of the conductivity and σ_0 is the initial conductivity at the temperature T_0. The Joule heat produced in the IEG increases the temperature linearly. A high electrolyte flow rate disperses the heat generated more than a low flow rate.

The machining products affect the conductivity as well. The dissolved hydrogen in the electrolyte does not affect equation 2-31, but the bubbles make voids in the electrolyte leading to a decrease in the conductivity value. The changes in temperature in IEG are shown in Figure 2-9 [54].
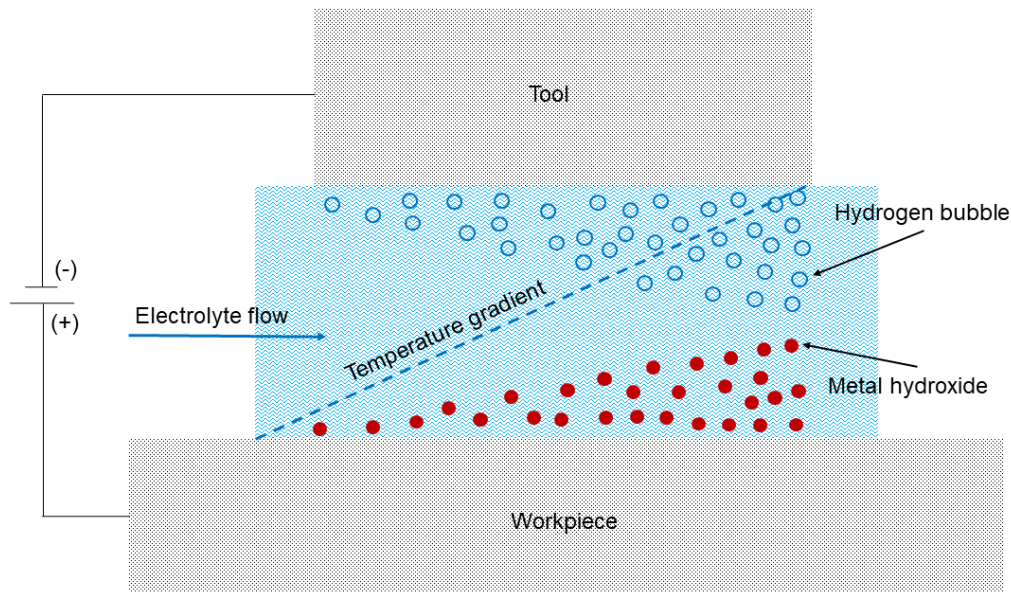
Figure 2-9: Schematic diagram showing the effect of temperature and machining products in IEG (Adapted from [54]).

2.1.3 Electrode polarization

In the equilibrium condition without applied current by the power source, there is an electrode potential barrier between the electrode and electrolyte, which prevent a higher rate of reactions. External energy overcomes this barrier, and ions are discharged. "Polarization" describes the changes in electrode potential from equilibrium with the external current. Current vs. potential curves, particularly those obtained under steady-state conditions, are called "polarization curves." Anode potential and current density are two important factors during ECM that affect the workpiece's dissolution. As a result, they also have effects on the surface finish. In Figure 2-10, two different polarization curves for the anode are shown. Curve 1 represents the occurrence of etching where metal dissolves more preferentially from the areas with lower electrode-chemical potentials. As a result, the discontinuous dissolution rate across the grain boundaries generates an uneven surface. Curve 2 represents the passivation phenomenon in which the passive oxide film is generated in the region (i). The current density becomes lower, resulting in a lower electrochemical dissolution rate. However, when the potential increases further, a transpassive phenomenon occurs due to the breakdown of the passive film. Hence, material dissolution becomes uniform resulting in a good surface finish [37].
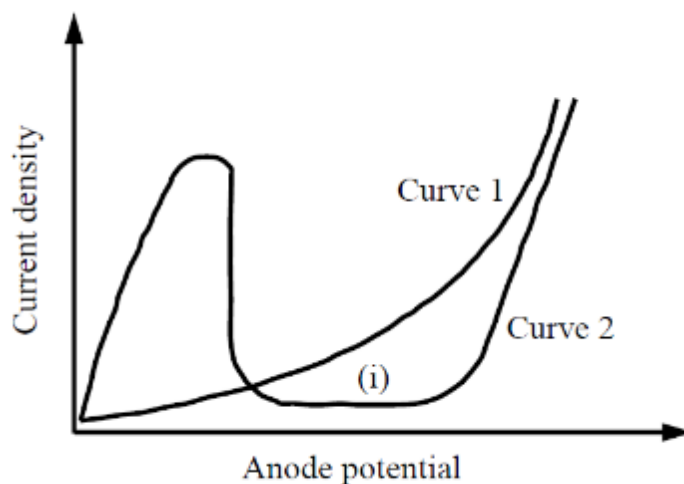
Figure 2-10: Potential-current density polarization curve for anode [37].

2.1.4 Pulse Electrochemical machining (PECM)

The industrial ECM process has shown some limitations and disadvantages. The most important problems are control over the IEG distribution, dimensional accuracy, and tool design for complicated shapes. Both theoretical and industrial experiments showed that using pulsed current with oscillation of the tool solves the problems by keeping the IEG smaller than in ECM. Therefore, a pulse generator is needed to supply voltage pulses, called PECM [55]. Doing PECM, better electrolyte flow conditions, higher localization of the anodic dissolution, and small and stable IEG are achieved, which leads to higher accuracy in shape and better process control [56-58]. Pulses are usually applied as a square wave with variations in amplitude (voltage frequency and duration). Pulse-off time is not usually equal to pulse-on time as longer off time is needed to clean the IEG from machining products. It allows the double-layer capacitor to be fully discharged as well.

The principles of the PECM are illustrated in Figure 2-11. In the beginning, the IEG is at the central position and electrolyte flows in this zone. The voltage and electrical current are zero. In the next step, the cathode moves towards the anode, and the rectangular electrical current pulse is applied when the cathode reaches the position with the defined IEG. In this step, material removal occurs, and Joule heat increases the temperature of the electrolyte. Higher temperatures, hydrogen generation, and machining products affect the electrical conductivity of the electrolyte [59]. In ECM without oscillation, the small IEG and high concentration of machining products could

lead to deposition on the tool [53]. In the next step, the electrical current is zero, and the cathode moves upwards. Consequently, the IEG is greater, and the electrolyte flushes away all the products of the machining and heat. Afterward, the tool moves down again to have a small defined IEG. Then, the current is applied and material removal occurs. All these steps repeat during the whole PECM machining [59].
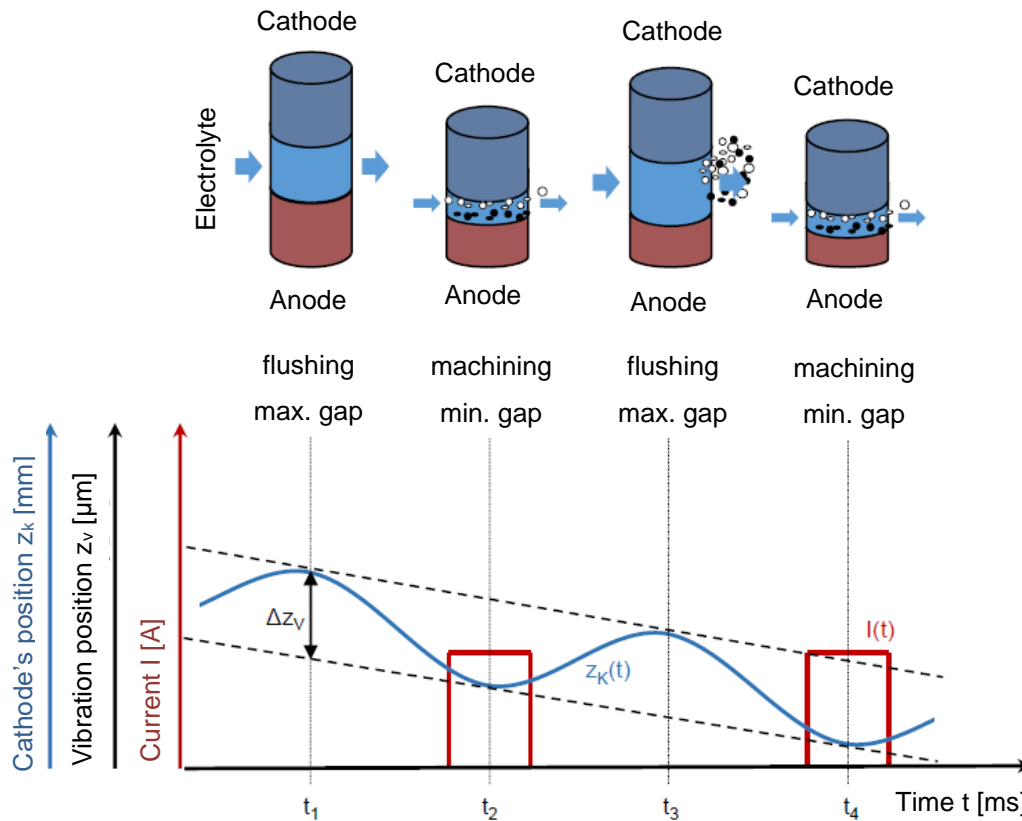
Figure 2-11: Principle of PECM with oscillation of the tool [9]. When the tool is in the position with a defined IEG the current is applied.

Choosing the optimum duty cycle and pulsed frequency is necessary for localized machining. Increased pulse frequency generates a shorter pulse period, and as a result, controlled material removal is achieved [60]. In general, PECM produces a better surface finish and roughness on the workpiece [61].

The material removal rate is reduced as effective machining time is reduced. This makes PECM a good option as a finishing process after DC-ECM or conventional technologies [61].

One tool oscillation in PECM takes T which is achieved by the sum of t_{on} [ms] and t_{off} [ms]. A duty cycle is defined as the coefficient of t_{on} divided by T. t_{on} is the time that electrical current is applied, and at t_{off}, it is stopped.

All formulas introduced for ECM should be adapted to PECM. It is possible by considering a constant factor composed of the pulse on time and the pulses per time unit, which is, in this case, defined by the frequency f of the sinusoidal oscillation. Therefore, Faraday's law is [48]:

$$Q = I \cdot t \cdot t_{on} \cdot f = \frac{m \cdot F \cdot z}{M} \qquad \text{2-32}$$

t is uninterrupted machining time and t_{on} is the length of each current pulse. The feed rate is defined as:

$$v = \frac{M}{z \cdot F \cdot \rho} \cdot J \cdot t_{on} \cdot f \qquad \text{2-33}$$

2.1.5 Application of ECM and PECM

The desired manufacturing method is chosen based on cost efficiency and achieved features. The ECM and PECM are primarily used in machining hard materials as the machining parameters are independent of the material and machining of complex shapes like jet blades [2]. The general categorizing of their application to be used efficiently is well defined in the dissertation of Clifton [62].

- Irregularly shaped cavities with features running along a single axis. ECM and PECM have advantages over other machining methods in machining deep cavities. Conventional machining methods are not functional in machining cavities with the depth to diameter ratio greater than ten to one. They are mostly cavities in forging dies, drilling deeper holes, and irregularly shaped holes.

- Holes and other features required in fragile and/or thin, delicate components. Conventional machining methods normally impose great cutting forces on the workpiece. The force leads to breakage or distortion of the workpiece in fragile and thin components. This is not a problem in ECM and PECM, as there is no contact between the tool and the workpiece.

- The machined surface that requires to be stress-free or highly polished. The contactless feature of ECM and PECM make them exemplary methods for producing stress-free surfaces. In addition, the roughness at the finished surface is low (depending on the machining condition, material, and electrolyte R_a is less than 1 µm).

Regarding the advantages of ECM and PECM, it has applications in different fields, such as aerospace, automotive, offshore, and medical engineering industries. An example of ECM application in the aerospace industry is the production of cooling holes in turbine blades. The dimeters of such holes are 1-4 mm, and the aspect ratio is 40-200. The material used to produce turbine blades is super heat resistant material such as nickel-based super alloy and titanium alloy [63]. The cathode is generally a side insulated tube in which electrolyte flows downwards inside of that. During ECM, overcut is a problem that makes a greater diameter in the generated hole. The problem is minimized by the insulation of the cathode [17]. The cooling holes in a blade are illustrated in Figure 2-12.
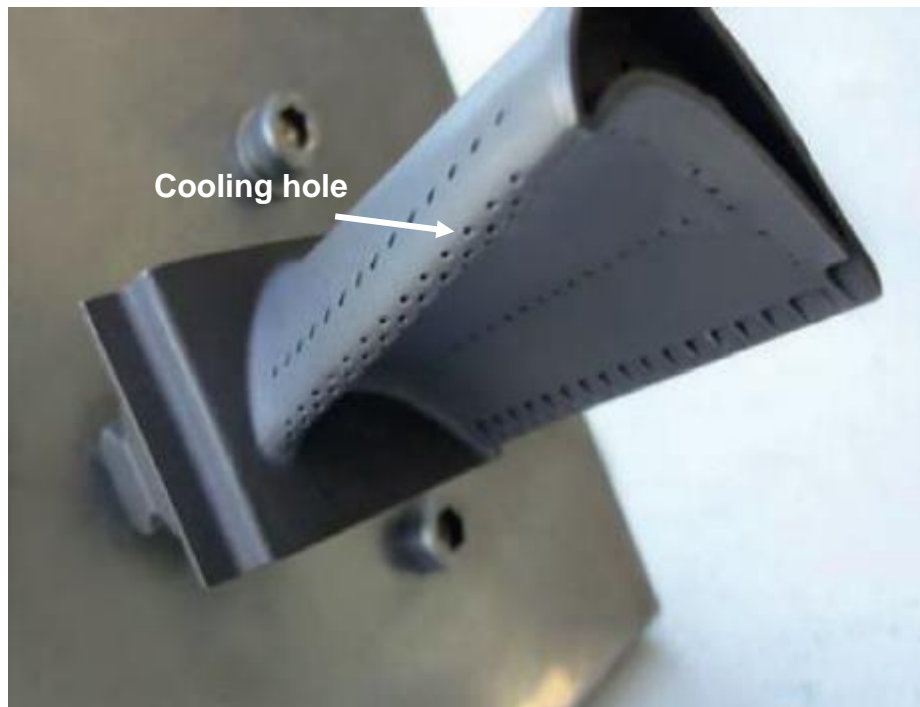
Figure 2-12: Cooling holes on gas turbine blade [63]. They are produced by ECM and PECM.

Defect sampling is another application of ECM, which is mostly carried out on the welded structure containing a defect. It helps not only to exclude the defect and prevent further damages but also a sample is acquired which, by analyzing it, the lifetime of the sample is estimated. This application is used in offshore structures [17].

Titanium and its alloys have medical applications such as orthopedic and dental implants. However, these materials are difficult to machine, which increases the tool wear of conventional machining processes. In addition, employing the conventional

machining processes leads to a poor surface quality of the machined area and low productivity related to high production costs [64]. The complex shape of implants, next to the high hardness of titanium and its alloy, make them an interesting target to be machined by ECM and PECM. The bone fixtures made of nitinol are successfully machined by PECM (Figure 2-13).
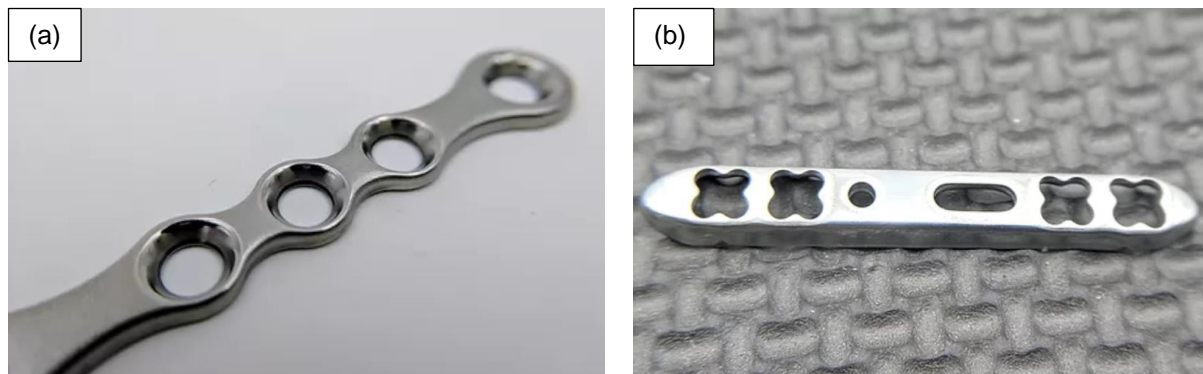
Figure 2-13: (a) and (b) Bone fixtures made of nitinol by PECM [65].

2.2   Experimental

2.2.1   Motivation

In research studies, one advantage of ECM and PECM compared to other machining processes is no tool loss [11, 12]. However, Weber states that pits form on the surface of the tool [66]. The tool material is cast iron which is composed of a ferrite matrix with spherical graphite dissipated. The tool is immersed in $NaNO_3$ with the machining condition of pH = 7, U = 9 V, and each machining cycle lasts for 5 min. The existence of small IEG and coarse graphite protrusions out of the surface is claimed to cause undetectable short circuits between the tool and workpiece, leading to damage on the tool [66]. The damaged surface is shown in Figure 2-14 (a). Point B in Figure 2-14 (b) shows the pit formed on the tool with higher magnification.
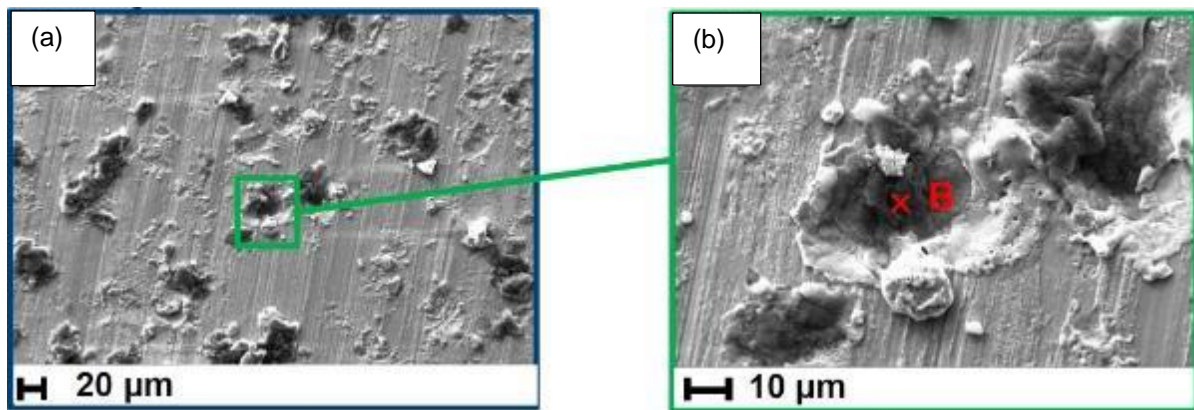
Figure 2-14: Formation of the pit on the cast iron as the tool after PECM with different magnifications in NaNO$_3$ electrolyte with the machining condition of pH = 7, U = 9 V [66].

In another study, Kamaraj and Sundaram claim that microtool geometry changes happen because of cavitation corrosion [67]. Tungsten carbide is used as the tool for PECM in 1 M NaOH electrolyte with 5 V in mentioned study. Cryogenic treatment is used in this study to improve the damage on the tool due to cavitation corrosion.

Corrosion of the tungsten carbide as the tool is reported in another study in the voltage range of -0.6 V to -0.1 V on the micro tools during PECM as well [68].

This work aims to present a systematic approach to investigate the tool during ECM and PECM to improve its lifetime by lowering its wear and damage. The employed methods and strategies are summarized at the end of chapter 1. The introduced material as the tool is martensitic stainless steel which is chosen to have a ferrite matrix and carbides that do not protrude out of ferrite. The material is introduced in chapter 2.2.3 In addition, the IEG is considered big enough to ensure no undetectable short circuit occurs.

Three hypotheses are proposed in this study for the probable mechanisms of the changes on the tool. However, in many cases discussing the electrochemical systems is crucial because of complicated reaction mechanisms, including multiple electrochemical or chemical reactions [69]. Hydrogen embrittlement is chosen as the first hypothesis because of the high applied voltage in ECM that produces a large amount of hydrogen on the tool [70]. Cavitation erosion is the second hypothesis because the oscillation of the tool changes the pattern of flow in the electrolyte which may change the local pressure in the electrolyte [3]. Cathodic corrosion is the last hypothesis which usually happens by having high pH and alkali metal in the electrolyte [71]. These hypotheses as the possible reasons for the changes are

investigated. The mechanisms of these hypotheses are briefly illustrated in Figure 2-15 but they are explained in details in further chapters.

(a)

Adsorbed H atom

Accumulated H atom

Localized corrosion area

Trapped H atom at dislocations

Trapped H atom at particles

(b)

Bubbles

Cavitation erosion due to direct bubble collapse

Cavitation erosion due to abrasive sliding marks

(c)

Oxidation of alkali metal

Cathode   Alkali cations   Cathode   Cathode
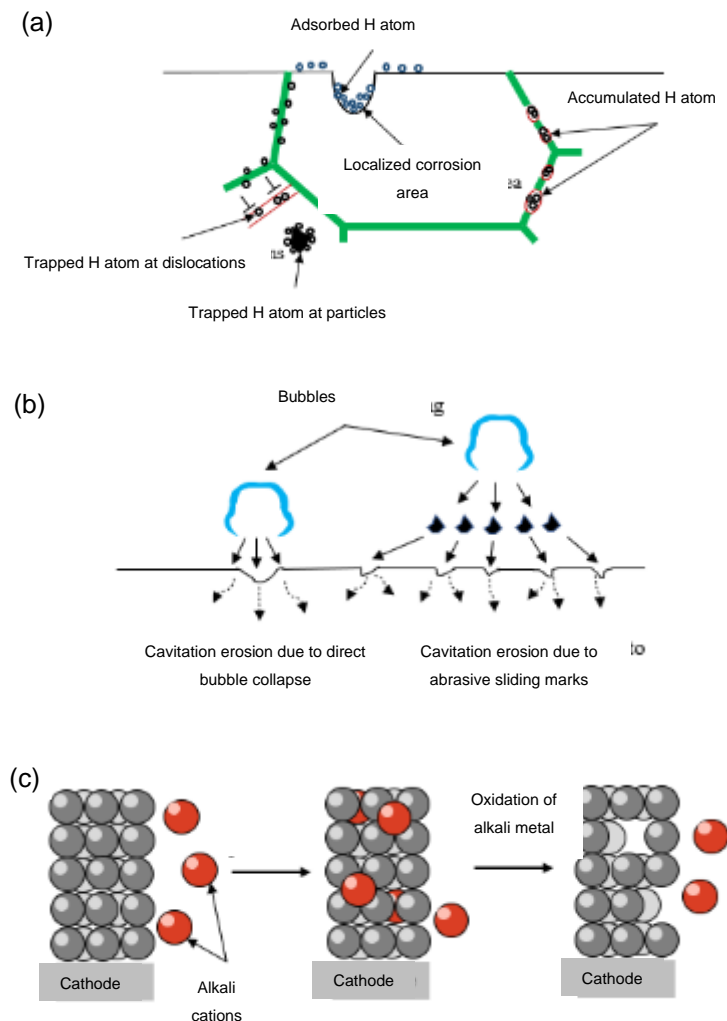
Figure 2-15: (a) Hydrogen Embrittlement mechanism (b) cavitation erosion mechanisms caused with the help of particles in the electrolyte or without particles (c) cathodic corrosion, alloying with cathode elements mechanism (Adapted from [71-73]).

The effects of all these hypotheses are studied with the help of a PECM machine, ECM laboratorial setup, and different developed laboratorial setups. The results of the PECM machine and laboratorial ECM setup correlated with each other with the help of some experiments, which are explained in related chapters. In general, this study starts with the PECM experiment and observation of the changes on the tool. Hydrogen embrittlement and cavitation erosion are investigated regarding PECM. Cathodic corrosion is investigated with laboratorial setup of ECM.

2.2.2 Material

Considering the chemical composition and the microstructure is necessary to discuss the phenomena occurring during ECM. As a result, the samples are subjected to analytical and metallographic investigations. The material used in this investigation are:

1. Stainless steel (1.4112) is used as the tool during ECM and PECM.
2. Bearing steel (1.3505) is used as the workpiece during ECM and PECM.

2.2.3 Stainless steel 1.4112

The material is martensitic stainless steel purchased from Eisen Schmitt in St. Ingbert, Germany, and is used as the tool. The metal is a 3 m shaft with a diameter of 20 mm in annealed as received condition and is used without further heat treatment. This material is mainly used where high wear and moderate corrosion resistance are required [74]. A wide range of applications of this material in the industry is found, such as molds, tools, structural parts of automotive and biomedical devices, etc. [75]. The martensitic stainless steel EN 1.4112 is also known as DIN X90CrMoV18 or AISI 440B. The motivation for choosing this material and research goal are explained briefly in chapter 2.2.1. The chemical composition of the material derived from the database is shown in Table 2-2, besides the composition achieved by field emission scanning electron microscope (FESEM) (ZEISS SIGMA) and energy dispersive spectroscopy (EDS) (Oxford Instruments Xmax), at the Institute of Material Science and Methods, Saarland University. The mass percentage from the database and experimental data are in good agreement. The acceleration voltage is 20 kV, leading to no detection of lighter elements with lower concentrations during EDS.

Table 2-2: Chemical composition of stainless steel 1.4112 [76].

Steel Symbol X90CrMoV18 Steel Number 1.4112	Element									
	Fe	Cr	Mo	C	Mn	Si	V	P	S	Other
Composition (Weight %) Min Max	76.6 81.2	17.0 19.0	0.9 1.3	0.85 1.0	0.0 1.0	0.0 1.0	0.07 0.12	0.0 0.04	0.0 0.015	
EDS-Composition (Weight %)	78.8	18.5	1.0		0.8	0.5				0.4

Figure 2-16 illustrates the microstructure of the material. The microstructure is composed of a ferritic matrix with carbide of Cr dispersed. As the sample is in the annealed condition, no martensite is observed in the microstructure. The X-ray diffraction (XRD) is done by PANalytical Empyrean at the Institute of Functional Material, Saarland University. To do this analysis, a Co tube, Slit optics, Iron filter, and a multi-channel semiconductor detector (PIXcel) are used.

The result shown in Figure 2-17 is in good agreement with the FESEM image. The detected phases are $Cr_{23}C_6$ (ICDD code: 04-002-2448) and ferrite with dissolved Mn (ICDD code: 04-004-9071).
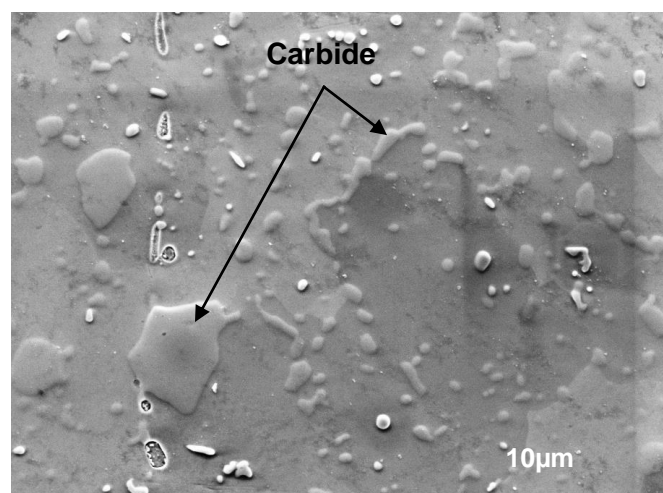
Figure 2-16: Microstructure of martensitic stainless steel 1.4112 used as the tool in annealed as received condition including ferrite and carbides.
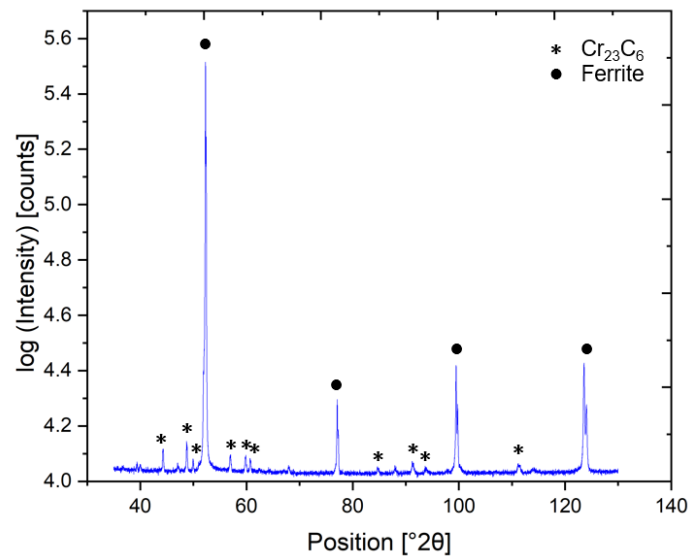
Figure 2-17: Phase analysis of martensitic stainless steel 1.4112 used as the tool.

2.2.4 Bearing steel 1.3505

The material is bearing steel purchased from Eisen Schmitt in St. Ingbert, Germany, and is used as the workpiece. This steel is a hard-to-machine material with conventional machining methods. Then, it is a good target as a workpiece in ECM and is widely used in industry [60]. This material is used in the manufacturing of bearings, ball screws, gauges, axles, and joints [77].

The steel EN 1.3505 is also known as DIN 100Cr6 or AISI 5210. The chemical composition of the material derived from the database and achieved by EDS are in good agreement and shown in Table 2-3. The acceleration voltage is 20 kV leading to no detection of lighter elements with lower concentrations during EDS. The microstructure of the 1.3505 is illustrated in Figure 2-18. The steel is etched in Nital 3% for 40 s to reveal the details of the microstructure. It is composed of ferrite with carbides of Cr [78].

Table 2-3: Chemical composition of bearing steel 1.3505 [76].

Steel Symbol 100Cr6 Steel Number 1.3505	Element											
	Fe	Cr	C	Mn	Si	Cu	Mo	Al	S	P	O	Other
Composition (Weight %)												
Min	97.1	1.4	0.93	0.25	0.15	0.0	0.0	0.0	0.0	0.0	0.0	
Max	98.3	1.6	1.1	0.45	0.35	0.3	0.1	0.05	0.03	0.025	0.0015	
EDS-Composition (Weight %)	96.2	1.6		0.5	0.3	0.2					0.1	1.1
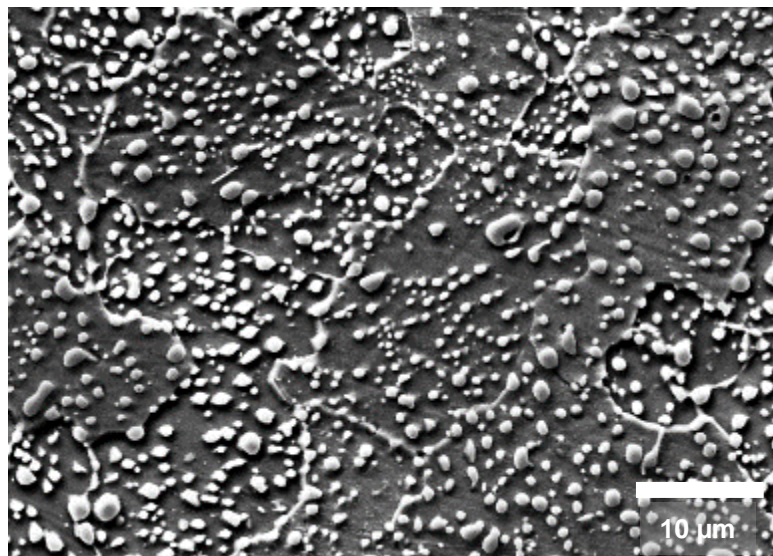
Figure 2-18: Microstructure of bearing steel 1.3505 etched by Nital 3% for 40 s used as the workpiece. There is a matrix of ferrite with carbides.

2.2.5 Industrial electrochemical machine

The experiment is carried out on the PECM machine, PEMCenter 8000 PECM system, from PEMTec SNC. (Forbach, France) at Center for Mechatronics and Automation Technology (ZeMA gGmbH) (Saarbruecken, Germany). The machine is shown in Figure 2-19.

It is divided into four groups: electrolyte supply, machining chamber, control system, and process energy source. To have an efficient working environment, the main

electrolyte supply (electrolyte volume of 2000 l) is replaced by a specially developed unit with an electrolyte supply capacity of 200 l. As a result, the applicable electrolyte pressure in this chamber is limited to a maximum of 5 bar.
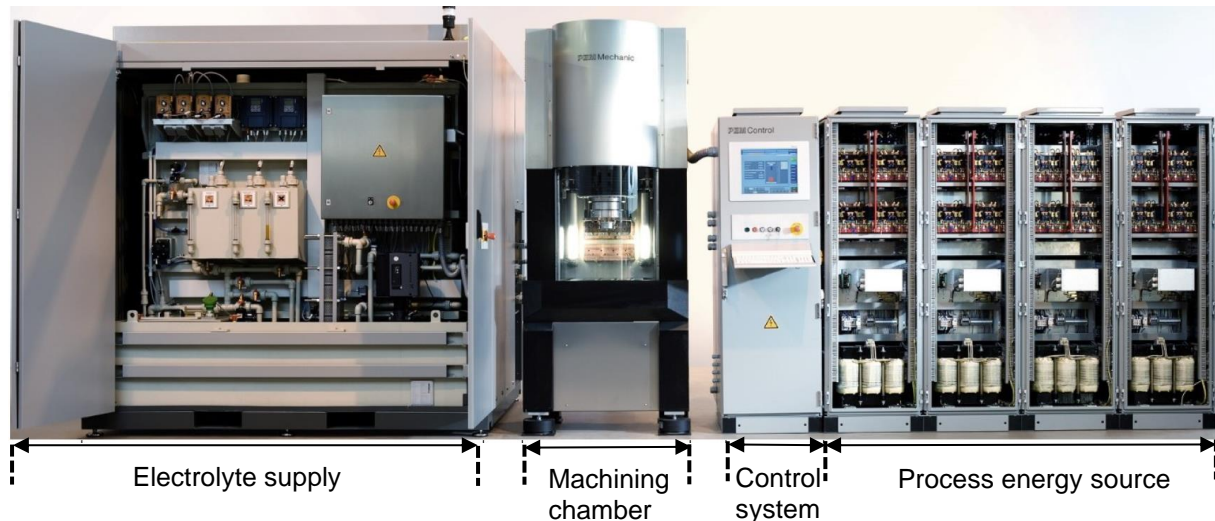
Figure 2-19: PECM machine PEMCenter 8000 with different operating groups [79].

In this machine, the electrolyte's pH, temperature, and conductivity are considered constant. Furthermore, there is a KEEP-Unit device that compensates for external electric potentials. The main technical information on the machine is given in Table 2-4.

Table 2-4: Technical Data of PECM machine PEMCenter 8000 [79].

Technical Data	
Current I [A]	1 – 8,000 (Pulsed)
Voltage U [V]	5 - 18.7
Pulse on time t_{on} [ms]	0.1 - 5
Mechanical Oscillation $f_{mechanic}$ [Hz]	0 - 60
Electrical pulsation without mechanical oscillation $f_{electric}$ [Hz]	1 - 500
Feed rate v_f [mm/min]	0.001 - 2
Electrolyte pressure [bar]	1 - 10
Vibration amplitude [µm]	183.5
Maximum travel [mm]	170

2.2.6 Electrolyte preparation

The electrolyte used is an aqueous solution with $NaNO_3$ and 80 mS/cm conductivity. As the electrolyte supply is 200 l, weighing the salt to find the concentration is difficult. Therefore, the conductivity is measured with the help of an electrical conductivity meter. The graph illustrated in Figure 2-20 is used to find the concentration used in the electrolyte preparation. The conductivity is correlated to the electrolyte's concentration, which increases with increasing conductivity. With 80 mS/cm of the conductivity used for this experiment, the concentration is derived around 1 M. The dissolution of $NaNO_3$ in water is an endothermic reaction. As a result, the temperature of the electrolyte decreases drastically, leading to a decrease in conductivity. To achieve the most accurate conductivity, a suitable time of stirring for the electrolyte is needed so that the electrolyte has the time to heat up to room temperature.
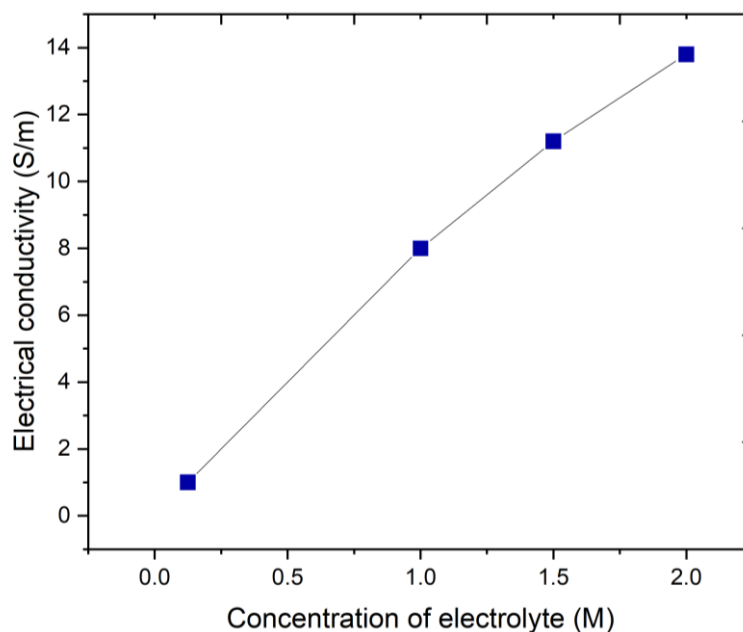
Figure 2-20: The tendency of electrical conductivities with concentration for $NaNO_3$ (Adapted from [80]). The concentration of $NaNO_3$ electrolyte increases by increasing conductivity.

The pH value is 8 at room temperature which is measured with the help of a pH meter mounted in the electrolyte's flowing path. During the experiments, the conductivity of the electrolyte, the pH value, and the temperature are measured continuously.

2.2.7 The setup used in industrial electrochemical machine

A developed setup is designed to have the proper flow of the electrolyte and be able to machine the hollow cylinder-anode with the tool. The upper parts of the setup used for PECM by the PEMCenter 8000 machine are shown in Figure 2-21. The electrolyte enters the flushing chamber from two symmetric inlets and flows downwards after filling the chamber. The flushing chamber is produced from Prusament PLA out of Prusa Polymers (polylactic Acid) by a 3D printer which is not electrically conductive. This PLA material is the most used filament, with good resistance against chemical agents and low thermal expansion. The interface between the tool-flushing chamber and workpiece-flushing chamber are sealed with sealing rings. A tool holder is used to keep the tool in the right place and help with the feed movement of the tool during the process. After some experiments with the setup, the sufficient thickness of the tool holder is designed. With this knowledge, a probable short circuit resulting from tool movement under the pressure of the electrolyte is prevented. The contact of the tool to the power supply is through the tool holder. The workpiece and the flushing chamber are fixed together against the electrolyte-flowing pressure by a stainless-steel part named "belt." In other words, with the help of this part, all setup components are kept constant from displacing during PECM.
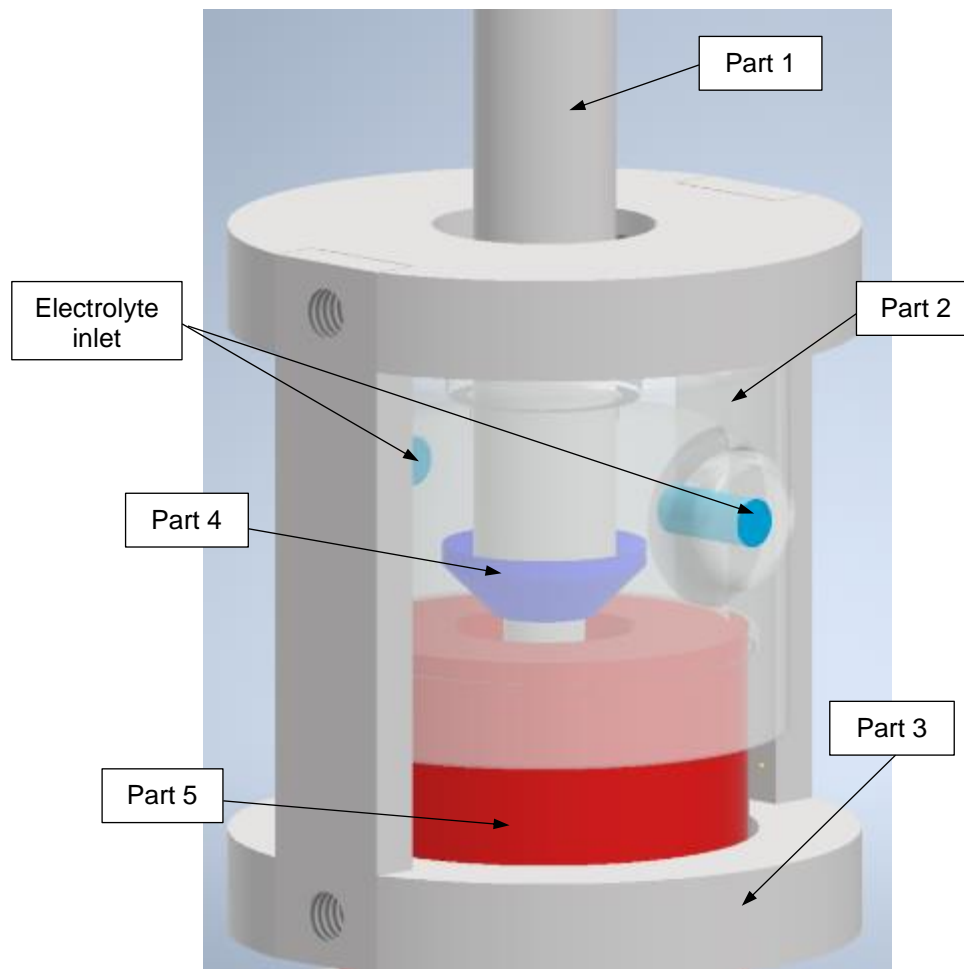
Figure 2-21: CAD model of the upper parts in the setup used for PECM by PEMCenter 8000,
Part 1. Tool holder to keep the tool in the center and make the feed movement of the tool possible,
Part 2. Flushing chamber, Part 3. Belt to keep the flushing chamber and other parts constant against
the pressure of flowing electrolyte, Part 4. Tool, and Part 5. Workpiece.

The inferior parts of the setup used for PECM by PEMCenter 8000 are shown in Figure 2-22. A stainless-steel fixture is designed with two tasks: keeping the workpiece fixed during the process and having an outlet for the electrolyte to flow out of the process area. The electrolyte passes the IEG and flows out of the anode from the fixture. Some openings are designed in the fixture as the outlet for the electrolyte so that the electrolyte flows out of the setup through them. The area where the anode is placed in the fixture is designed in the shape of a triangle to have a more accessible and better centering of the components. The connection of the workpiece to the power supply is made with the help of screws to the fixture. The whole setup is shown in Figure 2-23. The setup is mounted in the PECM machine. The drawings of the parts are available in APPENDIX.
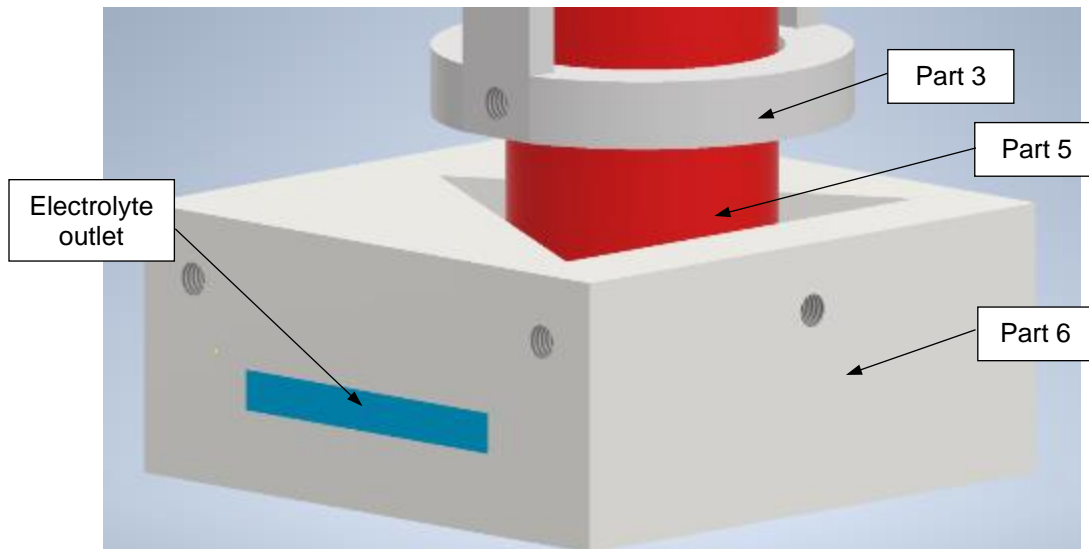
Figure 2-22: CAD model of the inferior parts in the setup used for PECM by PEMCenter 8000, Part 3. Belt to keep the flushing chamber and other parts constant against the pressure of flowing electrolyte, Part 5. Workpiece, and Part 6. Fixture to keep the workpiece in the center and connect the workpiece to the power supply.
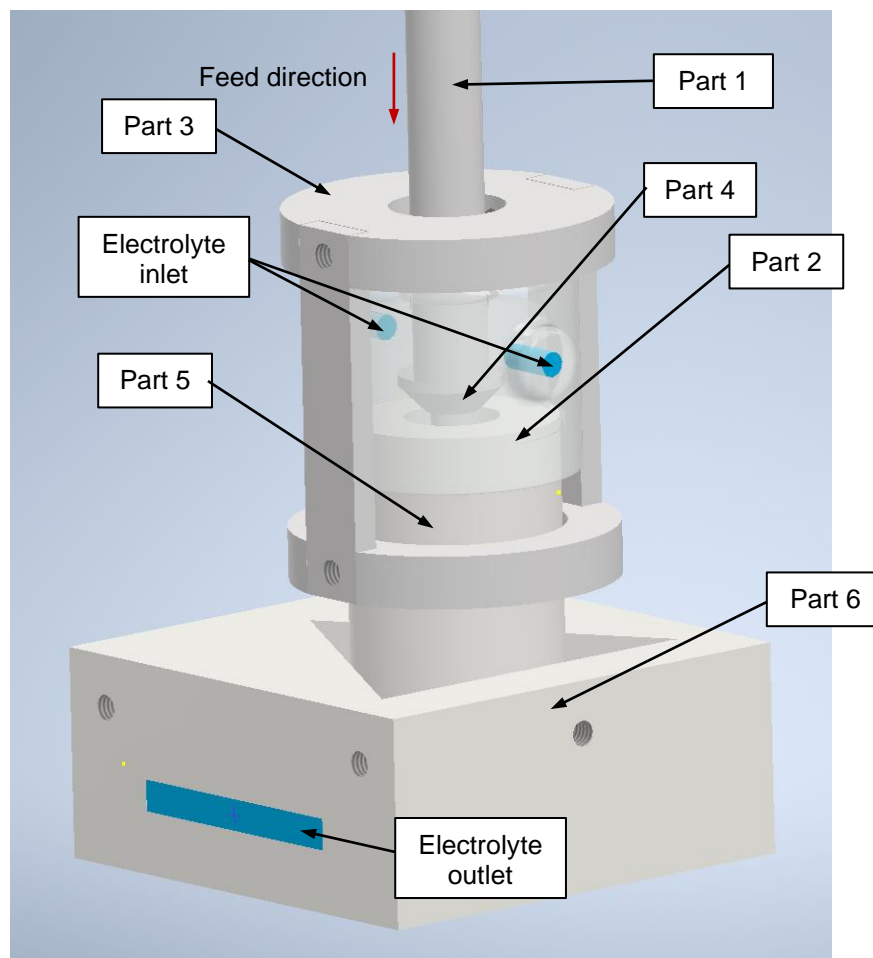
Figure 2-23: Experimental setup for PECM investigation, Part 1. Tool holder, Part 2. Flushing chamber, Part 3. Belt, Part 4. Tool, Part 5. Workpiece, and Part 6. Fixture.

Tool (1.4112 material) and workpiece (1.3505 material) are illustrated in Figure 2-24. The workpiece is a hollow cylinder with an inner diameter of 18 mm, an outer diameter of 40 mm, and a height of 65 mm. The inner diameter of the workpiece is widened with the tool with a diameter of 20 mm (the biggest diameter in the tool geometry) during PECM. The aim is to have the condition used in the production of paralloy ethylene profiled (PEP) tubes by PECM. PEP tubes are centrifugally cast tubes with a profiled inner diameter that maximize heat transfer in steam crackers [81]. PECM of the hollow cylinder is done in the industry to make profile on the inner diameter surface of the workpiece. In addition, having the hole in the cylinder before PECM decreases the work done by the PECM machine and the machining products.

The tool and the workpiece are machined to the desired geometry suitable for PECM by turning. The surfaces that are involved in electrochemical reactions are shown in red in Figure 2-24. The area labeled X in Figure 2-24 (a) is the region where surface analysis is done. The X area is out of the IEG and direct electrochemical process. As a result, less black coating is formed, making it easier to investigate this area. The black coating is discussed in chapter 3.3.2.

Moreover, because of the tool's geometry and workpiece, there is no possibility of damage on the tool in this area due to a short circuit. The real design of the setup while working in PEMCenter 8000 is shown in Figure 2-25.
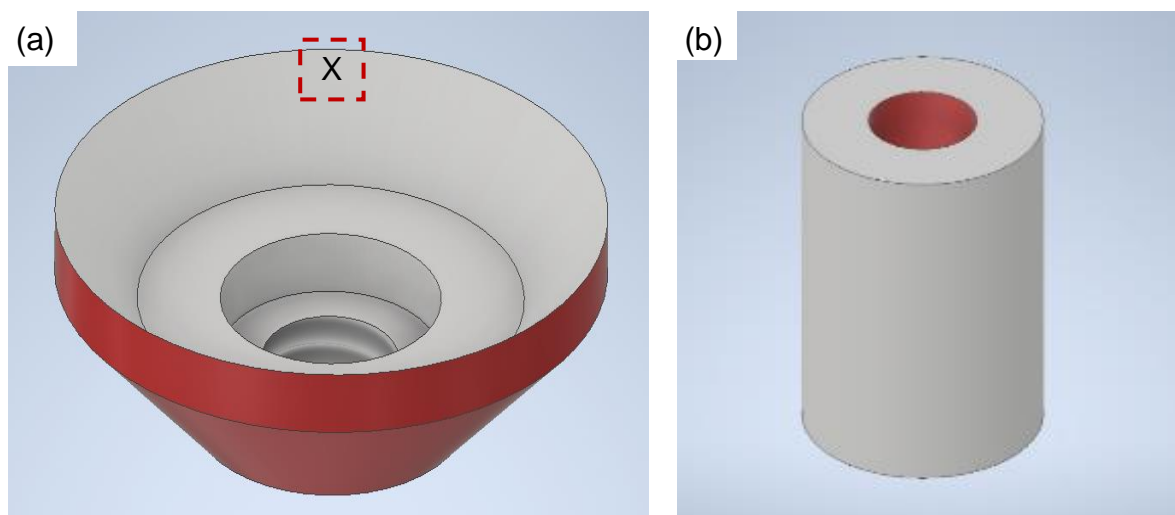
Figure 2-24: schematic design of (a) tool, the surface analyses are done in X area. (b) workpiece. Red surfaces are the involved areas in machining.
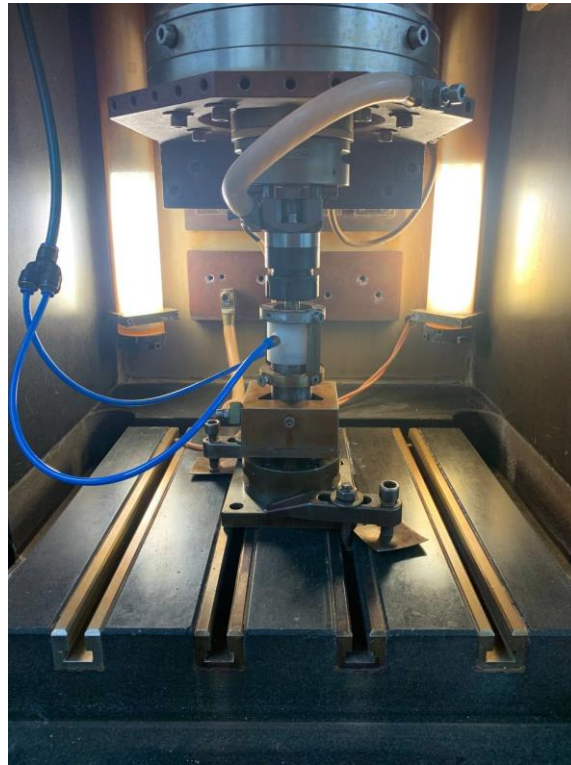
Figure 2-25: The setup used for PECM inside of PEMCenter 8000.

The processing area between the tool and workpiece is supplied with the electrolyte by downward flushing. To machine ferrous alloy, the aqueous electrolyte of $NaNO_3$ results in better dimensional accuracy by controlling stray current [2, 32]. As a result, aqueous $NaNO_3$ with 80 mS/cm conductivity is used. In the way of electrolyte circulation, a filter with the ability to remove particles bigger the 20 µm is used (Sediment filter).

Long-term machining is conducted to have the working condition close to industrial condition. A 60 mm length of machining in each cycle and 100 cycles is considered for long-term machining. A high feed rate is employed to make the machining faster by maintaining the constant machining state. It results in more precise machining geometry and a better finished surface due to decreased IEG [29]. The large IEG and high electrolyte pressure ensure no unwanted short circuits occur. The highest electrolyte pressure in the circulating electrolyte system available is 5 bar.

High voltages produce more hydrogen and reduce the conductivity of the electrolyte. On the other hand, in a study [82] done on 1.3505 as the workpiece, the range of voltage used is 12-16 V which, by increasing the voltage, better roughness on the workpiece is achieved. The voltage chosen for this study is 13 V to have a good

surface quality of the workpiece and material removal next to not excessive hydrogen production.

The employed machining condition is shown in Table 2-5. By having long-term machining, the electrolyte's features, such as temperature, conductivity, and pH, are affected. Consequently, the electrolyte was monitored all the time to be kept constant. The process is stopped after 2-3 cycles to let the electrolyte and setup cool down to get back to room temperature. The increasing pH is controlled by adding nitric acid to the electrolyte flow when the machine is not operating. After reaching the suitable pH, the machine runs again. When the conductivity of the electrolyte is changed, the electrolyte is renewed completely.

Table 2-5: Machining condition in $NaNO_3$ as electrolyte.

Parameter	Value	Unit
Electrolyte	$NaNO_3$	
IEG	0.750	mm
Feed rate	0.950	mm/min
Machining depth	60	mm
Voltage	13	V
Electr. frequency	90	Hz
Phase	50	%
Electrolyte pressure	5	bar
pH	8±1	
Conductivity	80±5	mS/cm
Pulse duration	2	ms
Cycle	100	
Temperature	Ambient±5	°C

2.2.8 Electric field simulation

Calculating the current density gives a good overview of ECM and PECM. To calculate the current density, the area of the anode and current are needed. Regarding the shape of the tool and workpiece, it is complicated to calculate the area of the anode involved in PECM. The distribution of the electric field illustrates the

exact areas which are involved in the machining. Consequently, 2D simulation is used to find the surfaces forming the electric field. The electric field is the basis for electrochemical reactions, which are based on Maxwell's equations and the continuity equation of charge:

$$\vec{\nabla} \cdot \vec{J} = -\frac{\partial \rho}{\partial t}$$

2-34

which ρ is the local electric charge and $\vec{J}$ is the divergence of the vector of current density. By neglecting the magnetic field, the electrical field $\vec{E}$ is defined:

$$\vec{E} = -\vec{\nabla}V$$

2-35

Then the vector of current density is:

$$\vec{J} = \sigma\vec{E} + \frac{\partial\vec{D}}{\partial t} + \vec{J}_e$$

2-36

which σ is the specific conductance, $\vec{D}$ is the electric displacement, and $\vec{J}_e$ is the external vector of current density. $\vec{J}_e$ is equal to zero for ECM as just external voltage is applied. Then there is:

$$\vec{D} = \varepsilon_0\varepsilon_r\vec{E}$$

2-37

which ε_0 is the electric field constant and ε_r is the material-dependent relative permittivity. Considering all the above [23]:

$$\vec{J} = (\sigma + \varepsilon_0\varepsilon_r\frac{\partial}{\partial t})\,\vec{E}$$

2-38

Simulation is done by COMSOL Multiphysics Academic Classkit License at Saarland University. The approach is a stationary simulation for a 2D symmetrical model, and the physic is electric currents. It is considered that all the changes on the tool are neglectable. To be able to have a more precise model of the workpiece, the cross-section of the workpiece in the IEG after PECM is observed. The machined cross section of the workpiece is shown in Figure 2-26. The angle of the surface is measured 131.26 deg, which is considered 135 deg during simulation for simplicity. It shows that the model is almost similar to the PECM results.
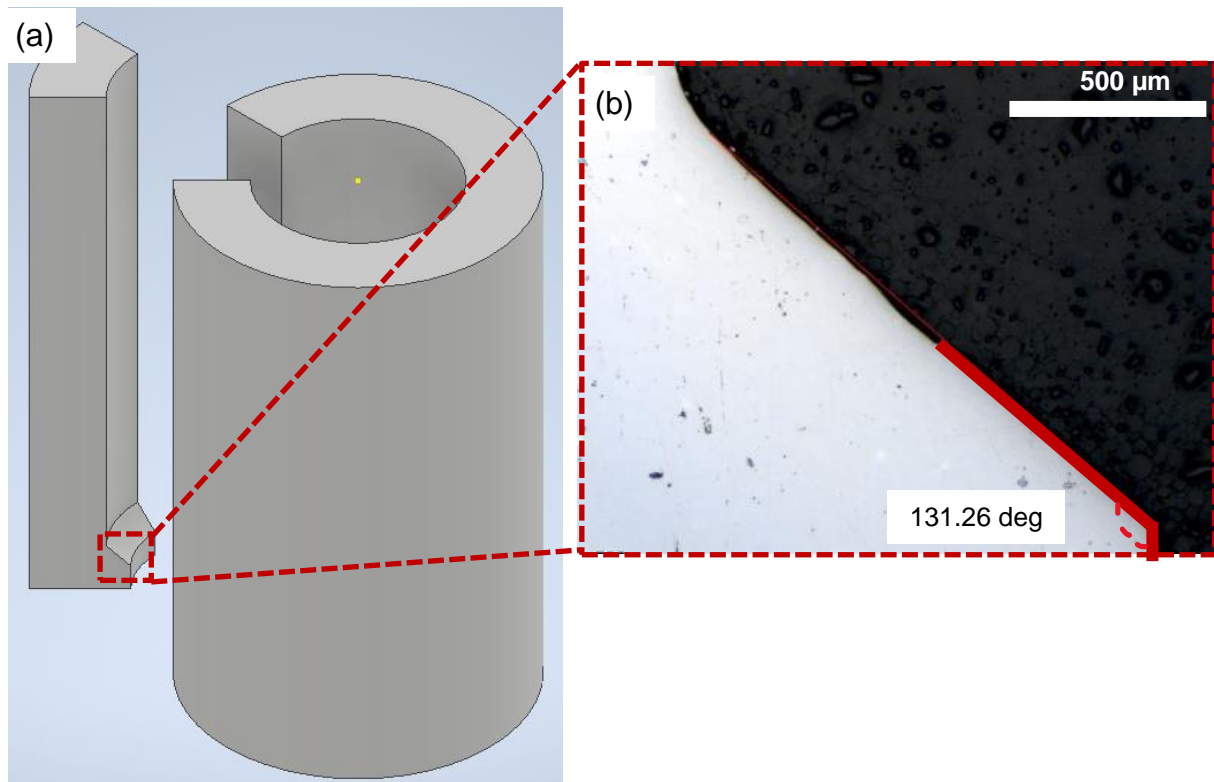
Figure 2-26: (a) Vertical cut of the workpiece after PECM (b) optical microscopic image of the machined cross-section of the workpiece after PECM.

The boundary condition is derived from Table 2-5 and is shown in Table 2-6.

Table 2-6: Definition of boundary conditions in COMSOL Multiphysics.

Boundary	Definition	Value
1	Electric insulation	
2	Electric potential	U = 13 V
3	Ground	U= 0 V
4	Axial Symmetry	

Therefore, the tool is assumed as the ground (dash line), and the workpiece has an electrical potential of 13 V (solid line), as shown in Figure 2-27 (a) [83]. Meshing is physic-controlled with normal size, which leads to having finer mesh in the tool, workpiece, and electrolyte in the IEG, as is shown in Figure 2-27 (b).
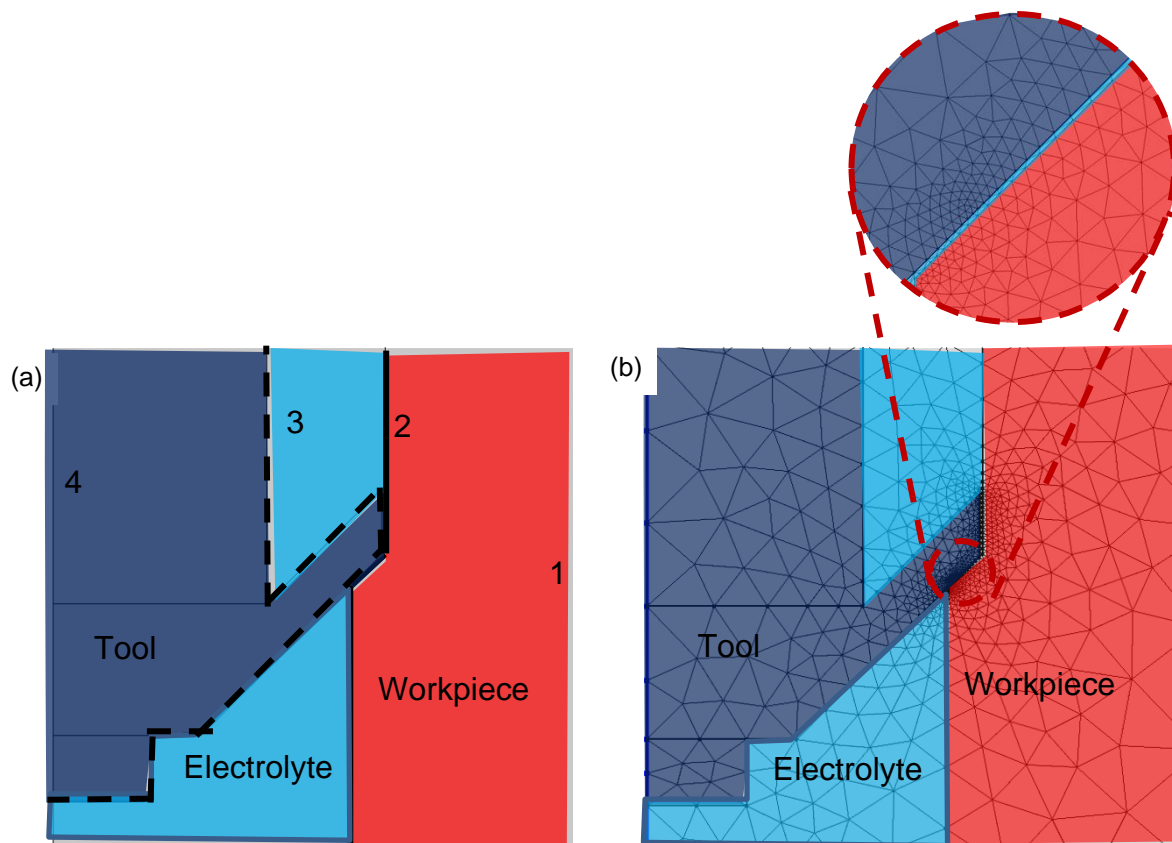
Figure 2-27: (a) boundary condition (b) mesh distribution in the stationary simulation of ECM. The red color is the anode, and the dark blue color is the cathode.

The current density is calculated by Equation 2-19. The current flowing during the process is recorded by an integrated measuring unit in the PEMCenter 8000 machine, and the output is the average current per processing pulse.

2.2.9 Measurements and technology

Surface Analysis

The samples after PECM are cleaned in an ultrasonic cleaning machine in alcohol. The surface of the samples and the changes are investigated by means of different microscopes, namely FESEM (ZEISS SIGMA) at the Institute of Material Science and Methods and digital microscope (KEYENCE VHX-7000) at the Institute of Production Engineering, Saarland University. A secondary electron detector (SE) is used for FESEM microscopy. It should be mentioned that the whole surface analysis is done on the inner side of the tool, which is facing electrolyte flow (labeled X in Figure 2-24 (a)).

2.3   Process effects

2.3.1   Tool surface

Figure 2-28 shows the digital microscopic images in the X-marked area on the tool's surface (marked in Figure 2-24) machined by PECM with PEMCenter 8000 after 100 cycles. The tool's surface before PECM in Figure 2-28 (a) has grooves due to the tool's manufacturing process before PECM. These grooves become smoother after PECM in Figure 2-28 (b). In addition, the formation of the pits after PECM is observed.
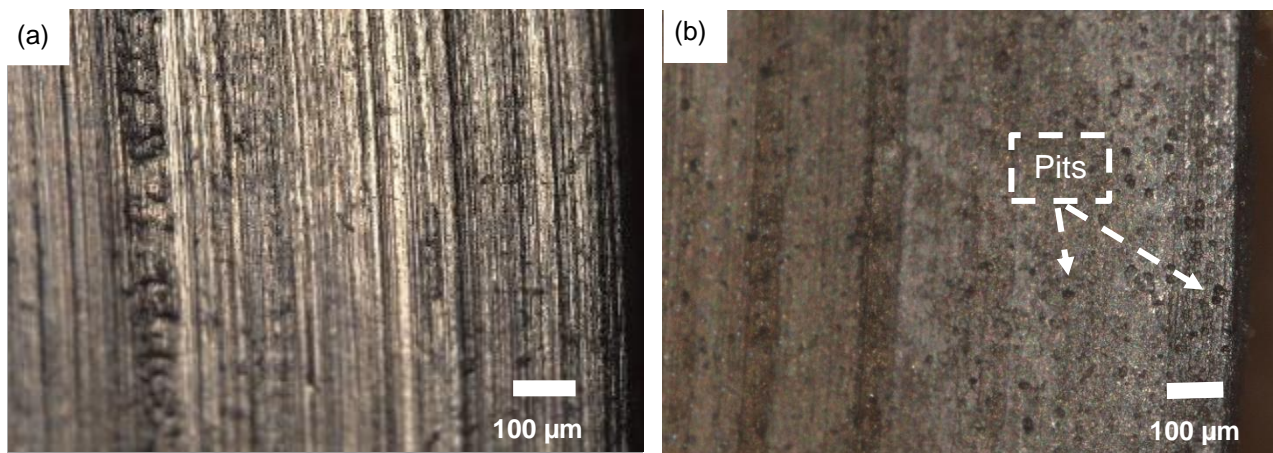
Figure 2-28: X area on the surface of the tool (a) before PECM; the grooves are the results of the manufacturing process before PECM. (b) after PECM; the grooves almost disappear and some pits are formed.

Figure 2-29 shows the FESEM images, illustrating the tool's surface before and after PECM in the X-mark area. Figure 2-29 (a) and (c) show the tool's surface with different magnifications before PECM. The surface looks without any pits. The manufacturing process lines on the tool's surface are visible. Figure 2-29 (b) and (d) show the tool's surface with different magnifications after PECM. The pits are formed on the tool's surface after PECM from about 17 µm to less than 4 µm ranging in size. The black spots on the tool's surface after EPCM are either contamination or partially formed black coating. Considering the motivation of this study in chapter 2.2.1, the three hypotheses (hydrogen embrittlement, cavitation erosion, and cathodic corrosion) are investigated as the reason for pits formation in further chapters.
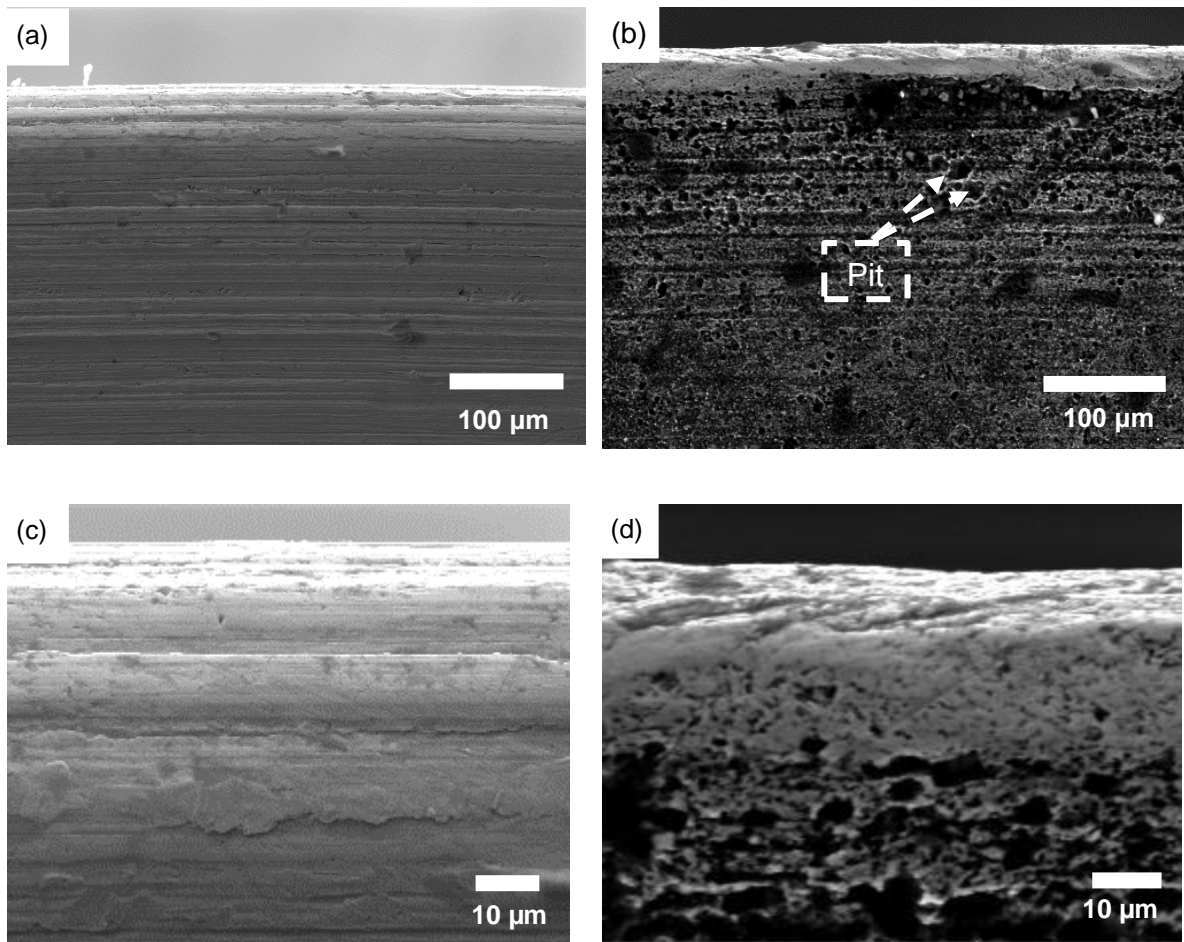
Figure 2-29: Surface of the tool 1.4112 (a) pre-PECM (b) after PECM with oscillation of the tool in lower magnification. (c) pre-PECM (d) after PECM with oscillation of the tool in higher magnification. The formation of the pits after PECM on the surface of the tool is shown.

2.3.2 Electric field simulation

Complexity in the tool and workpiece shape makes it difficult to calculate the current density. As a result, the active area of the tool and workpiece in PECM is approximately obtained with the help of simulation. The result shows that the electrical field is concentrated mostly in the frontal and side gaps (Figure 2-30). The electric field in other areas is close to zero, and it is possible to relinquish it.
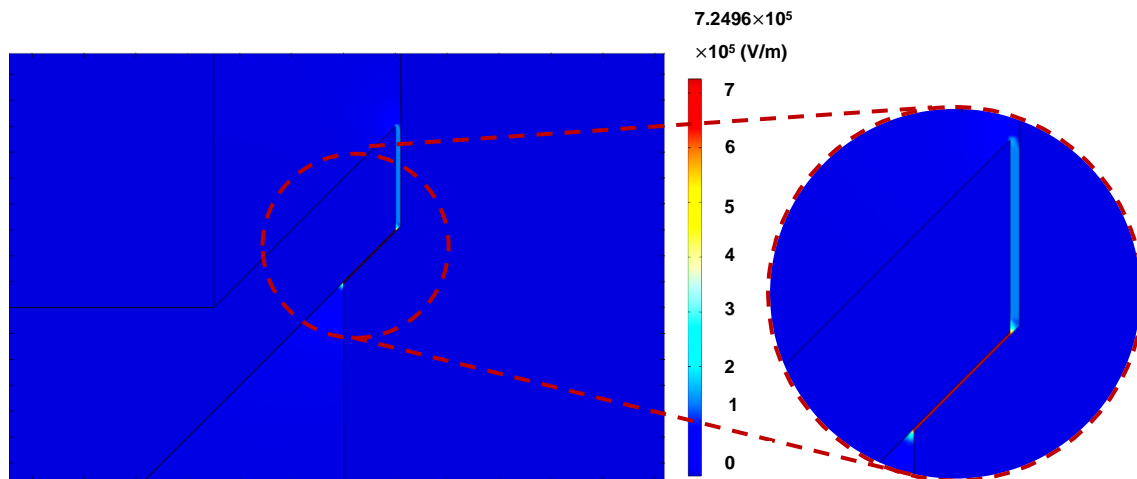
Figure 2-30: Electric field dissipation in the machining zone concentrated mostly in the IEG.

This result is used to find the surface area involved in the electrochemical process. The zones producing electric fields are shown with a yellow dashed line in Figure 2-31.
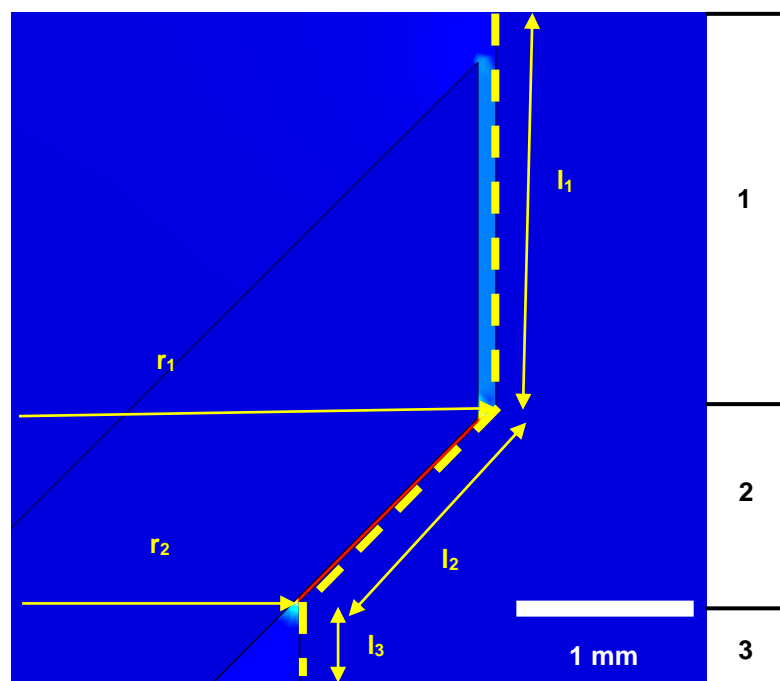
Figure 2-31: Zones on the workpiece involved in making an electric field during ECM used to calculate the area. Areas 1 and 3 make rectangular. Area 2 makes conical frustum.

The area is calculated by dividing the shape into three zones marked 1, 2, and 3. By assuming the workpiece on 2D, zones 1 and 3 make rectangular. The lengths are the inner diameters of the workpiece, and the widths are the longitude making electric field in Figure 2-31. The areas are calculated by:

$$Area = 2\pi rl \qquad\qquad 2\text{-}39$$

In zone 1, $r_1 = 10.1$ mm and $l_1 = 2$ mm, then:

Area zone 1 = 126.92 mm^2

In zone 3, $r_2 = 9$ mm and $l_3 = 0.5$ mm, then:

Area zone 3 = 28.275 mm^2

Zone 2 is considered conical frustum. The area is calculated as follows:

$$Area\ zone\ 2 = \pi\ (r_1 + r_2)\ l_3 \qquad\qquad 2\text{-}40$$

The longitude of making an electric field is calculated by Pythagoras' Theorem:

$l_3 = 1.49$ mm

As a result:

Area zone 3 = 89.41 mm^2

Total area = 244.605 mm^2

The current is obtained from the PECM based on Table 2-5. The current density is calculated by Equation 2-17 and the average current density as a solid line with standard deviation as a band is shown in Figure 2-32. The current density increases over a long time PECM from 121.2 A/cm^2 to 126.9 A/cm^2 as the mean value, which is because of having a conductive tool holder. The tool holder made the connection of the cathode and the feed of the cathode possible and, over time, entered more inside of the anode, increasing the tool's area involved in PECM. In addition, the long-term machining for each cycle increases the temperature of the electrolyte. The increase in the temperature based on Equation 2-31 increases the conductivity and, consequently, the current density. The effort during PECM is to keep the temperature constant over time, but during this experiment, the absence of cooling for a low volume of electrolyte (200 l) is considered as a limitation.
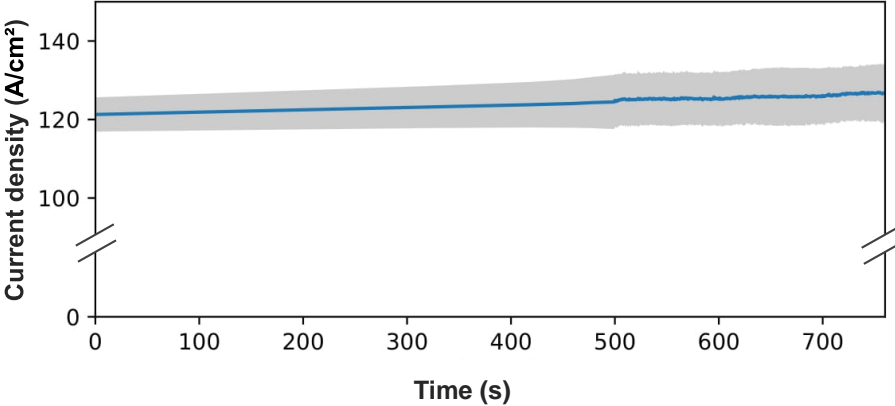
Figure 2-32: Current density vs. time of PECM process in a cycle. The error band is acquired by considering 100 cycles.

3 Hydrogen Embrittlement

3.1 Literature review

Hydrogen in metals reduces mechanical properties and causes phenomena such as hydrogen embrittlement, hydrogen cracking, and blistering. Hydrogen embrittlement is important and common during electrochemical processes [84]. The damage caused by hydrogen was first observed on iron and steel in the early 1870s. The first explanation was proposed, "hydrogen in interspaces impeding the movement of iron molecules" [85]. Since then, by improving advanced characterization techniques, intensive efforts have been made to understand the phenomenon of hydrogen embrittlement. It is reported that around 25% of equipment failure in the petroleum refining industry results from hydrogen embrittlement [86].

It is accepted that more than one mechanism can be the reason for failure based on hydrogen embrittlement [72, 87]. For example, the formation of hydride and cleavage mechanism is defined for pure metals and their alloys, as well as in titanium and zirconium. There can be even more than one mechanism activated for these materials. Finding the mechanism is a complex, multi-faceted challenge that requires knowledge of the hydrogen source, the interaction of hydrogen with the oxide layer on the metal, the diffusion of hydrogen into the metal, the interaction of hydrogen with microstructural features, loading during diffusion, and other properties. The proposed mechanisms are [87]:

- High hydrogen pressure bubble or void.
- Hydrogen-induced reduction in surface energy.
- Hydrogen-enhanced dislocation ejection from the surface or near-surface region.
- Hydrogen-induced reduction in cohesive strength.
- Hydrogen-enhanced localized plasticity.
- Hydrogen- and deformation-assisted vacancy production.
- Hydrogen-triggered ductile to brittle transition.
- Hydride formation and cleavage.
- Hydrogen- and strain-induced phase transformations; and
- Reactants and hydrogen.

Hydrogen atoms on the surface of a solid often form gaseous hydrogen molecules, which leave the surface without causing any problems. The rest of the hydrogen atoms stay in an atomic state and penetrate the metal [88]. There are three prerequisites needed to have a failure because of hydrogen embrittlement [89]:

- Metal condition (susceptibility to the diffusion of hydrogen)
- Atomic hydrogen
- Tensile stress (with two originating sources: outside or inside of the metal)

High-strength materials are more susceptible to hydrogen embrittlement. The hydrogen concentration of 0.5 – 1 ppm (wt.) in ultra-high-strength materials, namely martensitic steels, is enough to cause damage or crack. For materials with lower strength, such as ferritic steels, a higher hydrogen concentration (~10 ppm) is necessary to cause hydrogen embrittlement [72].

Hydrogen embrittlement occurs by absorbing the hydrogen into the surface of the metal. The source of hydrogen can be the atmosphere or a medium. In the atmosphere, hydrogen exists as a molecule in the gas phase. At room temperature and atmospheric pressure in the source of the atmosphere, the thermodynamic driving force to change the molecules of hydrogen to atoms is not enough. As a result, hydrogen absorption is low. With high pressure of over 100 bar in pure hydrogen gas, the adsorption of the hydrogen molecules occurs. Hydrogen diffusion in partially high pressure included three steps (Figure 3-1): deposition, dissociation, and absorption [90]. By deposition, the hydrogen molecule adheres to the steel's surface. The dissociation of the hydrogen molecule causes the atomic hydrogen, which shows the adsorption of atoms. The last step is absorption, completing the diffusion by entering the atomic hydrogen into the steel.
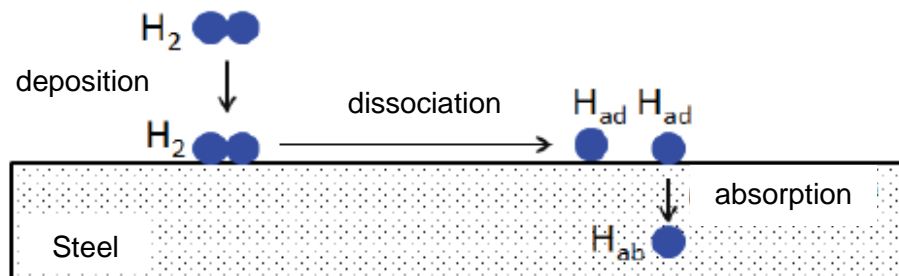
Figure 3-1: Three steps of hydrogen absorption from the atmosphere into the metal [91].

Diffused hydrogen moves between interstitial lattice sites and becomes trapped in lower potential energy relative to normal interstitial sites. Other trapping sites with

different trapping energies of hydrogen are some solute atoms, free surfaces and sites between the first few atomic layers beneath surfaces, mono-vacancies and vacancy clusters, dislocation cores and strain fields, grain boundaries, precipitate/matrix interfaces and strain fields around precipitates, inclusion-matrix interfaces, and voids and internal cracks [72]. The hydrogen trapping sites are shown in Figure 3-2.

(a)

Adsorbed H

Grain boundary

H+vacancy

Normal interstitial lattice site

H at dislocation core and H atmosphere

(b)

Plate

H and H_2 trapped at delaminated interface

H trapped at particles and inclusion interfaces

H filled grain-boundary nano-scale bubbles

H_2 in cracks or voids

Adsorbed H at internal crack tip
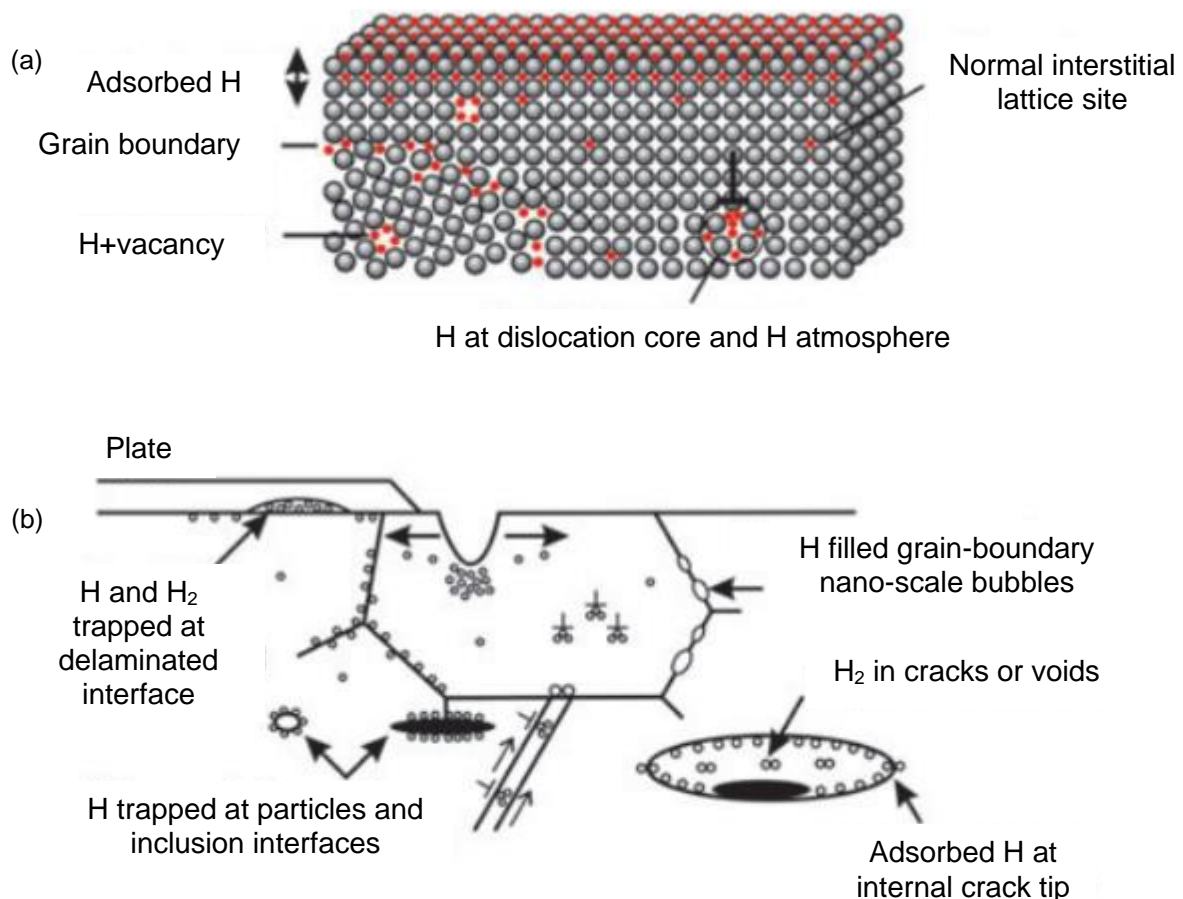
Figure 3-2: Trapping site of hydrogen in metal (a) on the atomic scale (b) on the microscopic scale [72].

The hydrogen diffusion rate depends on the crystal structure at ambient temperature. This rate is four to five orders faster in body center cubic (BCC) metals than in face center cubic (FCC) and hexagonal close pack (HCP) metals at ambient temperature (Figure 3-3) [72, 92]. However, Pd with FCC and Co with HCP structure are exceptions. The hydrogen diffusion rates in these materials are much faster than FCC structure. In iron with BCC structure, the hydrogen diffusion distance with the diffusion rate of 10^{-5} cm^2/s is about 50 µm in 1 s. Whereas the hydrogen diffusion

distance in nickel with FCC structure and diffusion rate of 10^{-10} cm^2/s is about 0.1 μm [72].
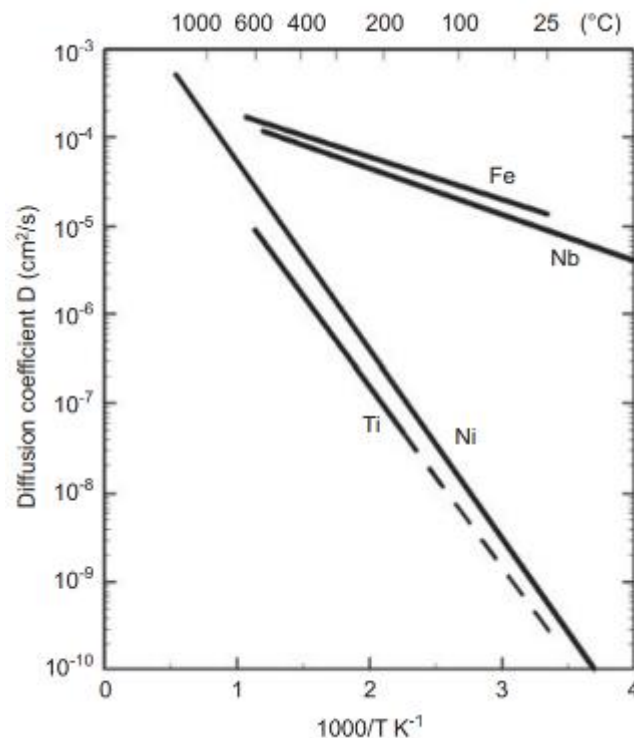
Figure 3-3: Hydrogen diffusion coefficients for Fe and Nb (bcc), Ni (fcc), and Ti (hcp) vs. temperature [72].

Iron and its alloys have many interstitial sites for hydrogen to diffuse. This hydrogen is called dissolved hydrogen. Additionally, steels have defects in their microstructures which interacts with hydrogen. This hydrogen is called trapped hydrogen [86]. Steels with higher strength have lower effective diffusion coefficients because of a larger volume fraction of carbide strengthening phases and a higher dislocation density. By increasing temperature, hydrogens diffusion increases. As a result, more hydrogen can leave the traps at higher temperatures. Baking steel at higher temperatures is a method of preventing hydrogen embrittlement.

Based on the source of the hydrogen, there are two types of hydrogen embrittlement. The first is during steel making or processing, resulting from water dissociation on the surface, and the second is the result of hydrogen absorption from an external source. Diffusible atomic hydrogen is produced and penetrated during coating, plating, cathodic electrochemical reactions, some corrosive mediums, ECM, cathodic protection, welding, roll forming, heat treatment [70], or cleaning where hydrogen

bubbles are formed at the cathodic surface of the steel. In some cases, hydrogen absorption occurs during service because of cathodic corrosion reactions. During ECM, the cathode might be the target for produced hydrogen to diffuse [93]. In such processes with cathodic charging, current density plays an important role. Higher current density leads to higher diffusion of hydrogen into the material [94].

Without tensile stress, hydrogen embrittlement degradation is not possible. When there is biaxial strain, where major and minor stresses are both tensile stresses, degradation of the material because of hydrogen embrittlement is more significant. Avoiding high local tensile stress or modifying the tensile stress to be compressive stress secures the material from hydrogen embrittlement [90].

The tensile stress is imposed by the environment during service or is residual tensile stress. Machining processes, such as turning, milling, and drilling, often make the residual tensile stress needed for hydrogen embrittlement [95]. After these machining processes, a white layer might form on the surface, and tensile residual stress is produced on the surface and immediately become compressive beneath the surface. That amount of residual tensile stress will be sufficient to initiate some damages like hydrogen embrittlement [96-99]. Grains and microstructure are not visible in the white layer with an optical microscope [100]. This layer forms mostly on difficult-to-machine alloys such as high-strength steel. It is reported that three mechanisms are involved: phase transformation, severe plastic deformation with dynamic recrystallization, and chemical surface reactions [101, 102]. Sometimes more than one mechanism is involved. In addition, the white layer is refined to nano-size grains [101].

Residual stress is compressive or tensile based on the mechanism involved. When the dominant mechanism is the thermal mechanism, tensile residual stress is produced. The heat generated during machining is the result of plastic deformation and friction which creates a thermal phenomenon. The portion of the heat conducted with the workpiece produces residual tensile stress. In Figure 3-4, the mechanism of producing residual tensile stress is shown. Heat is generated when the cutting edge is in contact with the metal's surface, leading to a temperature gradient. When the cutting edge moves away, the surface cools down, and heat dissipates reversely to the temperature gradient. The surface is cooled though the layers beneath are still hot. As a result, the shrinkage of the outer zone is prohibited, and residual tensile stress forms. Phase transformation or dynamic recrystallization also produces residual stress as thermal actions [103].
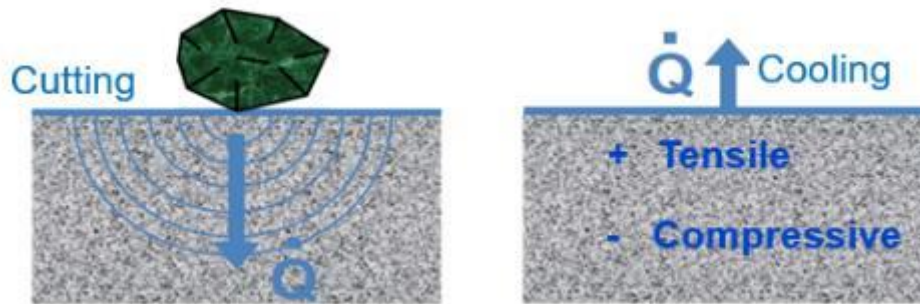
Figure 3-4: Mechanism of producing residual tensile stress by machining process as a result of heat generation and temperature gradient.

3.2 Experimental

3.2.1 Hydrogen embrittlement

To investigate hydrogen embrittlement, three prerequisites are studied. The metal condition is studied with the help of microstructural characterization methods such as FESEM and XRD to determine the tool's susceptibility to hydrogen embrittlement. The microstructure defines the condition which is necessary for the diffusion of hydrogen. The hydrogen source is investigated with the help of FESEM, electron backscatter diffraction (EBSD), XRD, and thermal desorption spectroscopy (TDS) to find the probability of hydrogen diffusion into the tool and the amount of hydrogen. The tensile stress investigation is divided into two groups: an external source (from the environment) and an internal source (residual tensile stress).

The internal source is investigated with the help of XRD to find the amount of residual stress caused by the turning process before ECM. The stress value is measured to 50 µm depth in each step of about 5 µm. Two directions are considered for XRD: parallel and normal to turning direction. The external source is investigated with the help of fluid-solid simulation, as electrolyte flow imposes stress on the tool.

Fluid-solid simulation

Autodesk, with a free student license, is used to fulfill fluid-solid simulation. The first step is to design the parts in Autodesk Inventor. The design is derived from the real working setup, but it is simplified, as seen in Figure 3-5.
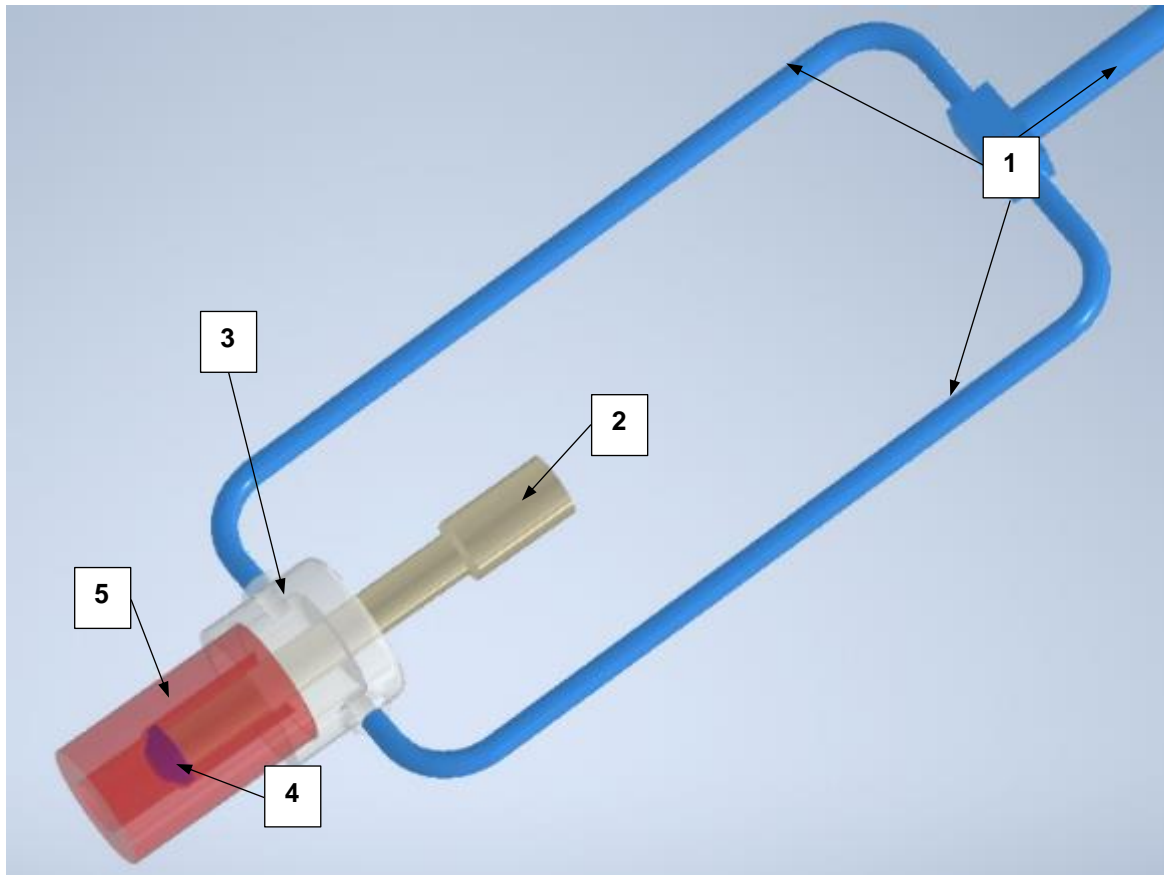
Figure 3-5: CAD design of setup used in the PECM machine 1. Electrolyte piping system 2. Tool holder, 3. Flushing chamber 4. Tool 5. Workpiece.

The design is imported into Autodesk CFD. As the electrolyte flushes away the ECM products and their volume ratio is so small, their effect is considered zero. The electrolyte is assumed incompressible and laminar. Then:

$$\rho u \cdot \nabla u = \nabla[-PI + \mu(\nabla u + \nabla u)^{T}] + F \qquad \text{3-1}$$

P is the pressure of the electrolyte, ρ is electrolyte density, u is velocity, T is temperature, I is the identity matrix, μ is the electrolyte viscosity, and F is the volume force that is small enough between electrodes and electrolyte to neglect [104]. The boundary condition and material, defined based on Table 2-5, are shown in Table 3-1.

Table 3-1: Definition of boundary conditions in Autodesk CFD.

Boundary	Definition	Value
Inlet	Pressure	5 bar
Outlet	Pressure	0 bar

The result of CFD is imported to Autodesk Nastran as the load. The whole design is assumed constraint without the degree of freedom, and mesh tolerance is 0.0001 m. The finer mesh size is applied to the tool because the result in the tool is important.

3.2.2 Measurements and technology

Surface analysis

The samples are cleaned in an ultrasonic cleaning machine with alcohol. The surface of the samples and the changes are investigated with the help of FESEM (ZEISS SIGMA), SE, EBSD, and energy dispersive spectroscopy (EDS) detector by Oxford Instruments X-Max at the Institute of Material Science and Methods, Saarland University.

X-Ray Diffraction (XRD)

XRD is used for two purposes: residual stress detection and phase analysis. To fulfill the residual stress detection, XRD Eigenmann 3000 PTS, at the Institute of Quality, Modeling, Machining, and Material, University of Applied Sciences Kaiserslautern, is used. To use this device, a Cr tube, polycapillary optics, and a line detector are used. Phase analysis has been done by XRD PANalytical Empyrean at the Institute of Functional Material, Saarland University. To use this device, a Cu tube, low background optics, and a multi-channel semiconductor detector (PIXcel) are used.

Thermal Desorption Spectroscopy (TDS)

TDS involves the measurement of the hydrogen desorption flux under controlled temperature ramping conditions. Gas chromatography or mass spectroscopy is used to quantify the hydrogen. The working temperature is 650 °C. The test is done by Aktien-Gesellschaft der Dillinger Hüttenwerke, Germany.

3.3   Results and discussion

As PECM is based on electrochemical reactions which produce hydrogen on the cathode, hydrogen embrittlement is the first hypothesis. The mentioned three prerequisites are investigated in this chapter. If all these three meet simultaneously, hydrogen embrittlement could be the reason for damage to the tool.

3.3.1   Metal condition

Figure 2-16 and Figure 2-17 show the cathode material's microstructure and phases before PECM. There is ferrite as the matrix with chromium carbides. As the sample is in the annealed condition, no martensite is observed.

Ferrite is BCC in structure. There is a lower hydrogen solubility in ferrite and a higher diffusion rate through the material because of an open lattice structure. As a result, ferrite is more sensitive to a small amount of hydrogen in the environment [105]. Local hydrogen accumulation at boundaries between the carbides and ferrite matrix can occur [93].

3.3.2   Atomic hydrogen

One possible reaction done at the surface of the cathode is hydrogen gas evolution [46]:

$$2H_2O + 2e^- \rightarrow 2OH^- + H_2 \qquad\qquad \text{3-2}$$

This reaction is the hydrogen source that penetrates the metal if the condition of the metal is in favor of hydrogen diffusion. The hydrogen reaches weak traps as highly stressed sites and is the reason for hydrogen embrittlement [106].

Kernel Average Misorientation (KAM) on the cross-section of the cathode before PECM helps to understand the condition of the tool for hydrogen diffusion. The KAM image is presented in Figure 3-6. Smaller grains at the surface result from dynamic recrystallization, which takes place on the tool after the turning process [107]. Some smaller grains are marked with red and labeled "A" in Figure 3-6. High KAM value is located close to grain boundaries of small grains at the surface and inside of bigger grains beneath the surface. Having a high KAM value is evidence of having more dislocations. Dislocations are proper places for hydrogen to diffuse into the sample [108, 109].
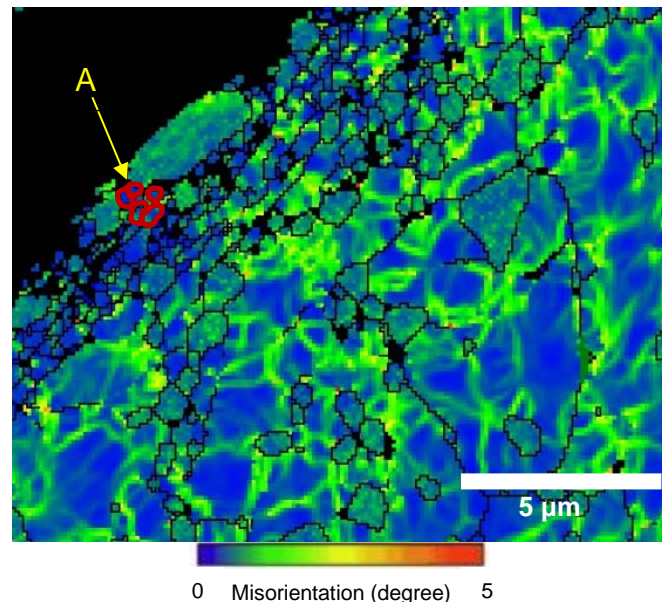
Figure 3-6: KAM value of cathode's cross-section PECM. "A" shows the small grains at the surface. The high KAM value in small gains on the surface is located close to the grain boundaries and in bigger grains beneath, is inside of the grains.

In addition, after some cycles of PECM, a black coating is formed on the surface of the cathode. EDS of the black coating is shown in Table 3-2. It is mostly the oxide of iron. The XRD result in Figure 3-7 shows that the black coating is composed of magnetite (COD code: 96-900-5813). Hydrogen diffusion is enhanced on the passive layer of magnetite because the hydrogen evolution mechanism increases hydrogen adsorption. The hydrogen adsorption on the iron surface without the passive layer is lower [109]. Other peaks shown in the XRD results are related to iron from the substrate (COD code: 96-901-3474)

Table 3-2: EDS result of the black coating formed on the cathode after some cycles of PECM.

Element	(wt.%)
Fe	63.5
O	16.8
Cr	11.8
Mg	4.7
Na	1.5
Mn	0.6
Si	0.5
AL	0.4
Other	rest
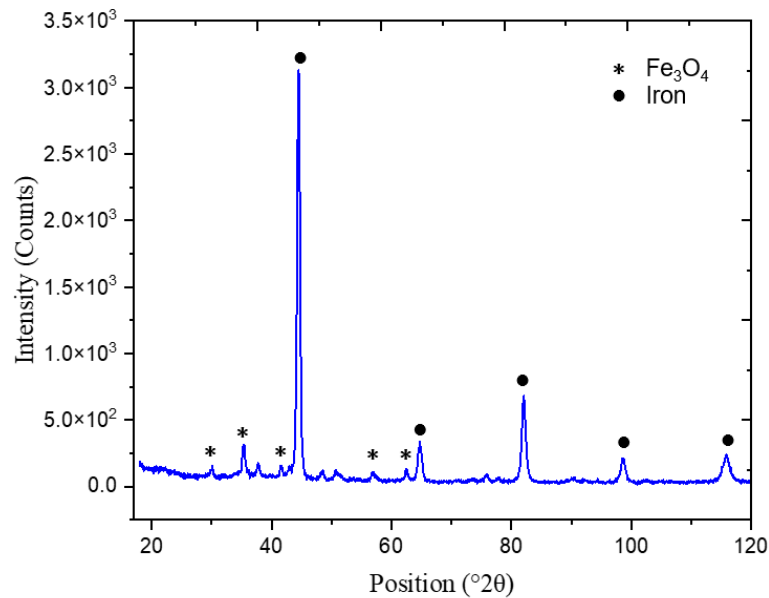
Figure 3-7: XRD result of the black coating formed on the cathode after some cycles of PECM showing formation of the magnetite. Iron's peaks are related to the substrate.

The electrochemical condition of the cathode depends on the composition and properties of the relatively thin layer of the electrolyte in the interface of the cathode and the electrolyte. Electrons released by the anode are consumed for the reduction reactions at the cathode. Depending on the electrolyte and cathode condition, different reactions occur on the cathode. In this study, considering an alkaline solution as the electrolyte, oxygen reduction occurs [110]:

$$2H_2O + O_2 + 4e^- \rightarrow 4OH^-$$ 3-3
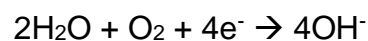
The former reaction is the reason for the alkalization of the electrolyte next to the surface of the cathode. Figure 3-8 shows the Pourbaix diagram for Iron. By increasing the pH, the oxide and hydroxide of the Iron are more stable in the negative range of potential. The stable oxide is magnetite which correlates to the XRD result in Figure 3-7. In high potentials, magnetite does not have the protection function [111].
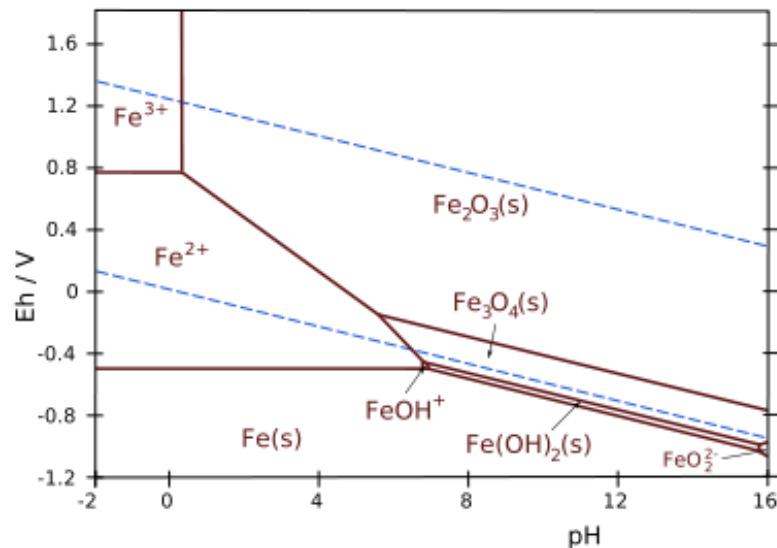
Figure 3-8: Fe-Pourbaix-diagram [112]. Formation of magnetite in high pH and negative potential.

TDS is done in 650 °C, and the result shows the amount of 6.8 ppm hydrogen within the sample. A threshold amount needed for hydrogen embrittlement is rarely mentioned in literature as different parameters like sample size and strength are important. Based on industrial experiments, considering the small sample used in this study, micro-cracks and damages could be generated with 6.8 ppm hydrogen in the sample [113].

3.3.3 Tensile stress

Without tensile stress, no damage due to hydrogen embrittlement occurs on the sample. There are two sources for tensile stress: tensile stress imposed from the environment and residual tensile stress.

Environmental tensile stress

Fluid-solid simulation is fulfilled to find the effect of electrolyte flow on the tool during PECM. The result of the CFD simulation is shown in Figure 3-9. The velocity

increases by entering the IEG and, by removing, decreases. The maximum velocity is 1500 cm/s and concentrates in the side IEG between the tool and the workpiece. The electrolyte velocity looks asymmetric though the model is symmetric. It is due to an effect in fluid named Coanda effect. Basically, air or other fluid emerging from a nozzle tends to follow the nearby curved surface and attaches to it. As a result, the flow becomes asymmetric despite having a symmetric model. When the velocity is increased close to the one wall, the pressure decreases. The pressure difference keeps the flow asymmetry [114]. The former definition of the Coanda effect is correlated to Bernoulli's equation. The decrease in the pressure is the reason for causing bubbles in the electrolyte base on Bernoulli's equation. It is the principle of cavitation erosion. Consequently, the result of CFD simulation raises the idea of cavitation erosion in the electrolyte which is investigated in chapter 4.
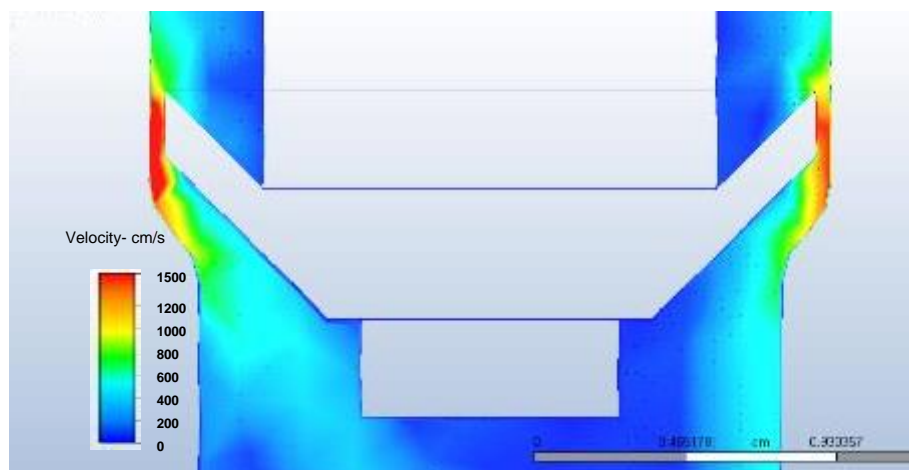
Figure 3-9: CFD simulation of PECM by Autodesk showing asymmetric velocity of the electrolyte as a result of the Coanda effect.

Fluid-solid simulation result done by Autodesk on the tool is illustrated in Figure 3-10. The stress on the surface is not symmetric as well because the CFD result used as the load in the fluid-solid simulation is not symmetric. The maximum stress imposed to the tool's surface is less than 1 MPa in Figure 3-10. Consequently, there is no effect or change on the tool because of imposed stress on the surface by the electrolyte.
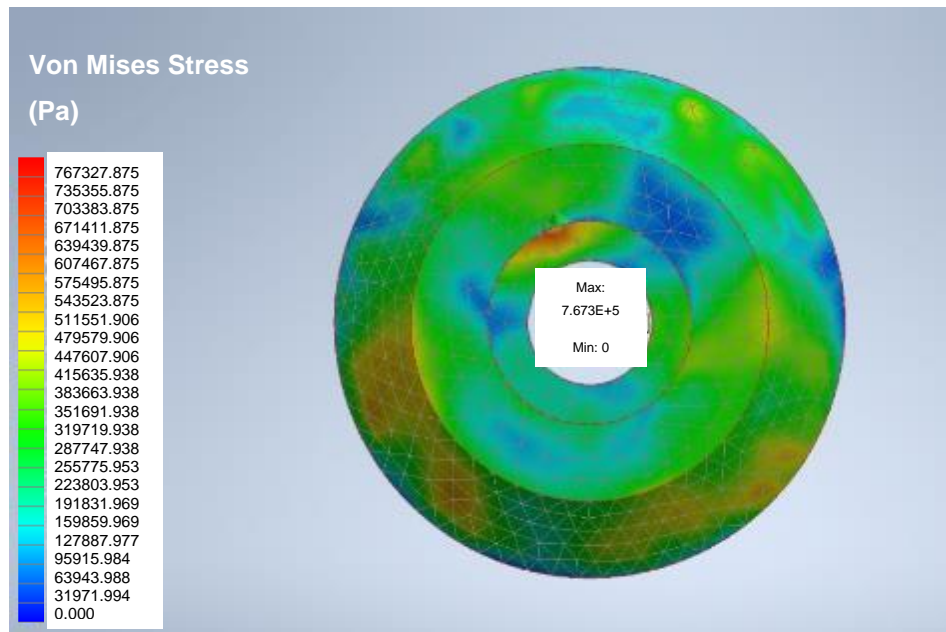
Figure 3-10: Fluid-solid simulation by Autodesk on the tool during PECM showing asymmetric imposed stress on the surface because of asymmetric electrolyte's flow.

Residual tensile stress

The tool's surface is investigated under the microscope to find the existence of the white layer before PECM. In Figure 3-11 (a), a layer of small grains with a thickness of 3.66 μm is formed, showing grain refinement and dynamic recrystallization. The grains' size on the surface varies from 0.19 μm to a coarser size of 0.76 μm. The formation of the refined grains is evidence of the white layer. However, Figure 3-11 (b) shows no evidence of white layer formation. It could be because of a very thin white layer that does not show in the FESEM image. As a result, XRD is used to directly find the residual stress type and amount on the tool's surface.
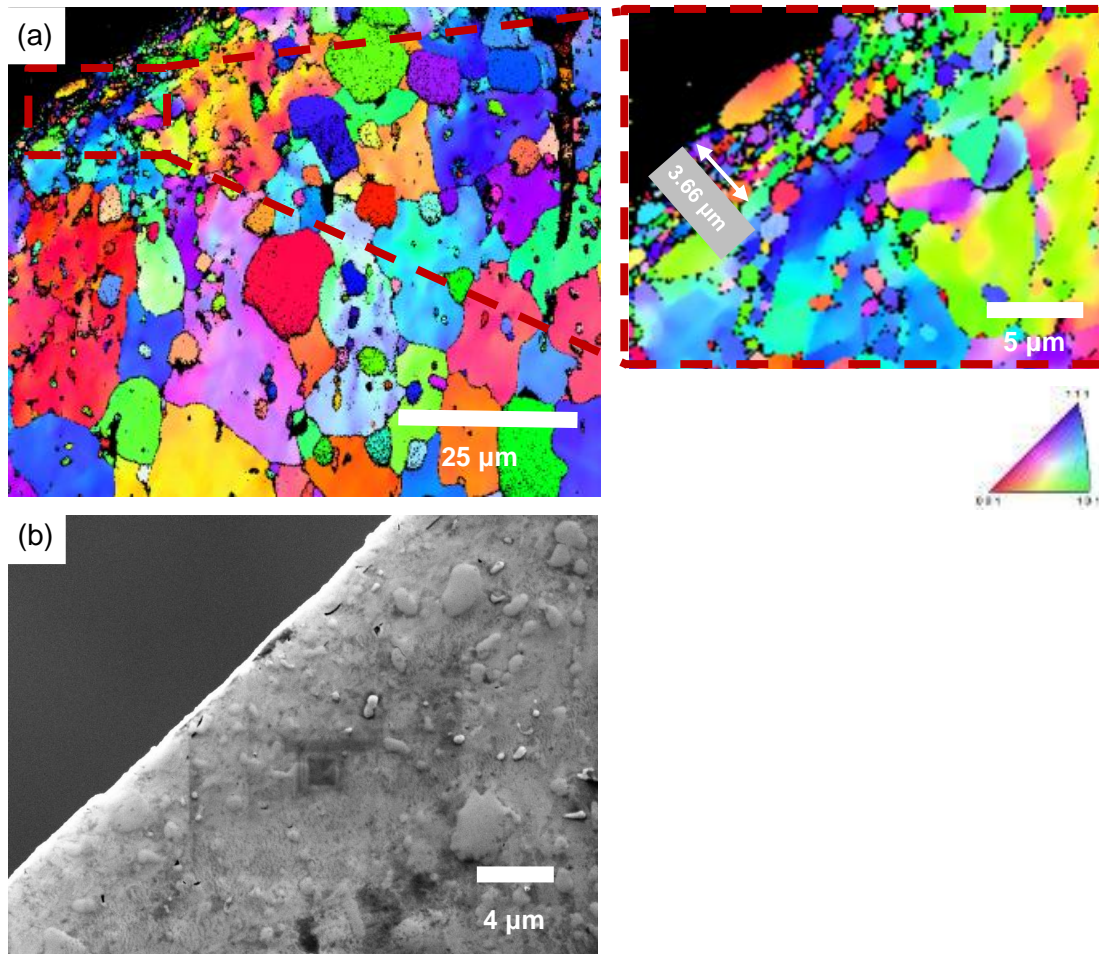
Figure 3-11: Before PECM (a) EBSD view of the tool near the surface (b) Microstructure of the tool near the surface. The dynamic recrystallization occurs on the surface after the turning process leading to the refinement of the grains to the depth of 3.66 µm.

XRD is done on the sample in different depths of 50 µm with steps of about 5 µm to use the plot for extrapolating and gaining residual stress on the surface, shown in Figure 3-12. However, the results in two directions (the same direction with turning and normal to the direction) show no tensile residual stress on the surface. The residual stress in all steps are compressive residual stresses. The residual stress on the surface in the directions of the parallel to the turning process is -292 MPa and the normal to the turning direction is -452 MPa. At the depths of 50 µm, the residual stress amount in the direction of parallel and normal are -142 MPa and -332 MPa, respectively. As the slopes of both plots are positive, extrapolation led to more compressive residual stress. It shows that thermal actions are not dominant during turning process and interaction between the surface layer and the bulk causes compressive stress.
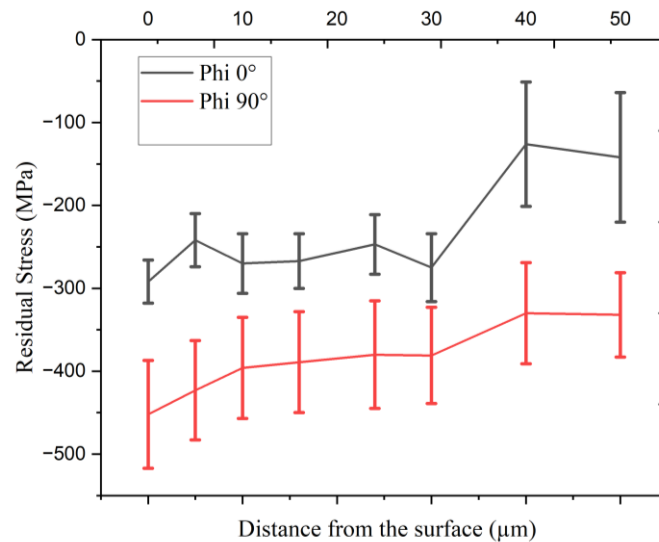
Figure 3-12: Compressive residual stress in the depth of tool 1.4112 before PECM in two directions of normal and parallel to the turning process till the depth of 50 μm measured in each step of about 5 μm.

3.4 Conclusion

Three prerequisites needed for hydrogen embrittlement are investigated:

1. The sample used is 1.4112, which is susceptible to hydrogen embrittlement because of its microstructure and having ferrite as the matrix.
2. TDS test shows that 6.8 ppm hydrogen diffuses into the sample.
3. The XRD result shows no tensile residual stress on the surface.

Consequently, hydrogen embrittlement is not the reason for damage to the tool, as the three prerequisites do not meet simultaneously.

4 Cavitation erosion

4.1 Literature review

Cavitation is defined as the growth and collapse of the vapor cavities or bubbles due to the local pressure fluctuation in a liquid [115]. Vapor cavities or bubbles are formed in liquid because of the supply of mechanical and thermal energy; either by subjecting it to tensile stress or by raising its temperature to boiling point [116]. If the pressure in liquid drops to the below the vapor pressure (for example because of sharp changes in the geometry of the flow), the tensile stress imposed on the liquid leads to the generation of cavities or bubbles. When the pressure in the liquid increases, the bubbles collapse, and a sudden flow of liquid is generated. Consequently, stress pulses are imposed on the surface of the solid [115]. The nucleation of the cavitation bubbles is easier when there are other phases in liquid like contamination or bubbles of undissolved gas. The cavitation erosion is defined based on Bernoulli's equation:

$$P + \frac{1}{2} \cdot \rho_l \cdot V^2 = \text{const.} \qquad \text{4-1}$$

In this equation P is local pressure, V is the velocity of the liquid and ρ is the density of the liquid. There is a balance between the kinetic energy and potential energy of the electrolyte. The velocity of the electrolyte changes the kinetic energy and the pressure of the electrolyte changes the potential energy but the sum of both energies in the electrolyte is constant. As a result, the local increase in the velocity (because of the changes in the liquid flow pattern) leads to a decrease in the local pressure [117]. When the cavitation bubbles collapse large stress pulses are generated due to the shock wave (Figure 4-1 (a)). Then a high-velocity microjet attacks the adjacent solid surface (Figure 4-1 (b)). The velocity of the micro jet can reach 100 m/s. The stress imposed on the surface can reach the GPa level. Rapid repetition of such a high scale of stresses imposed on the surface leads to localized fatigue and material removal [116].
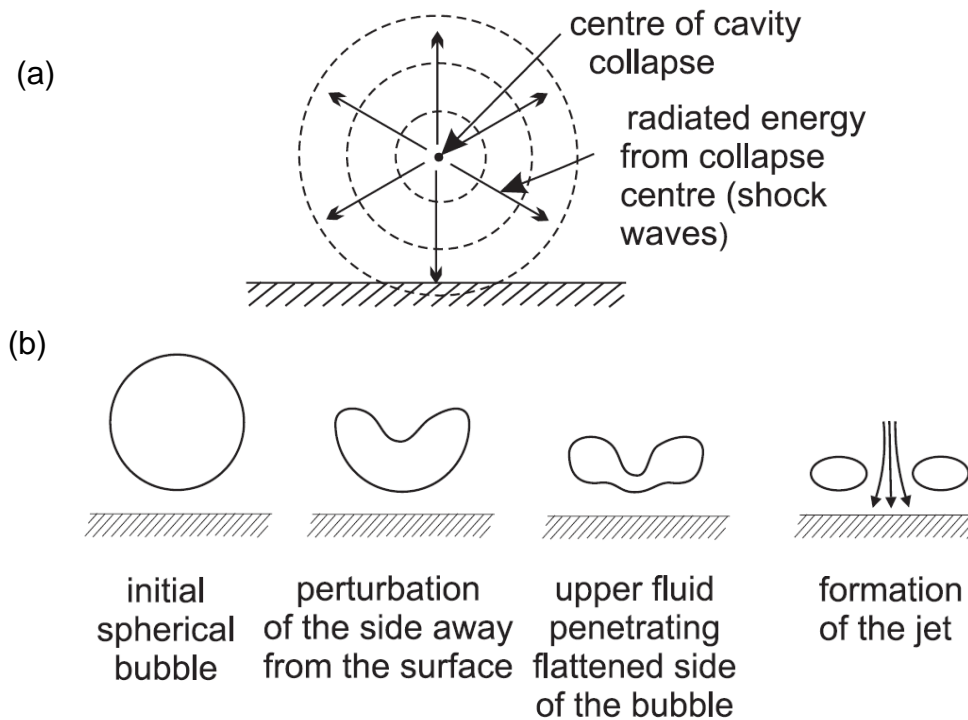
Figure 4-1: (a) the shock wave mechanism (b) the micro jet mechanism of cavitation erosion [116].

During PECM it is assumed that the oscillation of the tool may affect the pattern of the flow and pressure. In addition, the simulation results in chapter 3.3.3 show that the Coanda effect exists. The Coanda effect leads to a decrease in the local pressure in the electrolyte. Then, it is considered that cavitation erosion might affect the tool and form pits on it during PECM. As a result, the flow of electrolyte must be designed perfectly. In addition, the proper design of the tool can help in decreasing cavitation erosion, by having a uniform flow of electrolyte in all machining areas. The optimum flow of the electrolyte is desired because excessive flow can cause erosion of the tool [2].

To prevent cavitation erosion, outlet pressure can be increased, some additives can be added to the electrolyte, or the sudden change in the pattern of the flow should be controlled. The additives cause non-Newtonian behavior and less turbulent friction [3]. Depending on the design of the solid surface different conditions of electrolyte flow pattern and local pressure changes exist [5]. Figure 4-2 shows one condition that the Coanda effect occurs adjacent to a solid surface which is more similar to the piping condition used in this study. In the vortex area, the pressure is lower than in other areas.
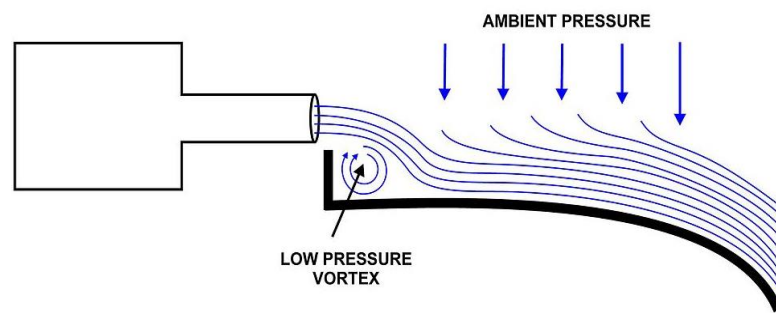
Figure 4-2 Coanda effect occurring adjacent to a solid surface showing formation of areas with lower pressure in the electrolyte [5].

Studies show that having vibration in the tool leads to cavitation on the anode which helps with material removal [118]. The vibration of the tool makes microbubbles in the electrolyte which collapse near the electrode again and increase the intensification of mass and electric charge transportation. Moreover, it is shown that vibration intensifies the electrochemical process by increasing the diffusion of metal ions [119]. The small IEG during ECM and PECM rise the probability that the cavitation may not only occur on the workpiece but on the tool as well.

4.2   Experimental

4.2.1   Cavitation erosion

The experiments are done on the PECM machine by excluding the oscillation of the tool to investigate the effect of oscillation. To exclude the oscillation of the tool, the mechanical frequency is excluded. The PECM setup and parts used are similar to chapter 2.2.

In addition, the machining is repeated for 10 cycles though in chapter 2.2 the PECM is done for 100 cycles. It is intended to ensure whether the changes and pits' formation on the tool occur in short-term machining as well. During this investigation, other parameters are constant as PECM with oscillation in Table 2-5. The working condition is shown in Table 4-1.

Table 4-1: Machining condition in $NaNO_3$ as electrolyte without oscillation of the tool.

Parameter	Value	Unit
Electrolyte	$NaNO_3$	
IEG	0.750	mm
Feed rate	0.950	mm/min
Machining depth	60	mm
Voltage	13	V
Electr. frequency	90	Hz
Phase	50	%
Electrolyte pressure	5	bar
pH	8±1	
Conductivity	80±5	mS/cm
Pulse duration	2	ms
Cycle	10	
Temperature	Ambient±5	℃

4.2.2 Measurements and technology

<u>Surface Analysis</u>

The samples are cleaned in an ultrasonic cleaning machine with alcohol. The surface of the tool is investigated with the help of FESEM (ZEISS SIGMA), SE, at the Institute of Material Science and Methods, Saarland University.

4.3 Results and discussion

Based on the CFD result in Figure 4-3 which is derived from the results shown in chapter 3.3.3 asymmetric flow of electrolyte exists. It is evidence of the Coanda effect. The Coanda effect leads to local pressure changes in the electrolyte. In the zones with lower pressure based on Bernoulli's equation, bubbles form, and cavitation erosion could occur. As the simulation is done in the stationary study, it is assumed that the tool oscillation increases the changes in the flow pattern and pressure (based on more material removal with tool vibration effect which affects the electrolyte flow [118]). As a result, the effect of tool oscillation is investigated.
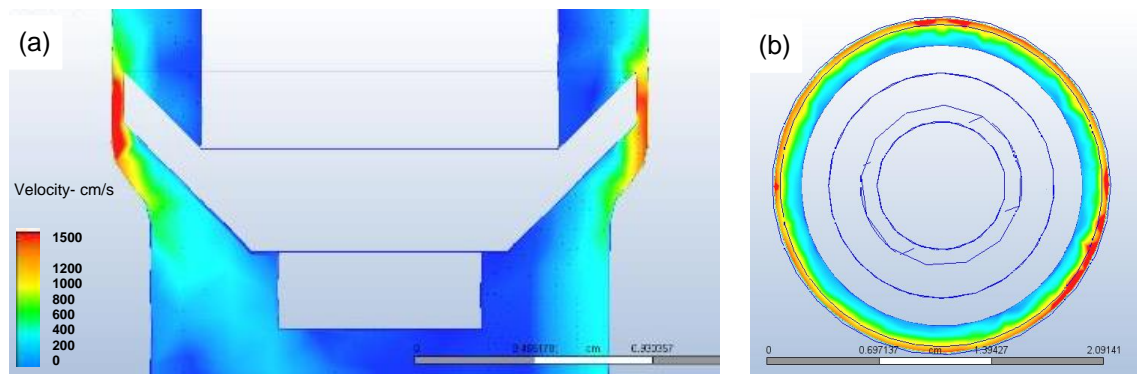
Figure 4-3 CFD simulation result in chapter 3.3.3 showing asymmetric electrolyte velocity (a) cross-section view (b) top view in the IEG. The asymmetric velocity of the electrolyte shows the Coanda effect.

Figure 4-4 compares the tool's surface before PECM, and after PECM with and without oscillation of the tool. Figure 4-4 (a) and (b) are derived from the results in chapter 2.3. No pit is observed on the tool's surface before PECM in Figure 4-4 (a). After PECM with and without oscillation of the tool in Figure 4-4 (b) and (c), the surfaces are changed and pits are formed. Figure 4-4 (d) shows the pits on the tool without oscillation of the tool in higher magnification. As a result oscillation of the tool causes no cavitation erosion and has no effect on the formation of the pits. The acquired results help with the design of laboratorial setup by excluding the oscillation and tool feed which is going to be explained in chapter 5.2.3.

Another parameter investigated is the time (cycles) of machining. Figure 4-4 (b) shows the tool's surface after 100 cycles and Figure 4-4 (c) is after 10 cycles PECM. The amount of pits and the damage is decreased by decreasing the machining time. It shows that the pits formation on the tool is a short-term effect and even in lower machining time it could occur.
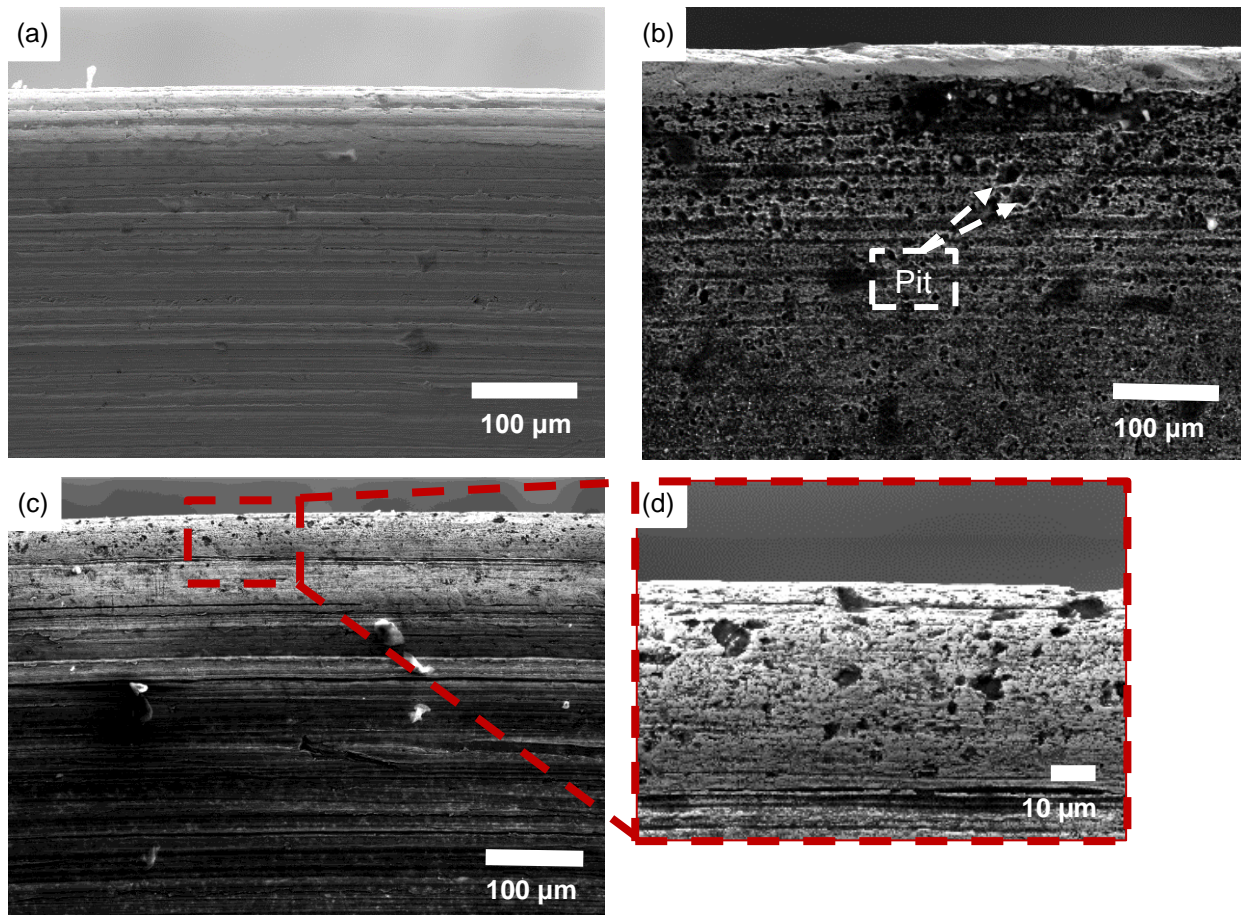
Figure 4-4: Surface of the tool 1.4112 (a) before PECM (b) after 100 cycles PECM with oscillation of the tool (c) after 10 cycles PECM without oscillation of the tool in lower magnification (d) after 10 cycles PECM without oscillation of the tool in higher magnification. By excluding the oscillation of the tool the pits still form during PECM. By decreasing the machining time the pits still form but their numbers are decreased.

4.4 Conclusion

The effect of oscillation of the tool and time are investigated:

1. Oscillation of the tool has no effect on the formation of the pits during PECM because of cavitation erosion. This result helps with excluding the tool feed and oscillation in designing the laboratorial setup in chapter 5.2.3.

2. Machining time affects the amount of pits formation. The pits formation is a short-term effect and occurs in lower machining time.

5 Cathodic corrosion

5.1 Literature review

Cathodic corrosion or cathodic activation is somehow an etching process. During cathodic corrosion, the cathode is corroded at potentials assumed to be cathodically protected.

Seebeck noticed the reaction between mercury cathodes and ammonium carbonate in 1808 [120], and in 1810, Sir Humphry Davy reported the corrosion of an arsenic cathode [121]. The corrosion of lead and arsenic cathodes was investigated by Reed in 1895 [122]. Haber and Bredig reported studies on the cathodic corrosion of lead and other electrodes in 1898 [123]. Further studies are published in 1902 and 1903 by Haber and Sack [124, 125] and 1970s [126], but most fundamental studies are done recently [127-129]. Based on these studies, it is assumed that cathodic corrosion occurs by forming an unknown metal containing an anion [130]. However, the nature of this anion needed for cathodic corrosion is unclear. Some approaches use cathodic corrosion to alter the metallic surface and produce shape-controlled nanoparticles that exhibit favorable catalytic properties [131].

Some electrolyte cations enable cathodic corrosion, like alkali metal cations [130]. There are different mechanisms proposed for cathodic corrosion. Regarding the applied current densities and other experimental conditions like electrolyte composition, one mechanism or more than one mechanism is activated. Some of the mechanisms are alloying with alkali metals [123-125], formation of metal hydrides [132-134], bimetallic corrosion pathway [135, 136], cathodic etching [130, 137], contact glow discharge [138], and anodic degradation of cathode [139]. The concentration of the electrolyte is an important factor affecting cathodic corrosion. Thermodynamically, the cathodic corrosion increases by increasing the concentration of alkali ions in the electrolyte. However, Salzberg's study shows the opposite of the expected trend [71]. Some important mechanisms are explained in the following chapters.

5.1.1 Alloying with alkali metals mechanism

The alkali cation A^+ in the electrolyte near the cathode is shown in Figure 5-1 (a). The cation forms a bimetallic alloy with the cathode (Figure 5-1 (b)). Then the alloy is

oxidized by water, and the alkali cations leach out of the cathode, making sponges or pitted structures on the cathode (Figure 5-1 (c)). This mechanism is proposed for metals and alloys like Pb, Sn, Bi, Sb, Hg, As, Tl, and Rose alloy electrodes [71, 123].
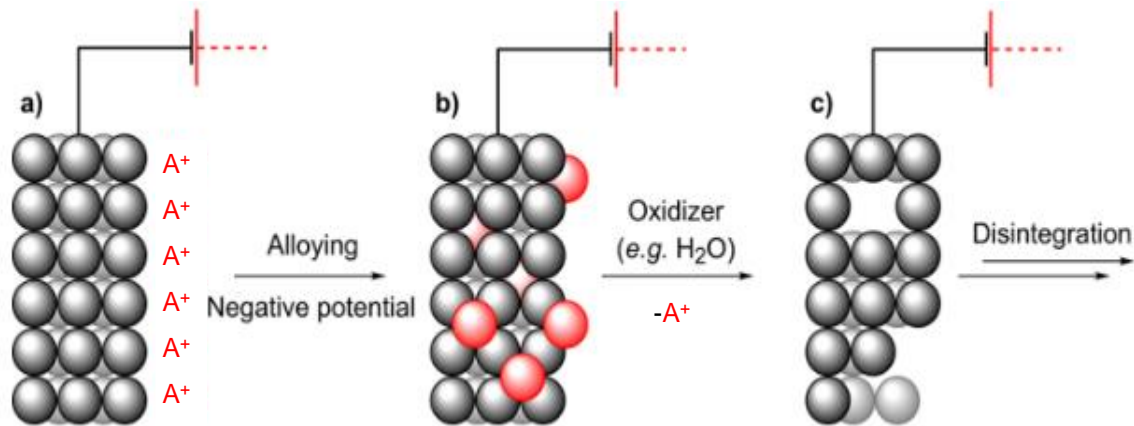
Figure 5-1: Schematic of alloying with alkali metals mechanism for cathodic corrosion. The alkali cations make an alloy with the cathode. The alloy reacts with the oxidizer (water) and the alkali cations leach out of the cathode [71].

5.1.2 Formation of metal hydrides mechanism

Some metals like Cu, Pb, Sn, Bi, and Sb can form (meta) stable hydrides, which are assumed as intermediates in their cathodic corrosion. At the surface of the cathode, which is in contact with an aqueous solution, the Me-H bond forms (Me is the element in the cathode) (Figure 5-2) [140, 141]. The metal hydride then releases from the cathode and either evaporates from the reaction mixture or reacts with an oxidizer like water to produce hydrogen gas and metallic particles. These particles can stay in the electrolyte or deposit on the surface of the cathode [71, 141].
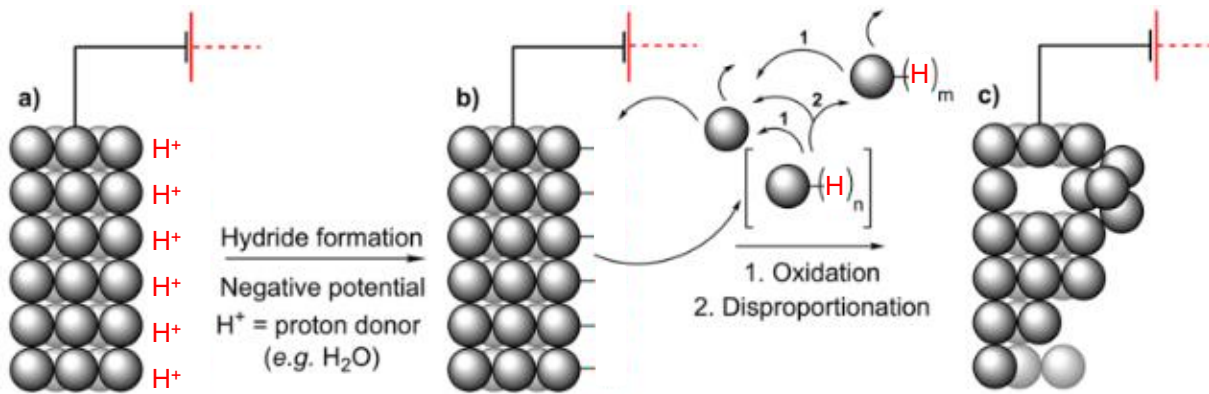
Figure 5-2: Schematic of the formation of metal hydrides mechanism for cathodic corrosion. At the cathode the Me-H bond forms. It releases from the cathode and reacts with the oxidizer (water) to form metal atoms and hydrogen gas [71].

5.1.3 Cathodic etching mechanism

Cathodic etching occurs for Pt, Rh, Ir, Pd, Au, Ag, Cu, Re, Fe, Ni, Nb, Ti, V, W, Si, Nb, Ru, Al, Pb, Sn, Sb, Bi, Hg, Ga, and In [142]. At the metallic cathode, metal anions or anionic clusters are formed and stabilized by nonreducible electrolyte cations. The metal anions or clusters are detached from the cathode surface. It is assumed to be because of having the dynamic water-free layer with high pH at the solution and cathode interface. Then free metal anions face the oxidants like water and deoxidize to metal atoms and agglomerate and deposit on the electrode (Figure 5-3) [71]. It is reported that adsorbed hydrogen, which is produced at the cathode, plays a crucial role in cathodic corrosion, which makes ternary metal hydrides ($A_xMe_yH_z$; A = alkali or alkaline earth metal, Me = transition metal, H = hydride) as elusive intermediates in cathodic etching [142].
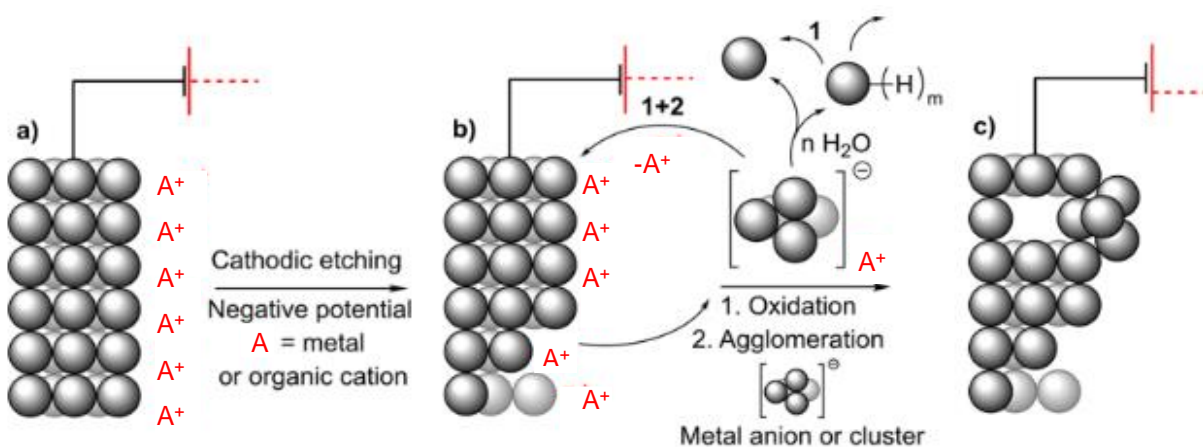
Figure 5-3: Schematic of the formation of cathodic etching mechanism for cathodic corrosion. At the cathode, the metal anions or anionic clusters are formed. They detach from the surface and react with the oxidant (water) to form metal atoms [71].

5.1.4 Inhibiting cathodic corrosion

Two methods are proposed to help inhibit cathodic corrosion based on reductive organic electrochemistry: cationic additives and alloying (Figure 5-4). These methods modify the electrical double layer (EDL) or the physicochemical properties of the cathodes. In addition, the advantageous properties of the cathodes, such as the high overpotential for hydrogen, are increased. Moreover, using both methods improve extractability, machinability, softness, etc. Consequently, corrosion resistance and practical aspects are improved [71].
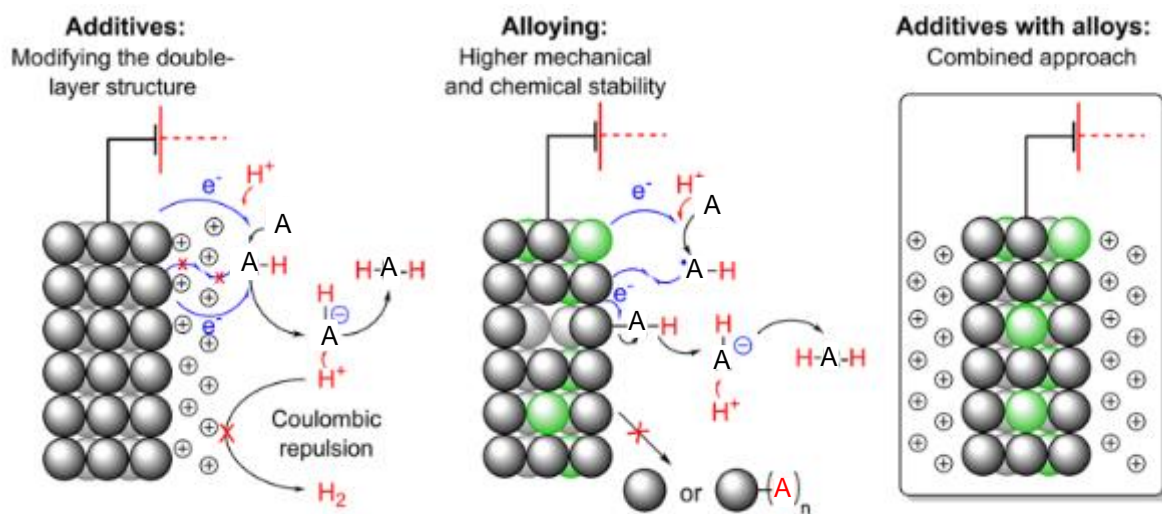
Figure 5-4: Methods of inhibiting cathodic corrosion. Cathodic corrosion is inhibited by adding cationic additives to the electrolyte or alloying the cathode [71].

An electrical double layer forms by polarizing the electrode in an electrochemical cell. Different inorganic or organic cationic additives are added to modify this layer and improve cathodic corrosion which are shown in Figure 5-5. In addition, by introducing a small amount of the active metal into a base metal, cathodic corrosion of base metal is inhibited by alloying method [71].
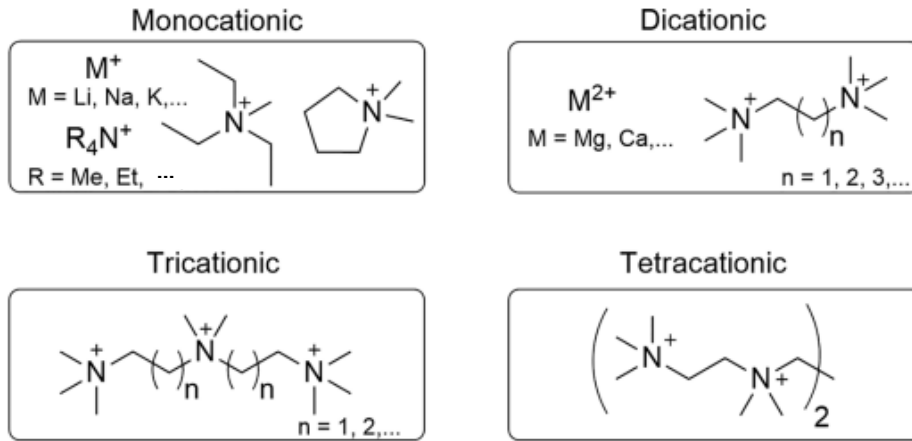
Figure 5-5: Different types of cationic additives to inhibit cathodic corrosion [71].

Hersbach and Koper proposed the adoption of an updated Pourbiax diagram for Pt which gives a better understanding of cathodic corrosion [71]. The Pourbaix diagram illustrates the potential condition vs. pH and describes if the metal is corroded, immune, or passivated. The corrosion area in all Pourbaix diagrams indicates anodic corrosion. However, in Figure 5-6, there are two different areas showing corrosion of Pt: anodic corrosion and cathodic corrosion. There is cathodic corrosion in pH higher than about 14 and negative potential. It is not still clear if cathodic corrosion in lower pH occurs. Consequently, considering this diagram, decreasing the surface pH might help prevent cathodic corrosion.
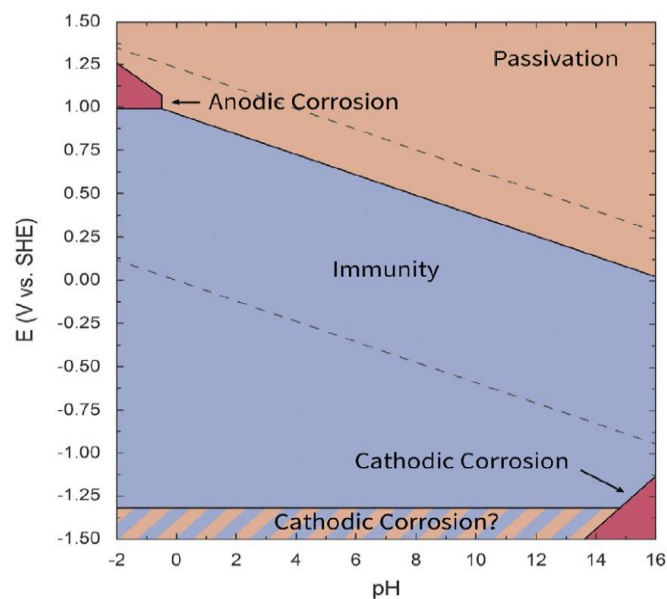
Figure 5-6: Updated Pourbaix diagram for Pt showing cathodic corrosion zone separated from anodic corrosion zone in high pH and negative potential [71, 143].

5.2   Experimental

In this study, small steps are designed to investigate cathodic corrosion, as there is no specific way to investigate it in the literature in this context. As the first step, cyclic polarization (CP) is investigated to determine the corrosion type of 1.4112. It is assumed that the corrosion type may help better understand the mechanism of cathodic corrosion. Then, a setup is designed with two different materials as the cathodes (noble and active metals) to investigate the possibility of galvanic corrosion on the cathode with working condition close to Table 2-5. The last step is designing a laboratorial setup to investigate the effect of electrolyte concentration in a simplified ECM setup compared to the industrial PECM machine. The basic aspects of the experiments with laboratorial ECM setup and industrial PECM machine are kept as equal as possible.

5.2.1   Cyclic polarization of 1.4112

The corrosion test is done with three electrodes for 4670 cycles. The reference electrode used is a saturated calomel electrode (SCE—Hg, Hg_2Cl_2, KCl_{sat}), with a platinum sheet as a counter electrode in an aqueous $NaNO_3$ electrolyte with a conductivity of 80 mS/cm. The working electrode is 1.4112, which is used as the tool in the PECM process. The working electrode has a diameter of 20 mm and a thickness of 2 mm. The surface of the working electrode is polished to make later microstructural imaging possible.

5.2.2   Galvanic corrosion test on the cathode

A special setup is designed to investigate the probability of galvanic corrosion on the cathode. Two different materials (one noble and one active) with different standard potentials are used to stimulate the cathode's corrosion. The noble material is copper, which has the standard potential of 0.34 E_0/V for:

$$Cu^{2+} + 2e^- \rightleftharpoons Cu_{(s)} \qquad\qquad 5\text{-}1$$

The active material is pure ferrite with the standard potential of -0.44 E_0/V for:

$$Fe^{2+} + 2e^- \rightleftharpoons Fe_{(s)} \qquad\qquad 5\text{-}2$$

Based on standard potential, an element with more positive standard potential is protected and a more negative one is dissolved. Consequently, ferrite is expected to

play the anode role, and copper plays the cathode role in galvanic corrosion. The ferrite has a size of 10 mm × 2 mm diameter and thickness, respectively. Copper is a square sheet of 20 mm × 20 mm with a hole in the middle with a diameter of 7 mm. Although other elements like Pt could play a better role as the noble cathode in this set, copper is more affordable.

The cathodes are not placed in the electrolyte entirely and are placed under the electrolyte chamber. Positioning the cathodes at the bottom of the electrolyte chamber reduces the edge effect and concentration of electric charge at the edge [144]. The setup is illustrated in Figure 5-7. The flushing chamber's drawing file is available in APPENDIX.
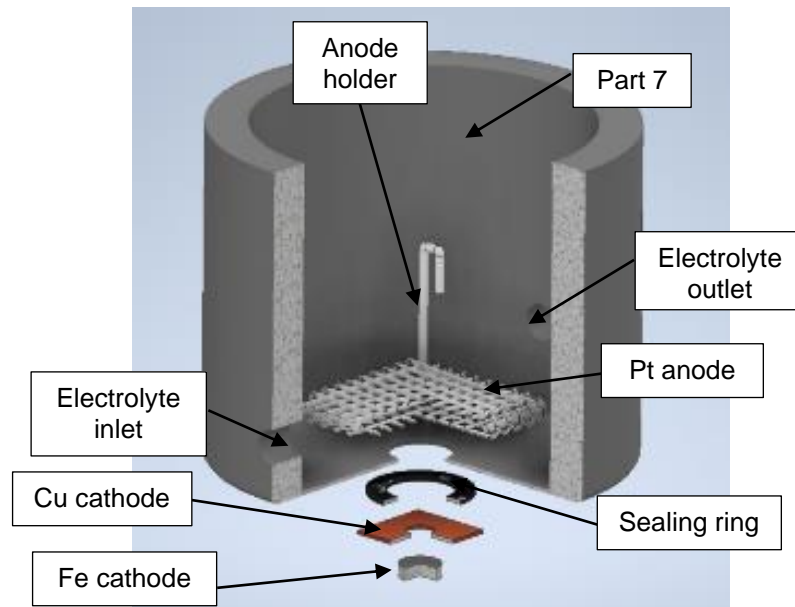
Figure 5-7: Schematic of the cathodic corrosion test setup, Part 7. Electrolyte chamber.

The real image of the setup is shown in Figure 5-8 (a). The inlet of the electrolyte is at a lower height than the outlet, letting fresh electrolyte enters the setup between the anode and cathode. On the way of pumping the electrolyte into the chamber, the electrolyte is cooled down with the help of a water-cooling circulator and a Graham condenser. The gap distance between the anode and cathode is manually set by placing the anode on the bottom of the chamber. Because of the design of the setup, the smallest possible gap is about 1 mm (the thickness of the bottom of the chamber). A noble anode (Pt) is chosen to have less anode dissolution in the electrochemical cell. The Pt wire with the 1mm diameter is formed to make a grid, as shown in Figure 5-8 (b). The applied voltage is 13 V with a VOLTCRAFT EP-925

Bench PSU power supply. The process runs for 10 hours as there is a probability of Pt deposition on the cathode during a longer time of the electrochemical process.
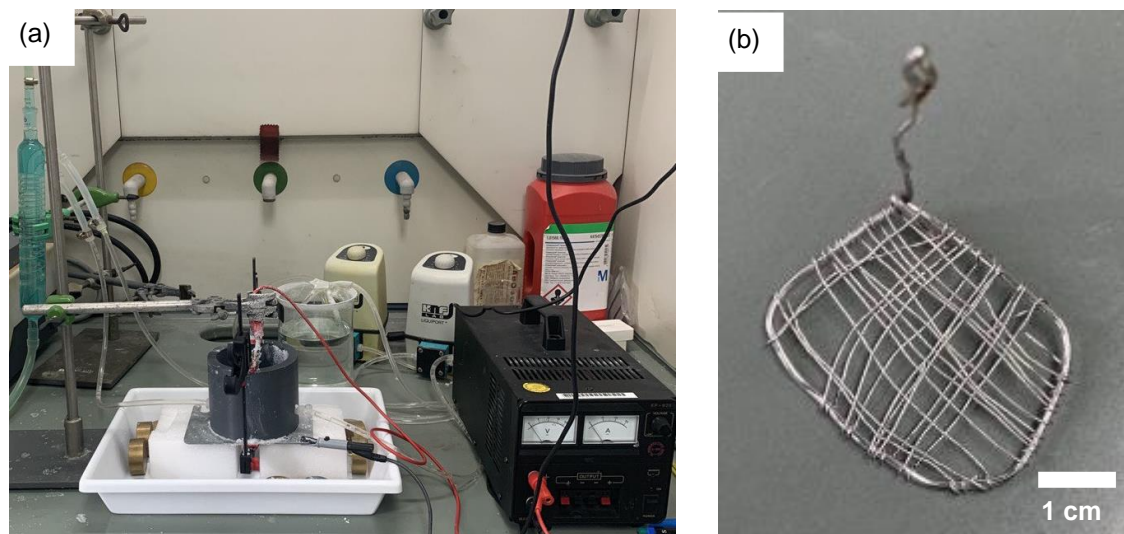
Figure 5-8: (a) Cathode's corrosion test setup by two different materials as the cathode (b) Pt anode shape used in the cathodic corrosion test.

5.2.3 Laboratorial setup

To simplify the ECM experiment, a small laboratorial setup based on the working condition in Table 2-5 with the PECM machine is designed. Some changes are necessary to transfer the working condition to the laboratorial scale. Considering the result of the machining process without oscillation on the PECM machine in chapter 4.3, the oscillation and feed of the tool are excluded. As a result, the tool is placed in the middle length of the workpiece which is shown in Figure 5-9. This way, the machining condition such as having a side IEG and electrolyte velocity is more similar to the experiment done with the PECM machine.
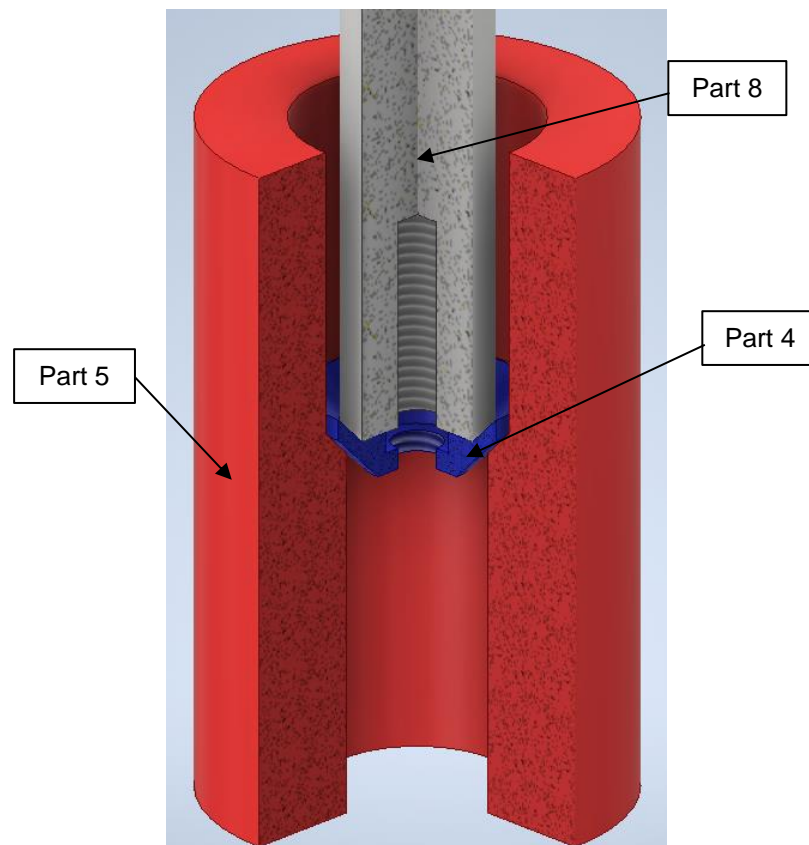
Figure 5-9: Position of the tool in the middle of the workpiece for doing ECM in laboratorial setup,
Part 4. Tool, Part 5. Workpiece, and Part 8. Tool holder to keep the tool in the center and make the
feed movement of the tool possible.

The CAD model of the upper parts of the setup is illustrated in Figure 5-10. An insulated PVC part is designed to mount the micrometer on it, which is shown transparent in Figure 5-10. The micrometer is necessary to adjust the IEG. There are two symmetric openings shown by red lines in Figure 5-10, which make assembling the coupler on the micrometer and tool holder possible. An insulated PVC coupler is made to be able to connect the micrometer and tool holder. Consequently, the movement of the tool holder and precise adjustment of IEG are possible. In addition, the connection of the cathode to the power supply is possible by using a screw through the coupler to the tool holder. An insulated PVC ring is designed to keep the tool holder and the tool in the center of the setup. The green color of the tool holder shows the coating on it, which is SLOTOWAX resin purchased by Schötter Galvanotechnik. The coating is applied by a brush in two layers.
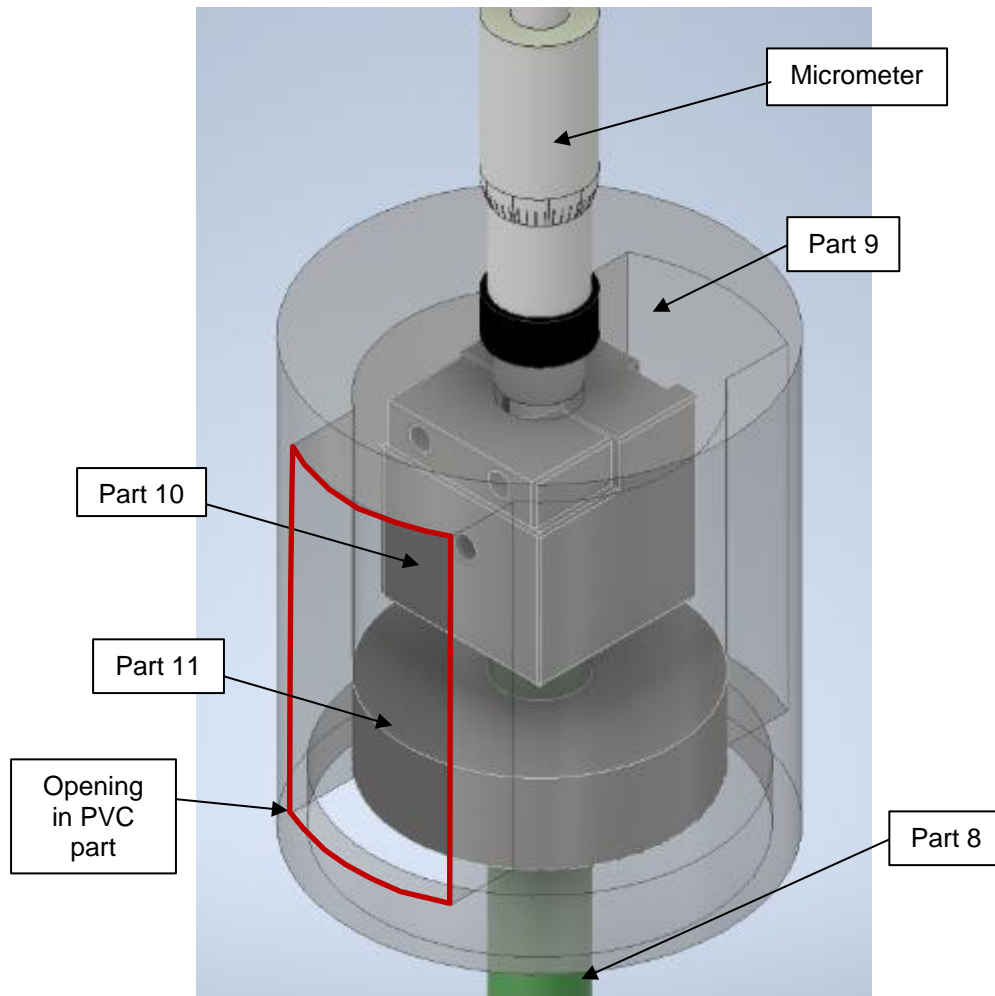
Figure 5-10: CAD model of the upper parts of setup used in laboratorial ECM experiment, Part 8. Tool holder to keep the tool in the center and make the feed movement of the tool possible, Part 9. PVC part to mount the micrometer on it, Part 10. The coupler of the micrometer and tool holder, and Part 11. Centering ring to keep the tool holder and tool in the center.

The CAD model of the inferior parts of the setup is illustrated in Figure 5-11. The PVC part used for mounting the micrometer is placed on a part named "belt." The belt is not only a base for the PVC part to be placed on, but also is a part to keep the anode and the flushing chamber fixed and stable during flowing pressurized electrolyte. The part is made of stainless steel to have good strength and, at the same time, corrosion resistance. It is fixed around the anode by two symmetric screws. The flushing chamber is the same as the one used in the PECM experiment in the PEMCenter machine explained in chapter 2.2.7. From two symmetric inlets, the electrolyte enters the flushing chamber. The interface of the tool holder-flushing chamber and anode-flushing chamber are sealed with sealing rings.

The tool, the tool holder, and the screw for connecting the tool to the tool holder are all green, which shows they are coated by SLOTOWAX resin. Only a small area of

the tool is not coated, which will be discussed in Figure 5-15. The screw is designed long enough to get through an insulated PVC centering cylinder. The centering cylinder keeps the tool in the center of the setup to avoid any lateral movement of the tool. The lateral movement of the tool might cause a short circuit. The stainless-steel fixture keeps the anode stable in the center with the help of a side screw during ECM. The anode is connected to the power supply with the help of a screw getting through the fixture. There are four rectangular holes as the outlet of electrolyte designed in the fixture. The electrolyte flows in from the flushing chamber, gets through the IEG and the workpiece, and flows out from the fixture.
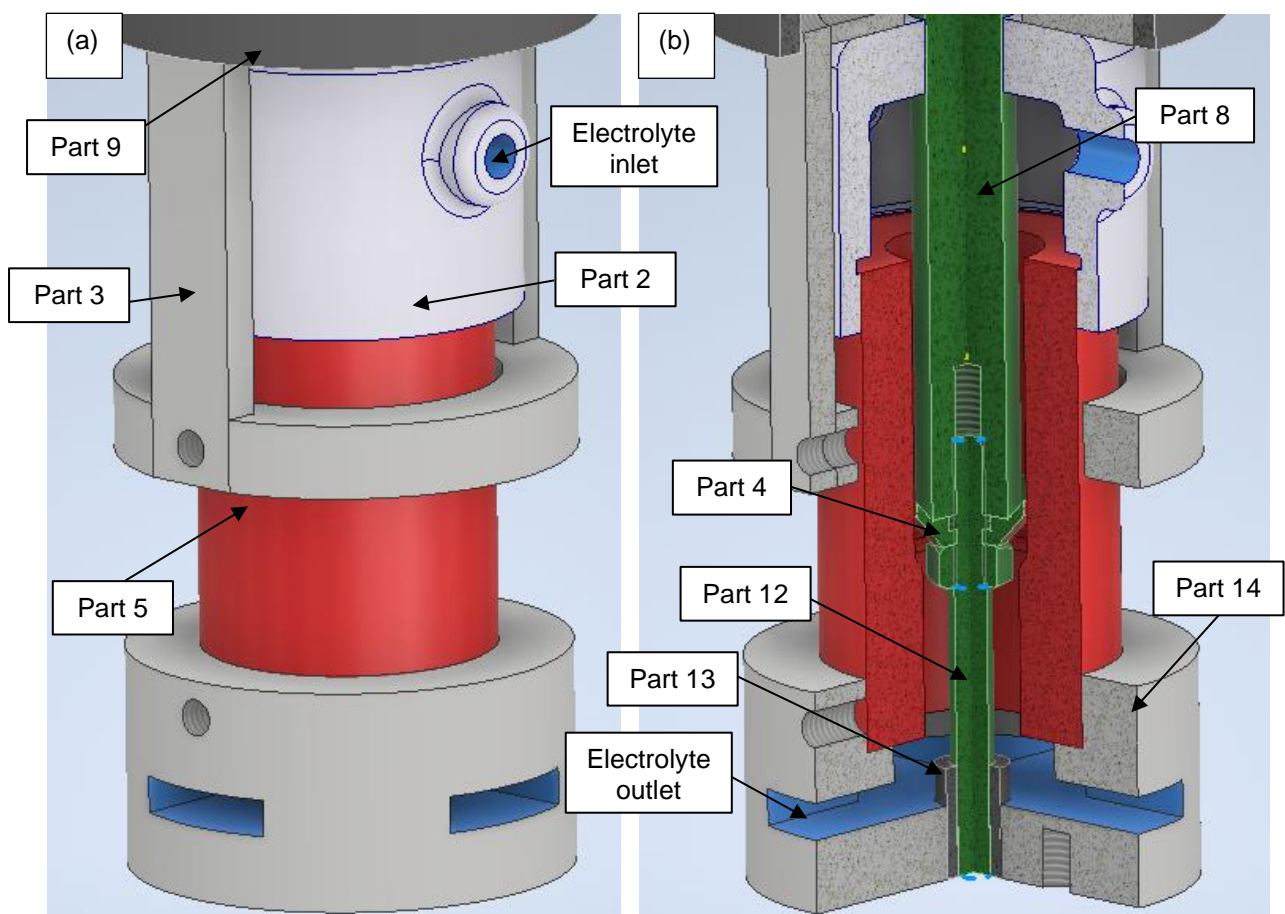
Figure 5-11: CAD model of the inferior parts of setup used in laboratorial ECM experiment, Part 2. Flushing chamber, Part 3. Belt to keep the flushing chamber and other parts constant against the pressure of flowing electrolyte, Part 4. Tool, Part 5. Workpiece, Part 8. Tool holder to keep the tool in the center and make the feed movement of the tool possible, Part 9. PVC part to mount the micrometer on it, Part 12. Centering screw, Part 13. Centering cylinder to keep the tool in the center, and Part 14. Fixture (a) full view (b) three-quarter view.

The complete setup is shown in Figure 5-12. The drawing files of all the parts designed for this study are available in APPENDIX. The machining zone is similar to what is used in PECM, shown in Figure 2-23. This area is marked in Figure 5-12 (a).

The real shape of the laboratorial setup for the ECM experiment is shown in Figure 5-13.
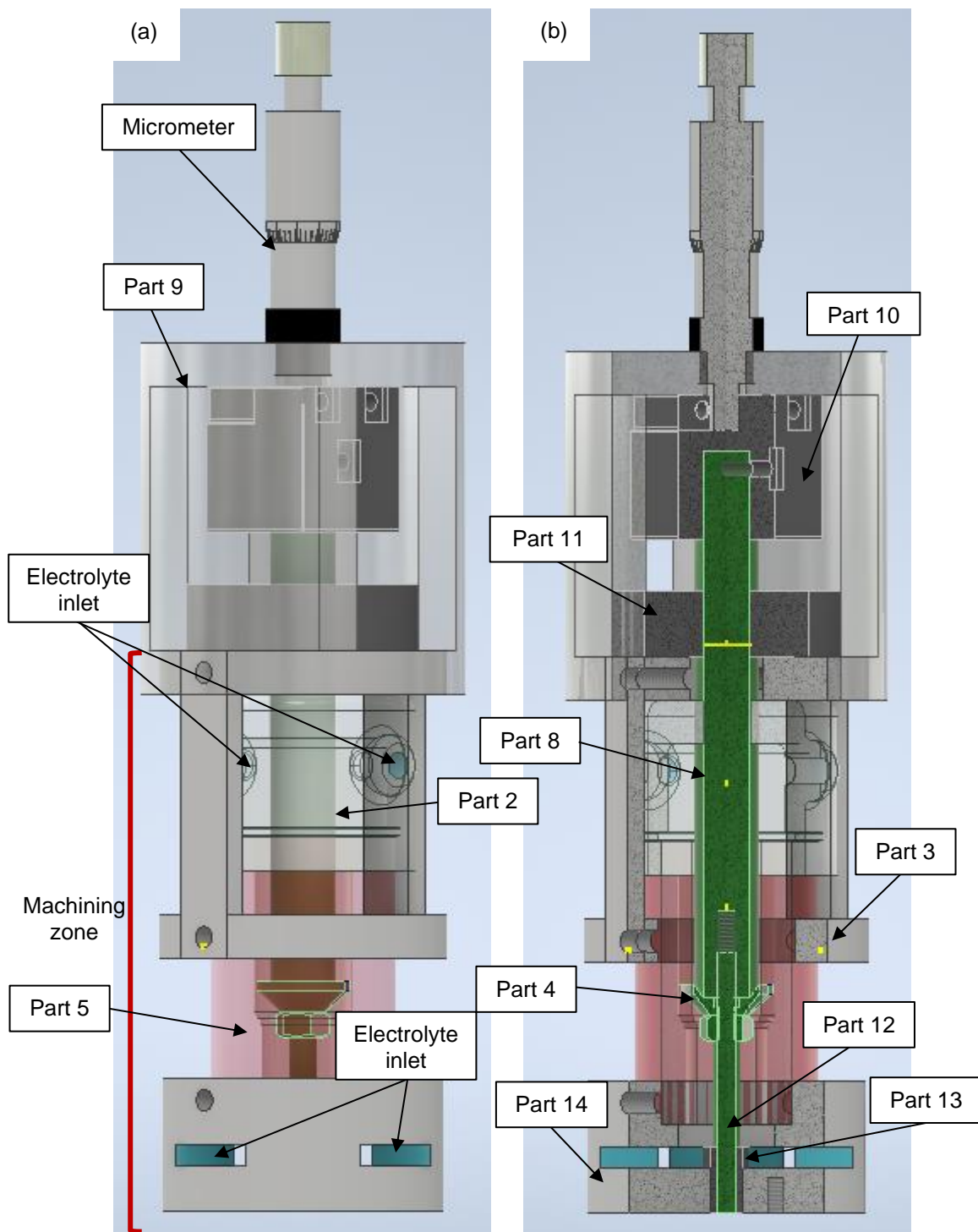
Figure 5-12: Setup used for laboratorial ECM, Part 2. Flushing chamber, Part 3. Belt, Part 4. Tool, Part 5. Workpiece, Part 8. Tool holder, Part 9. PVC part, Part 10. Coupler, Part 11. Centering ring Part 12. Centering screw, Part 13. Centering, and Part 14. Fixture (a) full view (b) three-quarter view.

Figure 5-13: Setup used for laboratorial ECM.

The power supply consists of a BioLogic potentiostat and a booster, as shown in Figure 5-14. These are controlled by a laptop and the associated software "EC-Labs." The maximum DC voltage and current applied by the power supply are ±10 V and 10 A. The power supply works as both the voltage source and as the measuring source in the way that by applying suitable voltage, the current flowing through the setup is measured and saved as a file. According to the manufacturer, the accuracy of the measurement electronics is up to 5 μV and 780 pA, respectively. The electrical setup of the electrochemical cell corresponds to a so-called 2-electrode setup. As a result, the cathode is simultaneously used as the reference electrode to measure the cell voltage. Figure 5-14 shows the power supply and its adjustment with the electrochemical setup during this experiment. Reference electrode 1 and the working electrode (WE) are served as the anode. Reference electrode 2, reference electrode 3, and counter electrode (CE) are served as the cathode. The blue arrows show the cathode, and the red arrows indicate the anode.
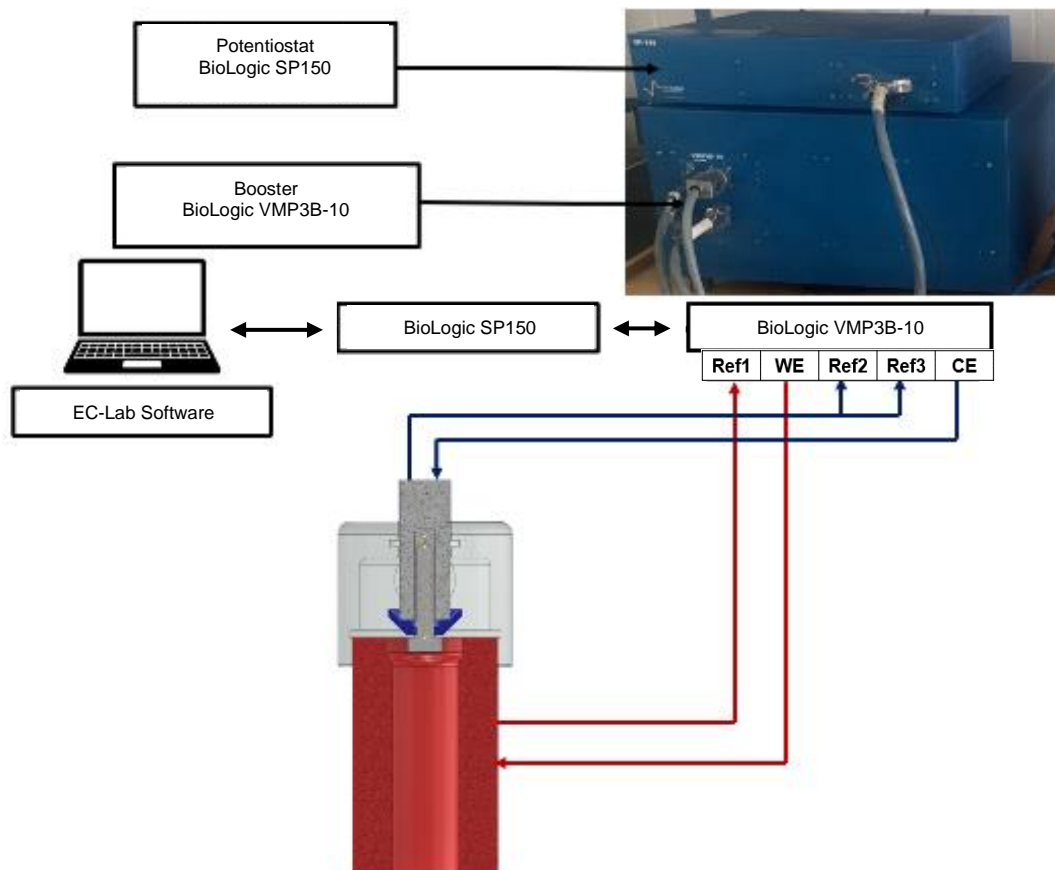
Figure 5-14: Power supply and electrochemical setup in correlation with each other. The red color shape and arrows are the anode, and the blue color shape and arrows are the cathode.

To correlate the result in this setup with the PECM experiment in chapter 2.2.7, the current density must be kept constant. To keep the current density constant in the working range by the power supply, the surface area of the tool is decreased.

The minimum mean value of current density during PECM in Figure 2-32 is 1.212 A/mm^2 and the maximum is 1.269 A/mm^2. The average of these two values is used for calculations here which is about 1.24 A/mm^2. By considering the maximum current by the power supply (10 A), and constant current density between PECM and ECM by laboratorial setup, the area of the workpiece considering Equation 2-17 is calculated:

$$1.24 \ [A/mm^2] = \frac{10 \ [A]}{A}$$

$$A = 8.06 \ [mm^2]$$

The tool's total area measured in chapter 2.3.2 is divided into 8.06 mm^2. Then 360 deg is divided into the result of that. The angle needed for ECM in laboratorial setup is calculated as 11.86 deg. This area of the tool is not coated, and the rest is

coated by SLOTOWAX resin (Figure 5-15). The coating is applied with the help of a brush and for two-layer to ensure the surface is completely covered.
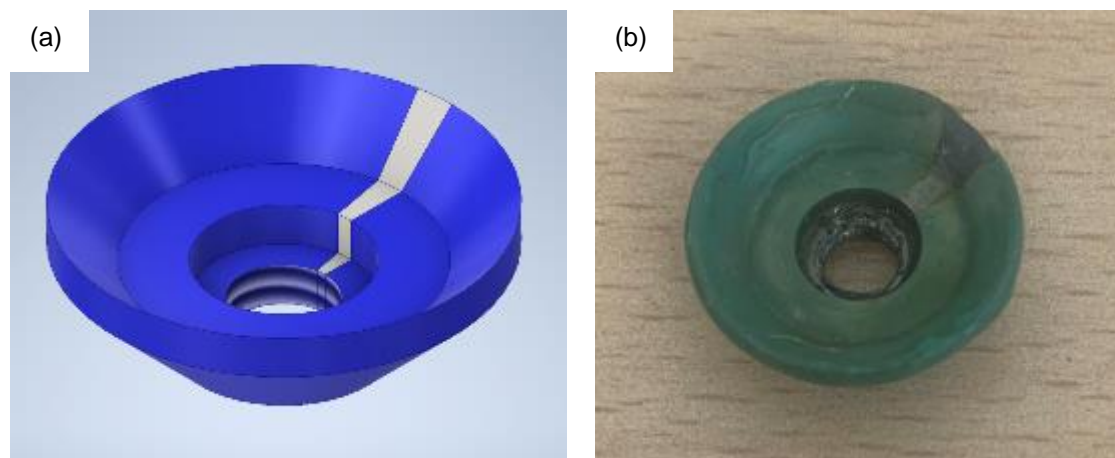
Figure 5-15: (a) The CAD image of the tool with coated area in blue (b) The real image of the tool coated by SLOTOWAX resin based on the CAD image.

The electrolyte flow is supported with the pump ISMATEC MCP-Z Process from the electrolyte supply tank to setup. An overrun system is used from the setup to the electrolyte supply tank. The volume of the electrolyte supply tank is 30 l.

5.2.4 Preliminary experiments

To determine the proper machining time, an investigation with different machining times is done to observe the removal behavior. The initial IEG is 0.750 mm which is adjusted with the help of the micrometer. The current density decreases over time due to no feeding in the tool. There is no severe decrease in current density during 15 min machining. As result, 15 min is chosen as the machining time in each cycle.

An investigation is done with 6 V, 8 V, and 10 V in an aqueous solution of $NaNO_3$ electrolyte with a conductivity of 80 mS/cm to prove the reasonable function of the setup. It is expected to see an increase in the current by increasing the voltage based on Ohm's law.

Further experiments are done with the conductivity of 50 mS/cm and 110 mS/cm to find the effect of conductivity and concentration on the pit's formation on the tool's surface as a cathodic corrosion parameter. With the help of Figure 2-20, the conductivity is correlated to the concentration of the electrolyte, which by increasing conductivity, concentration increases.

5.2.5 Measurements and technology

Surface Analysis

The samples are cleaned in an ultrasonic cleaning machine with alcohol. The surface of the samples and the changes are investigated with the help of FESEM (ZEISS SIGMA), SE, and EDS detector by Oxford Instruments X-Max at the Institute of Material Science and Methods, Saarland University.

Scanning kelvin probe force microscopy (SKPFM)

SKPFM combines atomic force microscopy (AFM) and kelvin probe methods. It can plot the potential map of the surface to measure the electrochemical potential and study the corrosion mechanisms. As a result, the anodic and cathodic behaviors of particles and matrix in the sample are measured [145]. SKPFM is usually done in the air, but electrochemical information is acquirable by doing it in the electrolyte. It measures the contact potential difference (CPD) between the sample and the tip (biased) as:

$$V_{CPD} = \frac{\phi_T - \phi_S}{e} \qquad \text{5-3}$$

Where ϕ_S is the work function of the sample, ϕ_T is the work function of the tip, and e is the electronic charge.

High work function indicates a high electrochemical nobility. The decreased work function shows an increased tendency for electron transfer and undergoing electrochemical reactions [146]. As a result, with the help of SKPFM, the difference volta potential is calculated, and based on it, the work functions of different phases are defined. With the help of the work function, the corrosion behavior is described.

The SKPFM done in this study is with Dimension FastScan at Bruker, Karlsruhe, Germany. The obtained result is evaluated by Nano scope analysis software developed by Bruker. A SCM-PIT probe with a Pt coating as the tip are used. The resulting images are modified by Flatten filter.

5.3 Results and discussion

5.3.1 Cyclic polarization of 1.4112

The CP output graph is shown in Figure 5-16. The First peak shows the oxidation peak which $E_{corr.}$ is -0.894 V and the second peak shows anodic to cathodic transition [147].
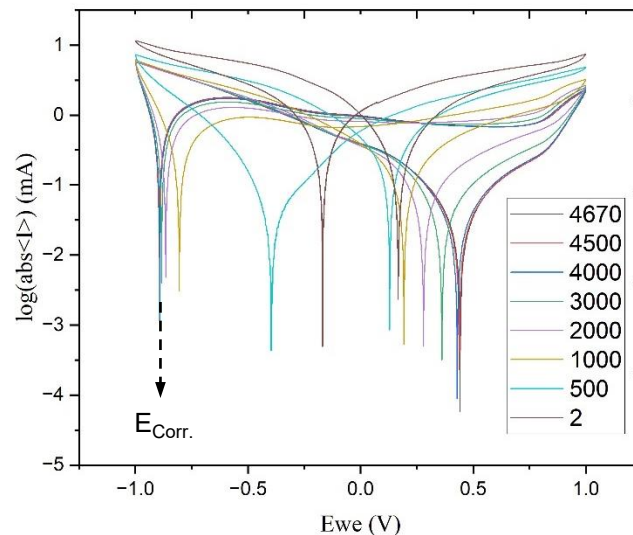
Figure 5-16: Cyclic polarization of tool after 4670 cycles. The corrosion potential is -0.894 V.

Figure 5-17 compares the microstructure and EDS-Map of the 1.4112 material before and after 4670 cycles of CP. Comparing Figure 5-17 (a) to (b) indicates that pits are formed on the surface. The size of the pits ranges about 3.4-0.3 µm. Comparison between Figure 5-17 (c) to (d) and Figure 5-17 (e) to (f) shows that by the formation of the pits, the distribution of elements and phases becomes different. It is related to the disappearance of the Cr carbides (any spot in the Cr EDS-Map shows the Cr carbides). After CP, Cr carbides disappear and ferrite remains. It is the evidence of galvanic corrosion; ferrite is the anode that is corroded, and carbides are cathodes that are protected. Ferrite is an active metal based on standard potential. The corrosion is initiated in ferrite around the carbides, and in the longer corrosion process, the whole ferrite around a carbide is corroded, and the carbide falls off the surface [148].
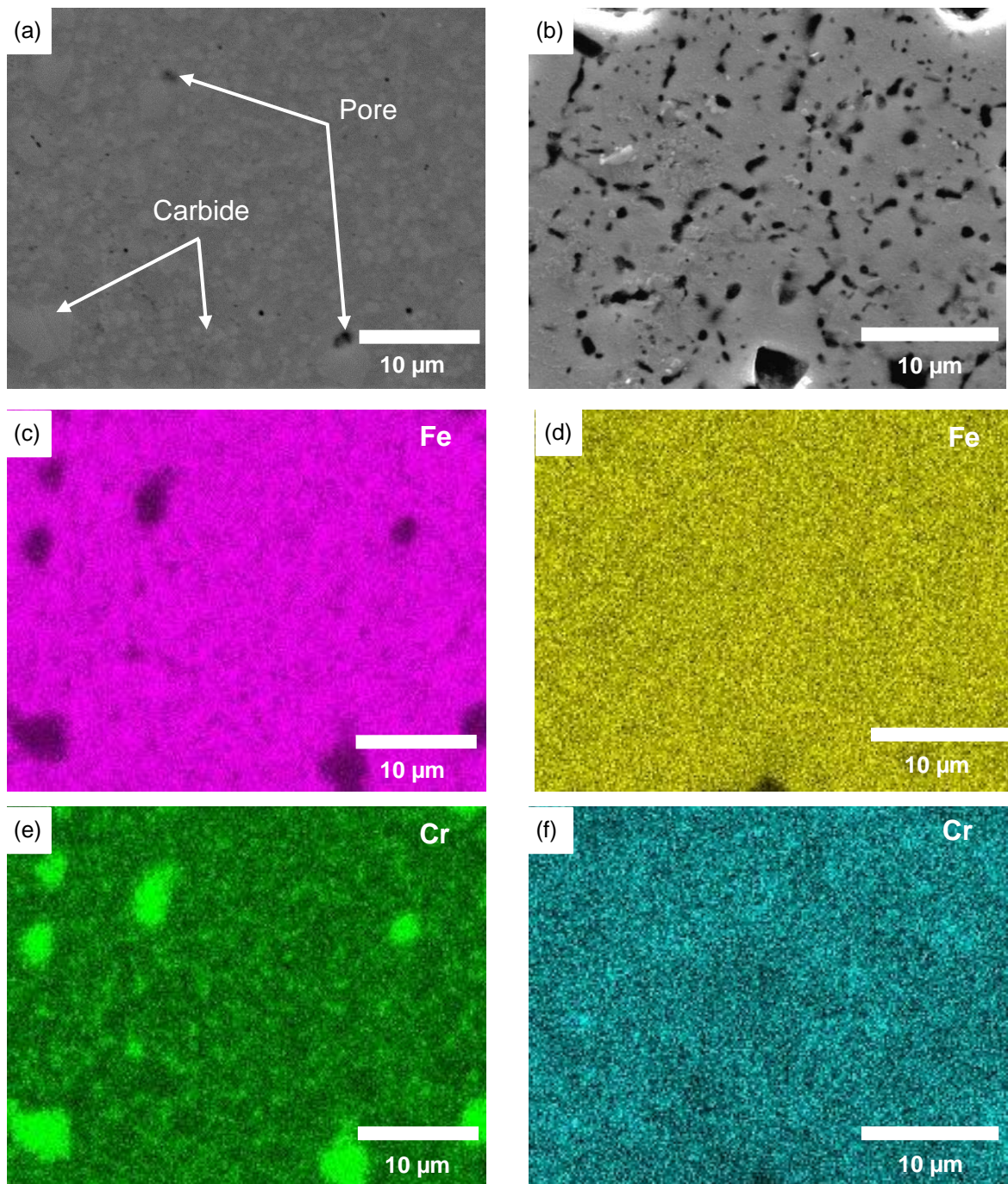
Figure 5-17: (a) Microstructure of tool before cyclic polarization (b) Microstructure of tool after cyclic polarization (c) Fe EDS-Map before cyclic polarization (d) Fe EDS-Map after cyclic polarization (e) Cr EDS-Map before cyclic polarization (f) Cr EDS-Map after cyclic polarization. After corrosion, the Cr carbides disappear. It shows the galvanic corrosion. Ferrite is the anode and carbide is the cathode. Ferrite around the carbide is corroded and the carbide falls off the surface.

To prove the anode and cathode phases in the galvanic corrosion of the 1.4112 material, SKPFM is done. Figure 5-18 (a) provides information about the morphology and edges of the phases in the material. The carbides of Cr with a size of fewer than 1 µm are illustrated in the matrix. The lines in the image are the result of surface

preparation. Figure 5-18 (b) shows the V_{CPD}. V_{CPD} between carbides and the tip is less than V_{CPD} between ferrite and the tip. Regarding Equation 5-3, there are:

$$eV_{CPD} = \phi_T - \phi_{Carbide} \qquad \text{5-4}$$

$$eV_{CPD} = \phi_T - \phi_{Fe} \qquad \text{5-5}$$

In Figure 5-18 (b), V_{CPD} is considered approximately for the carbide 1 V and the ferrite 10 V.

$\phi_T - \phi_{Carbide} = 1$ eV

$\phi_T - \phi_{Fe} = 10$ eV

As a result, there is:

$\phi_{Carbide} - \phi_{Fe} = 9$ eV

The result above shows that the carbides' work function is higher than ferrite. Consequently, carbides are cathodes, and ferrite is an anode during galvanic corrosion. It is assumed that the dominant mechanism for cathodic corrosion might be galvanic corrosion. To make sure further experiments and tests are carried out.
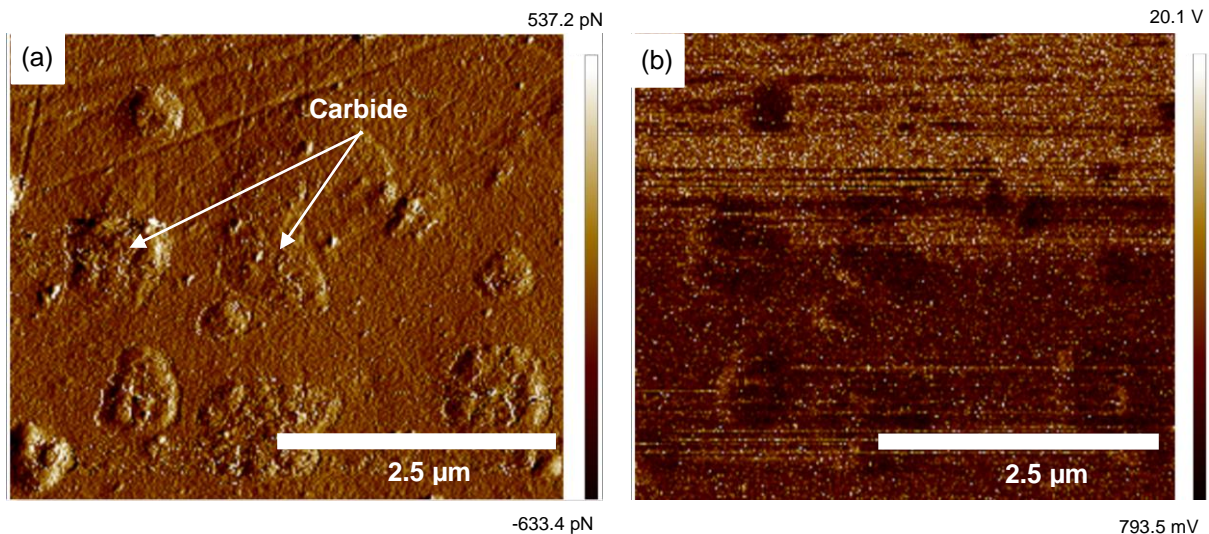
Figure 5-18: (a) Peak force error (b) potential showing the different potential and work function for ferrite and the carbide. Carbides' potential is less than ferrite.

5.3.2 Galvanic corrosion test on the cathode

Figure 5-19 compares the surface of the ferrite before and after the galvanic corrosion test. The ferrite surface is changed by corrosion. The grain boundaries are corroded, and some small pits in the nanometer range have appeared inside the

grains. There are distorted atomic arrangements and high free energy in the grain boundaries. In other words, the defects are closer to the grain boundaries, making this zone thermodynamically unstable and prone to oxidation and corrosion. Therefore, corrosion happens in these zones to reduce the energy level [149]. In addition, there are some pits inside of the grains. It is assumed that different crystallographic orientations lead to the electrochemical potential difference and many micro galvanic cells. The inhomogeneous distribution of strained and unstrained regions left behind by the metallurgical processes (such as fabrication, annealing, and shaping) gives rise to an inhomogeneous distribution of a large number of micro-sized galvanic cells, which, in a corrosive environment, causes the initiation and growth of localized corrosion [150].

This experiment shows the probability of having galvanic corrosion as the cathodic corrosion mechanism on the material 1.4112. Regarding complicated electrochemical reactions happening and the difference in the cathode with ECM and PECM, it is complicated to ensure that galvanic corrosion is the main mechanism for the damage to the tool. Other probable cathodic corrosion mechanisms are mentioned in chapter 5.1, which might be involved.
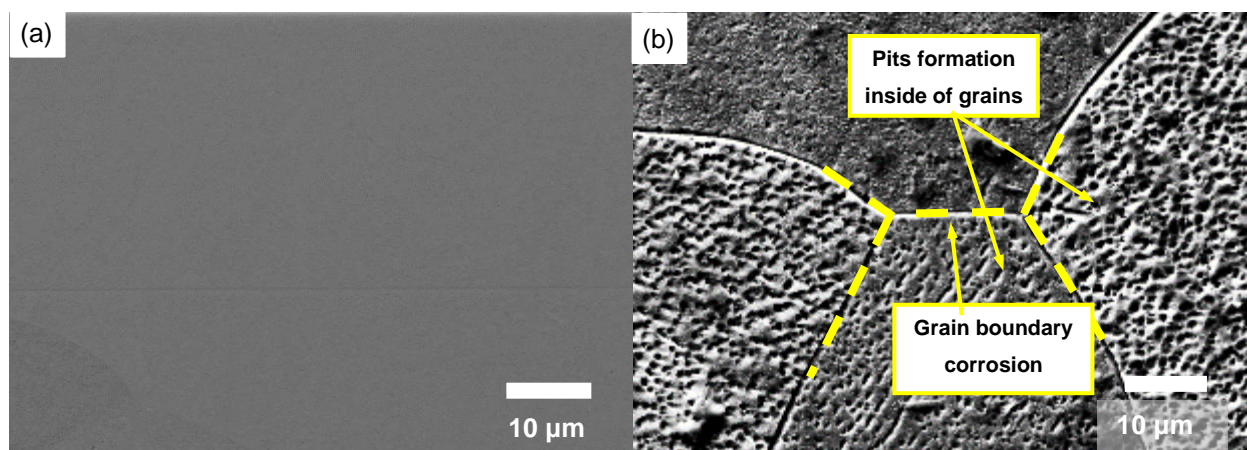
Figure 5-19: Microstructure of pure ferrite (a) before (b)after cathodic corrosion test by the coupled copper-ferrite cathode. The grain boundaries are corroded and some pits are formed inside of grains.

5.3.3 Laboratorial ECM

Figure 5-20 shows a few current vs. time plots acquired by EC-Lab software with different applied voltages. Each condition is repeated ten times, and just one of the plots for each (different voltages of 6 V, 8 V, and 10 V) is shown here. The current is

recorded every 0.1 s, which shows wobbling. However, the highest wobbling amount is about 0.2 A which is negligible. Production of metal hydroxide and hydrogen bubbles in the IEG decreases the conductivity and current. By flowing the electrolyte out of IEG and supplying fresh electrolyte, the conductivity, and current increase again, which causes wobbling of the current. In all plots, the current decreases by increasing time, showing that material removal is occurring and IEG increases.
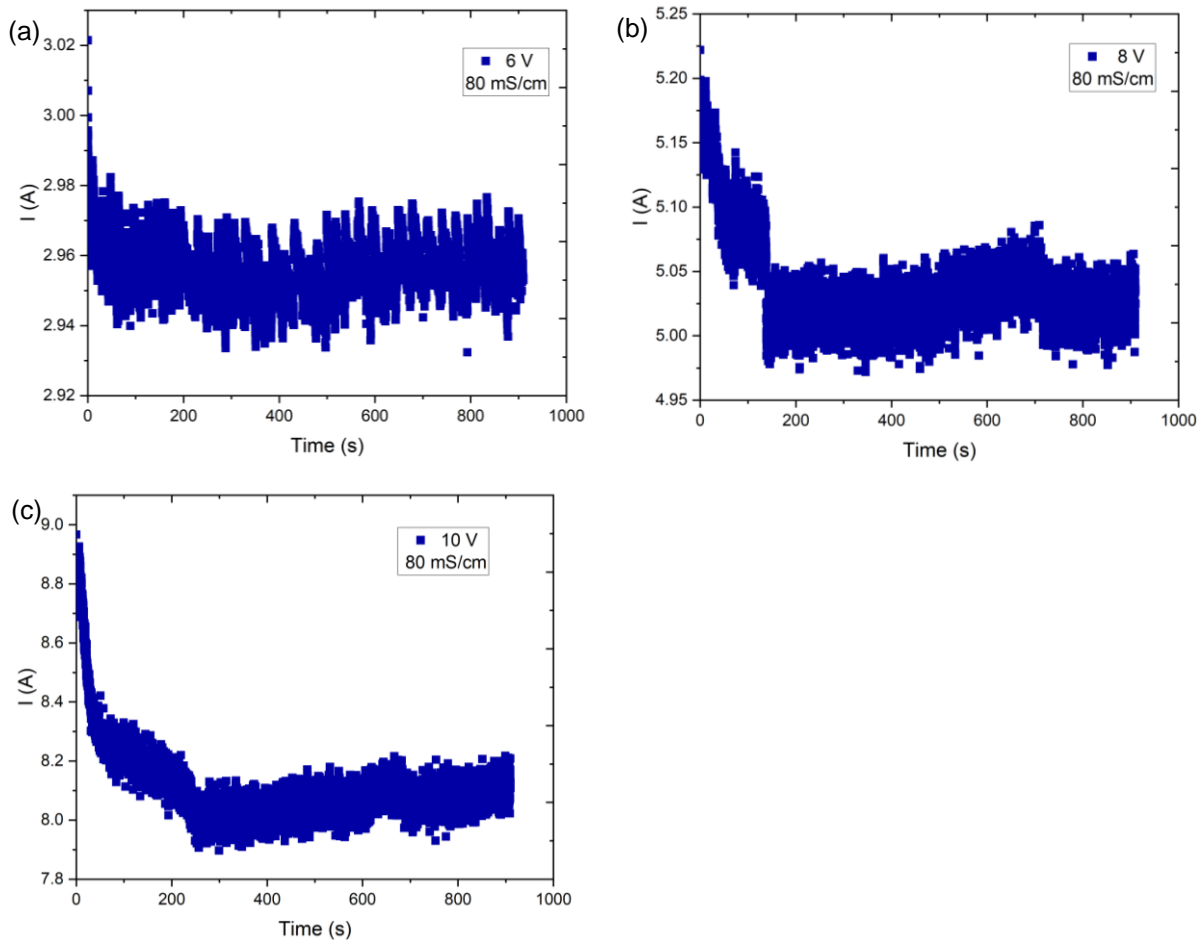
Figure 5-20: Current vs. time plots resulted from laboratorial setup with the help of EC-Lab software to compare the effect of applied voltage (c) 6 V, 80 mS/cm (d) 8 V, 80 mS/cm (e) 10 V, 80 mS/cm.

To simplify the plots and gain more information, lines are fitted to plots in Figure 5-20. Figure 5-21 shows the effect of the voltage changes in the laboratorial setup. The error bars show the current range in ten process repeats. The driven equation for 10 V is $y=-1.428×10^{-4}x+7.4243$, for 8 V is $y=-0.288×10^{-4}x+5.0587$ and for 6 V is $y=-0.142×10^{-4}x+2.9693$. Considering the constant in the equations as the measured current during the process, by increasing the applied voltage of 6 V, 8 V, and 10 V the currents are increasing by 2.9693 A, 5.0587 A, and 7.4243 A, respectively, due to

Ohm's law. In addition, by increasing the time, material removal increases, leading to increasing IEG and decreasing current. The equations' slopes show the voltage's effect in IEG and material removal. The smaller the slope of the equation, the less material removal and the less change in IEG. By increasing the voltage of 6 V, 8 V, and 10 V, the slopes increase by 0.142×10^{-4}, -0.288×10^{-4} and -1.428×10^{-4}, respectively. Higher voltage leads to more material removal and bigger IEG during ECM.
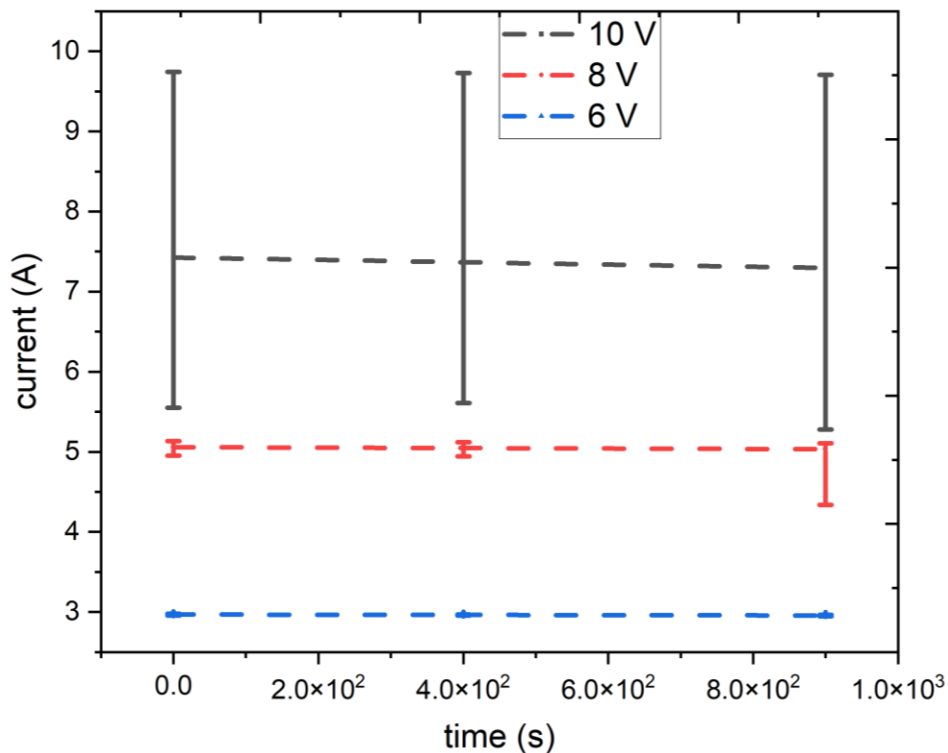
Figure 5-21: Effect of voltage and time on the current during ECM in laboratorial setup. By increasing the voltage the current produced during ECM increases. By increasing the time of ECM the current decreases. The decrease of current over time is more noticeable in higher voltages.

In the next step, the cathodic corrosion is investigated by changing the electrolyte conductivity, which shows the electrolyte concentration changes. Figure 5-22 shows some current vs. time plots by EC-Lab software, which compares the effect of electrolyte conductivity. The wobbling of current is happening; the highest amount is about 0.2 A and is negligible. The current is decreasing by increasing time showing the material removal.
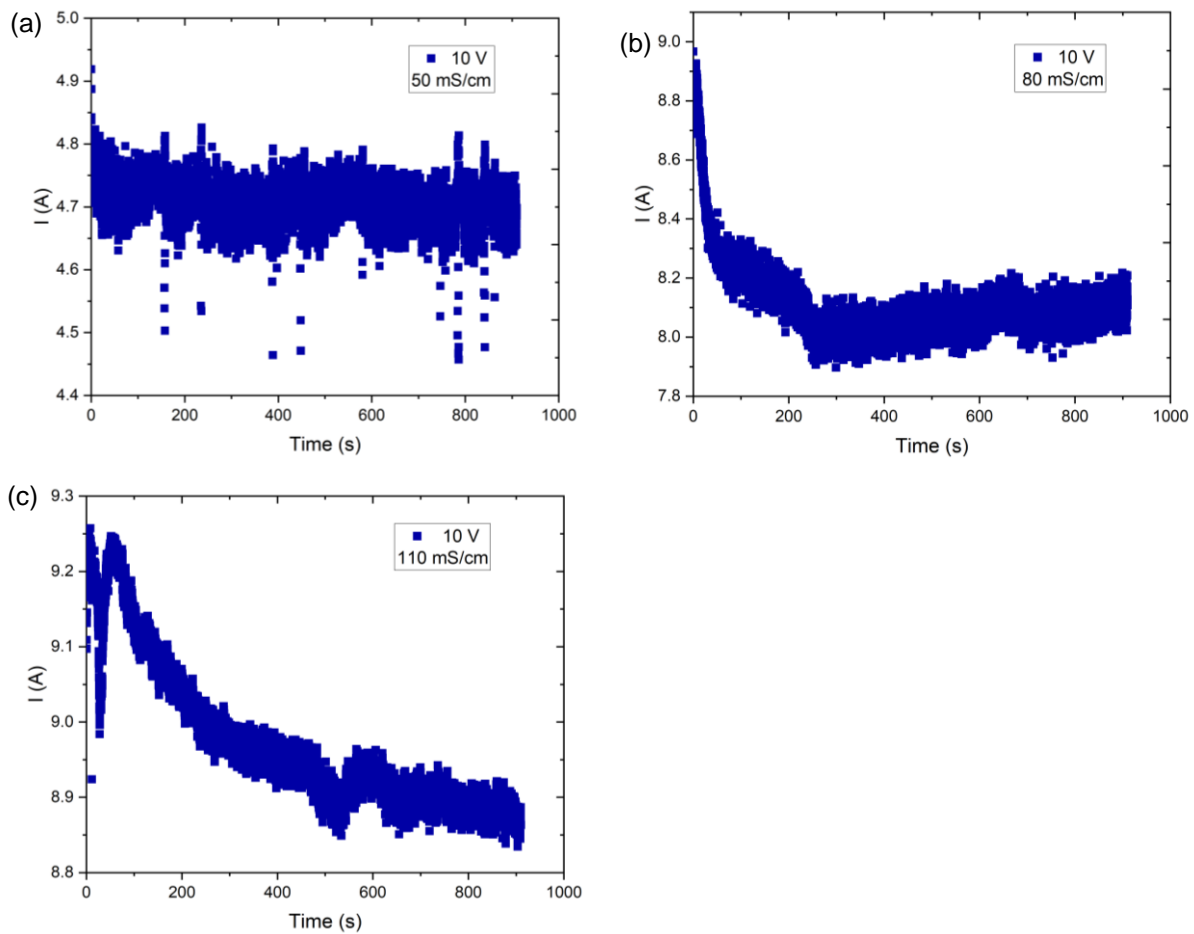
Figure 5-22: Current vs. time plots resulted from laboratorial setup with the help of EC-Lab software to compare the effect of electrolyte conductivity (concentration) (c) 10 V, 50 mS/cm (d) 10 V, 80 mS/cm (e) 10 V, 110 mS/cm.

A line fits each plot in Figure 5-22 to make it simple and gain more information. The effect of conductivity is shown in Figure 5-23. The error bars show the range of current considering 175 repeats of the process. The driven equation for 110 mS/cm is $y=-2.258\times10^{-4}x+8.6939$, for 80 mS/cm is $y=-1.428\times10^{-4}x+7.4243$ and for 50 mS/cm is $y=-0.071\times10^{-4}x+4.4052$. By increasing the conductivity of 50 mS/cm, 80 mS/cm, and 110 mS/cm, the current increases by 4.4052 A, 7.4243 A, and 8.6939 A, respectively. It is due to Ohm's law as in Equation 2-27. By increasing time, the current decreases, which the reason is as explained in Figure 5-21. The slope shows the amount of material removal by increasing the IEG. By increasing the conductivity of 50 mS/cm, 80 mS/cm, and 110 mS/cm, the slope increases by -2.258, -1.428, and -0.071, respectively, which shows that in higher conductivity, there is more material removal.
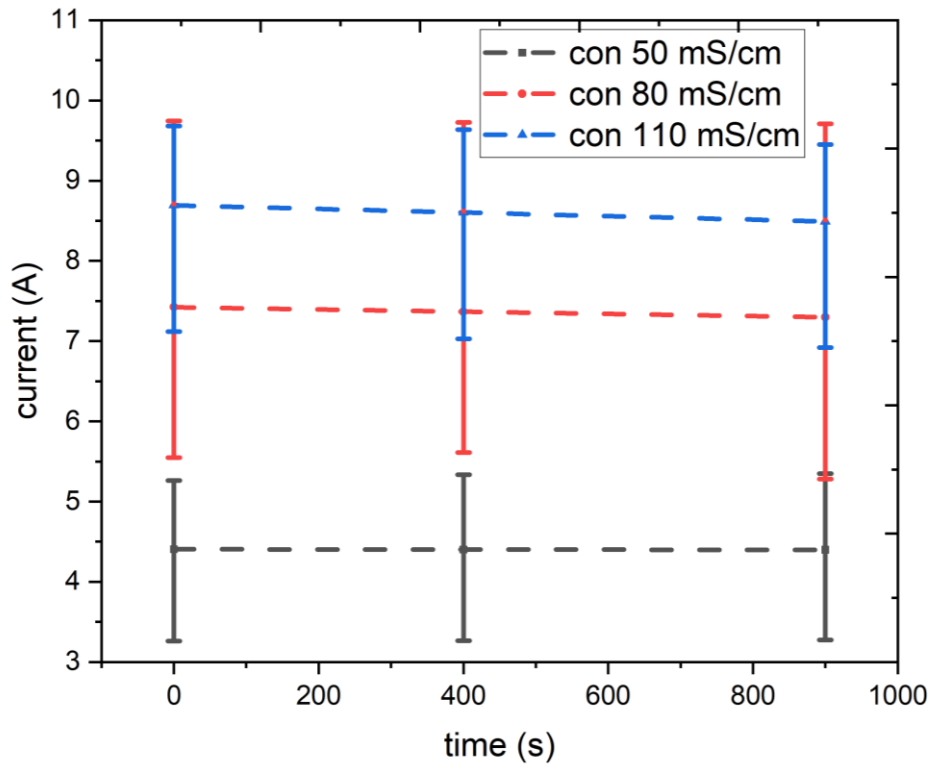
Figure 5-23: Effect of electrolyte concentration and time on the current during ECM in laboratorial setup. By increasing the conductivity the current produced during ECM increases. By increasing the time of ECM the current decreases. The decrease of current over time is more noticeable in higher conductivities.

The FESEM results are shown in Figure 5-24. Fewer pits are formed with 50 mS/cm conductivity in Figure 5-24 (a) compared to the conductivity of 80 mS/cm in Figure 5-24 (b). By increasing conductivity, the concentration of the salt in the electrolyte increases. In other words, more alkali ions of Na^+ are available in higher conductivity, which are the main agent causing cathodic corrosion.

By increasing the conductivity from 80 mS/cm to 110 mS/cm, it is expected to see more pits and damage on the tool surface, but the damage is less in Figure 5-24 (c).
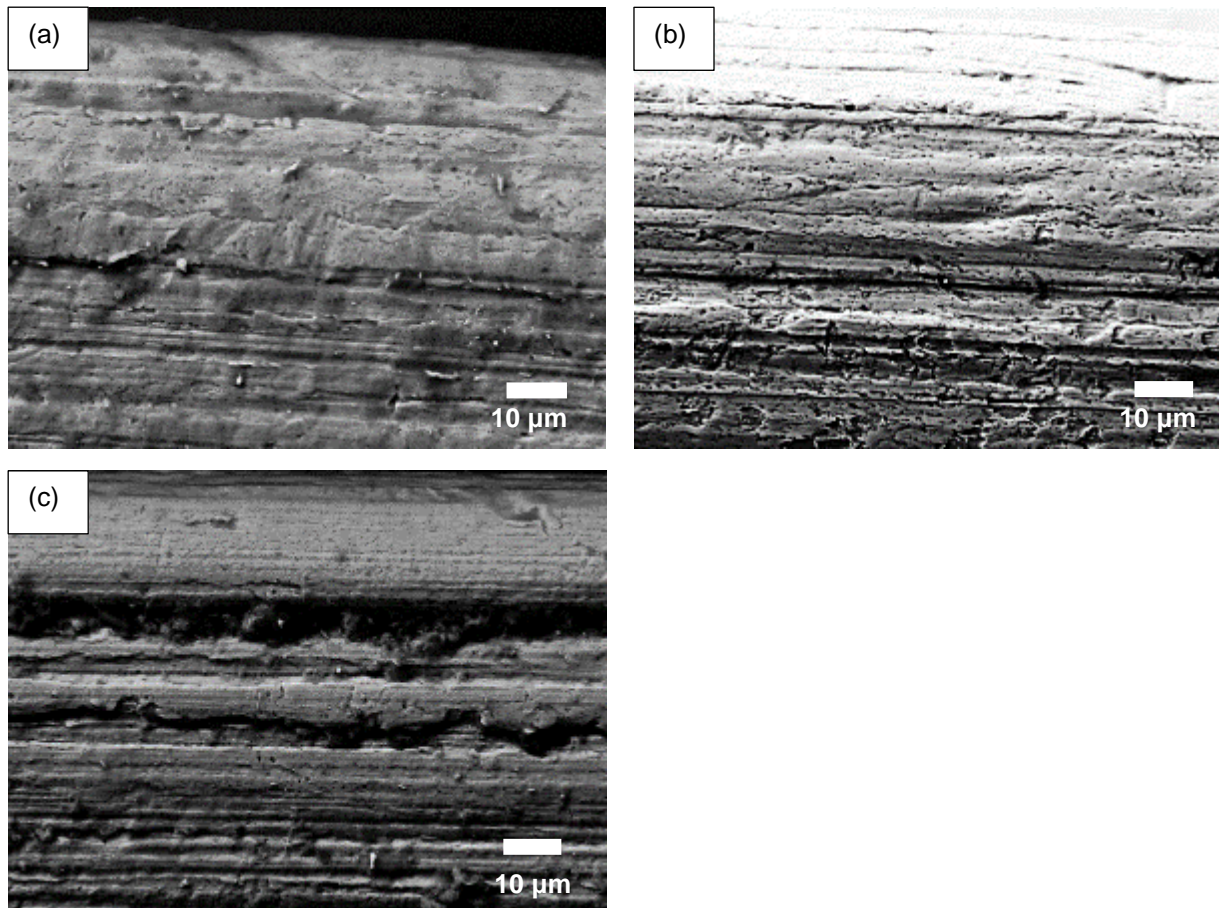
Figure 5-24: Surface of the tool after 175 cycles ECM in laboratorial setup and electrolyte with conductivity (a) 50 mS/cm (b) 80 mS/cm (c) 110 mS/cm. By increasing or decreasing the conductivity from 80 mS/cm, the pits' formation is reduced.

Figure 5-25, Figure 5-26, and Figure 5-27 show the surface of the tool with the help of EDS-Map in different electrolyte conductivity. In all conductivities, the tool shows the ferrite with Cr carbides distributed in ferrite (Cr in EDS-Map exists as the Cr carbide). A comparison between these Figures and Figure 5-17 shows that the type of corrosion and the activated mechanism is different. Figure 5-17 and related chapter 5.3.1 shows that by having galvanic corrosion, the Cr carbides disappear. But here, for all conductivities, the Cr carbides exist. As a result, a mechanism, or mechanisms other than galvanic corrosion, is activated. In addition, Figure 5-26, showing the damage on the tool in 80 mS/cm, illustrates that the damages exist in both phases of ferrite and Cr carbides. Consequently, it is not recognizable that corrosion is started on ferrite or carbides. The corrosion may be only on Fe or on Cr carbides (by corrosion, carbides disappear and show the Fe in EDS-Map). Moreover, corrosion may happen on both phases.
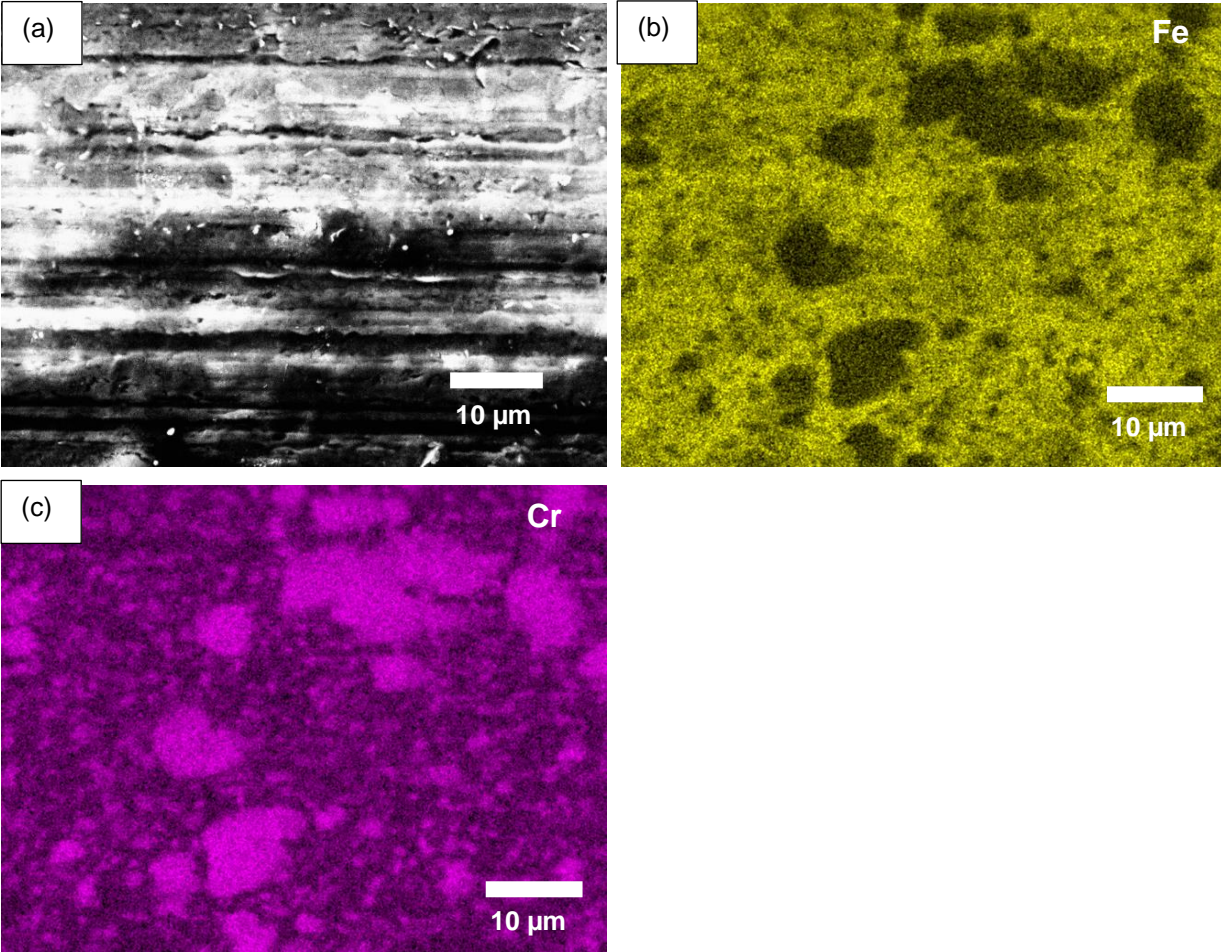
Figure 5-25: (a) Surface of the tool in 50 mS/cm (b) Fe EDS-Map of the tool in 50 mS/cm (c) Cr EDS-Map of the tool in 50 mS/cm. The microstructure consists of Fe and Cr carbides.
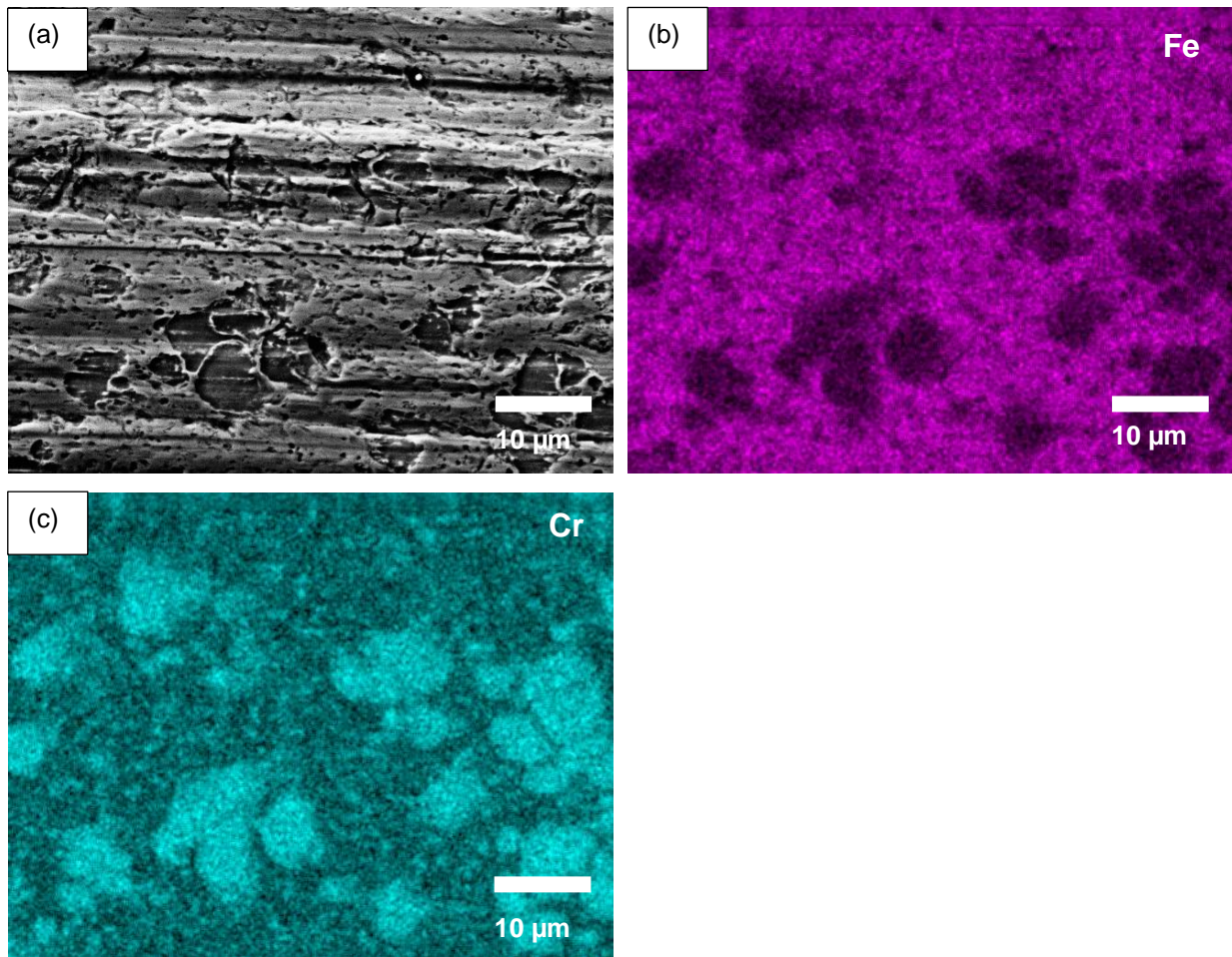
Figure 5-26: (a) Surface of the tool in 80 mS/cm (b) Fe EDS-Map of the tool in 80 mS/cm (c) Cr EDS-Map of the tool in 80 mS/cm. The microstructure consists of Fe and Cr carbides. Pits and damages are formed in both phases during ECM.
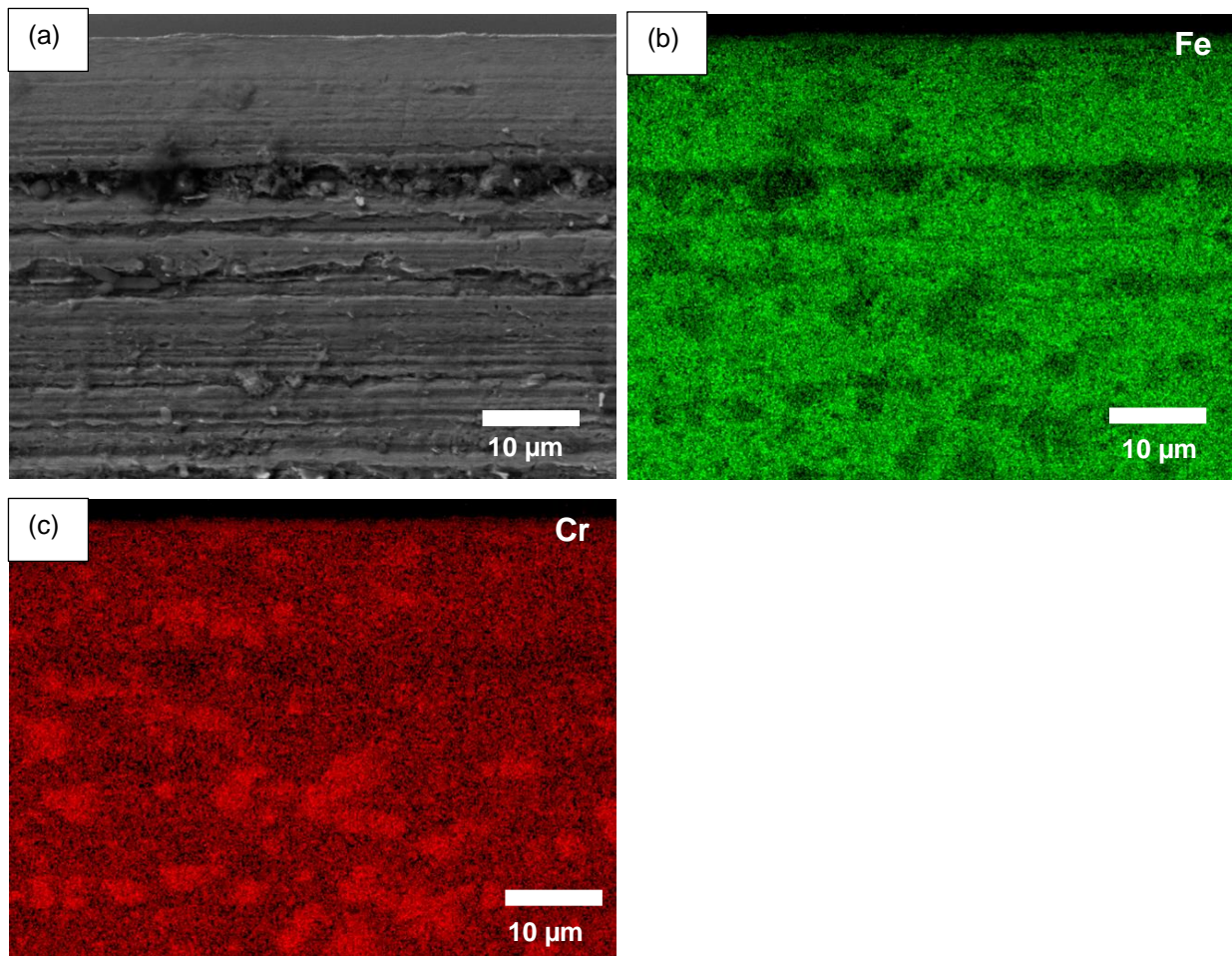
Figure 5-27: (a) Surface of the tool in 110 mS/cm (b) Fe EDS-Map of the tool in 110 mS/cm (c) Cr EDS-Map of the tool in 110 mS/cm after ECM. The microstructure consists of Fe and Cr carbides.

Between different mechanisms proposed for cathodic corrosion in chapter 5, alloying with alkali metal is not the responsible mechanism, as Cr and Fe cannot make the intermetallic compound with Na. Making an intermetallic compound is necessary to make the alloy and activate this mechanism.

It is complicated to talk about other mechanisms indeed, the same way as alloying with alkali metal, because: 1. It is not clear that corrosion is started on Fe or Cr carbides. 2. In most studies in the cathodic corrosion field, the cathode is pure, making understanding electrochemical reactions easier. In this study, the cathode is martensitic stainless steel with a matrix of ferrite and carbides of Cr. It is mentioned in a study [71] that Fe and Cr have corrosion with the cathodic etching mechanism. In this mechanism, anions of Fe or Cr are formed instead of cations. They get the electron from Na^+ and make the metal anions or anionic clusters on the cathode. Because of water electrolysis, the dynamic water layer next to the cathode surface has high pH. It helps the metal anions or anionic clusters to detach from the cathode

and face the oxidant (in this study, water is the oxidant). Depending on the working condition and materials, they can turn to metal or oxide of the metal. Regarding the higher tendency of Cr to get an electron from Na than Fe, it is believed that if this mechanism is activated and corrosion starts from Cr. In addition, another consideration assumes that adsorbed hydrogen plays a key role in cathodic corrosion [142]. Ternary metal hydrides ($A_xM_yH_z$, A=alkali metal, M=transition metal, H=hydride) are formed, which act as an elusive intermediate during cathodic etching. The results of hydrogen diffusion in chapter 3.3.2 show that hydrogen diffusion to the sample occurs which may help with this mechanism in cathodic corrosion.

The other probable mechanism is the formation of metal hydrides. Generally, the hydride is unstable at room temperature, and the elements of groups 6, 7, and 8 do not form hydrate at room temperature. However, Cr is an exception that forms hydrate and CrH_2 is a more stable form. To form it, H^+ is needed, which is produced by water electrolysis (diffusion of the hydrogen in the tool shown in chapter 3.3.2 proves the production of hydrogen). It provides the atomic hydrogen on the surface, which may help with this mechanism. The Cr-H bond forms in the interface of the cathode and electrolyte. Later, the hydrate can react with the oxidizer (water) and produce metal or oxide of the metal. The hydrate of Fe is not stable, but the probability of formation is still not neglectable. In addition, it is unclear if the hydrate complex of other elements of the cathode also exists.

More experiments in the future are needed to find the active mechanism. However, hydrogen might affect the mechanism because a high amount of hydrogen is produced during ECM and PECM. Chapter 3.3.2 shows that the high amount of produced hydrogen on the tool leads to hydrogen diffusion into the cathode. It is evidence of the production of H^+ on the surface. All produced hydrogen does not diffuse into the cathode. This hydrogen stays on the cathode's surface and helps with the corrosion mechanism. The best possible mechanism matching the results of this study is the cathodic corrosion by the formation of the metal hydrides. Increasing electrolyte conductivity (concentration) produces more hydrogen on the surface. Hydrogen is the main agent for causing cathodic corrosion.

In addition, the results in chapter 3.3.2 show that the magnetite forms on the surface of the cathode. Based on the Pourbaix diagram, magnetite forms at higher pH. At high pH, not only magnetite is stable, but also the hydride of iron has the chance of formation (Figure 3-8). As a result, more damage on the tool in conductivity of

80 mS/cm compared to 50 mS/cm is observed by the hydride formation mechanism. By increasing conductivity from 80 mS/cm to 110 mS/cm, it is expected to see more damage, but the damage is reduced. It might be because of having more Na^+ cations, which adsorb more to the cathode surface, leading to less available surface for hydrogen to form metal hydrides on the surface. Consequently, damage on the surface of the tool is reduced.

5.4 Conclusion

Cathodic corrosion is investigated in three steps:

1. Cyclic polarization on the 1.4112 material shows that galvanic corrosion occurs. Ferrite is the anode and Cr carbides are the cathodes. By corrosion of the ferrite around the carbide, carbide comes off the surface.

2. Galvanic corrosion with the PECM working condition on the two cathodes-setup (ferrite and Cu) occurs and the ferrite is corroded. It shows that with the defined working condition, corrosion on the cathode is possible.

3. The conductivity (concentration) of the electrolyte is investigated with the laboratorial ECM setup. In high and low conductivity the formation of the pits is decreased. It is theoretically proved that the hydride formation mechanism is the mechanism for damaging and forming pits on the tool.

6   Summary and outlook

This work aims to investigate electrochemical machining (ECM) and pulsed electrochemical machining (PECM) **from the tool side** point of view. This helps with making a better definition of working conditions to have a higher lifetime of the tool and precisely machined workpiece for long-term application. At the beginning of this work, the general theoretical background and basics of the ECM and PECM are explained. Based on the theoretical information, a developed setup is designed to be mounted in the PECM machine, and material **1.4112 is used as the tool** for PECM. The microstructural microscopy of the tool reveals a ferrite matrix with Cr carbides distributed in the matrix. The phases are confirmed with the help of XRD. After a long-term PECM, the changes and **pits' formation** on the tool's surface is observed which is illustrated in Figure 2-29. It leads to proposing three hypotheses as the cause of the changes on the tool to be investigated. The hypotheses are **hydrogen embrittlement, cavitation erosion, and cathodic corrosion**.

Hydrogen embrittlement is important to be considered as during ECM and PECM, specially by employing high voltages, a considerable amount of hydrogen is produced. The hydrogen penetrates into the tool if the condition is in favor of the hydrogen diffusion. Hydrogen embrittlement occurs when three perquisites exist simultaneously:

1. The metal condition must be suitable for hydrogen diffusion. That means suitable places for hydrogen in the microstructure should exist. 1.4112 material has BCC structure (ferrite) which increases the probability of having hydrogen embrittlement.

2. The presence of atomic hydrogen to diffuse into the material is necessary. During PECM, especially industrial applications, high potentials are used. Hydrogen production as a result of the electrolysis of water increases in high potentials. In this study, by having a high potential of 13 V, thermal desorption spectroscopy (TDS) test reveals that 6.8 ppm hydrogen exists in the tool.

3. Tensile stress is the last prerequisite for hydrogen embrittlement. In this study, the residual stress is measured, and the result is compressive residual stress, which causes no damage to the tool. The result is shown in Figure 3-12.

Consequently, although the material is susceptible to hydrogen embrittlement and the hydrogen penetrates into the tool but because of no tensile stress on the tool hydrogen embrittlement does not occur.

Cavitation erosion occurs based on Bernoulli's equation when the flow of the pattern is changed and the pressure decreases. The oscillation in the tool is assumed as a parameter affecting the pattern of the flow. The next hypothesis which is investigated is cavitation erosion which may be caused by the oscillation of the tool. In this step, the oscillation of the tool is excluded, but still, the pits form on the tool. In addition, the time of the PECM is decreased which proved that the tool damages are a short-term effect. The surface images of the tools in different conditions are shown in Figure 4-4.

The last hypothesis is **cathodic corrosion**, which happens in alkali electrolytes and high pH. In this experiment, $NaNO_3$ provides the alkali metal in the electrolyte. In addition, the electrolysis of water at the tool's surface increases the local pH during PECM. As this approach of the experiment has not been defined before, different experiments are done.

1. Cyclic polarization on the 1.4112 material is done to find the corrosion mechanism of this material. It is believed that the mechanism might be the same during cathodic corrosion on the tool during PECM. The type of corrosion is galvanic corrosion, the way that Cr carbides are the cathode and ferrite is the anode. The corroded material is shown in Figure 5-17.

2. A setup is designed and two materials (Cu, which is noble, and Fe, which is active) are used simultaneously as the cathode. The goal is to investigate the probability of having galvanic corrosion with the working condition of PECM. The result in Figure 5-19 shows the corrosion of Fe by having galvanic corrosion.

3. As the last step, an easy-to-use small setup is designed to investigate cathodic corrosion in ECM by varying the concentration of the electrolyte. The result shows that concentration affects the formation of the pits in Figure 5-24. By increasing or decreasing the concentration from the working condition of PECM in Table 2-5, the formation of the pits is less. In addition, this experiment proves that galvanic corrosion is not the mechanism that causes pits' formation on the tool. The hydride formation mechanism is believed to be the active mechanism for damaging and forming pits on the tool.

Considering the data acquired, **cathodic corrosion** affects the tool during ECM and PECM.

For further investigation, the theoretically proven mechanism for cathodic corrosion in this work, namely hydride formation, is suggested to be investigated to provide more evidence of hydride existence. As the next step, the elements involved in cathodic corrosion should be defined. Based on reviewing theoretical information, it is believed that any parameter affecting the current density might affect cathodic corrosion. However, in all experiments, the effect of ions in the electrolyte and electrochemical reactions has to be considered.

7 References

[1]   X. Zhengyang and W. Yudi, "Electrochemical machining of complex components of aero-engines: Developments, trends, and technological advances," *Chinese Journal of Aeronautics,* vol. 34, no. 2, pp. 28-53, 2021.

[2]   Z. Pandilov, "Application of Electro Chemical Machining for materials used in extreme conditions," in *IOP Conference Series: Materials Science and Engineering*, 2018, vol. 329, no. 1: IOP Publishing, p. 012014.

[3]   J. Bannard, "Electrochemical machining," *Journal of Applied Electrochemistry,* vol. 7, no. 1, pp. 1-29, 1977.

[4]   "http://electrochemicalmachining.com/technology/process-history." (accessed 23.01.2023).

[5]   "https://en.wikipedia.org." (accessed 23.01.2023).

[6]   B. Bhattacharyya, *Electrochemical micromachining for nanofabrication, MEMS and nanotechnology*. William Andrew, 2015.

[7]   F. C. Walsh, "The Overall Rates of Electrode Reactions: Faraday's Laws of Electrolysis," *Transactions of the IMF,* vol. 69, no. 4, pp. 155-157, 1991/01/01 1991, doi: 10.1080/00202967.1991.11870914.

[8]   *DIN 8590: Fertigungsverfahren Abtragen*, Berlin, 2003.

[9]   A. Ernst, "Analyse und Modellierung der Einflüsse auf das Arbeitsergebnis der elektrochemischen Bearbeitung hochtemperaturfester Werkstoffe für Turbinenstrahltriebwerke," Dissertation, Universität des Saarlandes, 2020.

[10]   X. H. Li, Z. L. Wang, W. Zhao, and F. Q. Hu, "Pulsed micro-electrochemical machining technology," in *Key Engineering Materials*, 2007, vol. 339: Trans Tech Publ, pp. 327-331.

[11]   J. Yao, Z. Chen, Y. Nie, and Q. Li, "Investigation on the electrochemical machining by using metal reinforced double insulating layer cathode," *The International Journal of Advanced Manufacturing Technology,* vol. 89, no. 5, pp. 2031-2040, 2017.

[12]   G. Liu, Y. Li, Q. Kong, and H. Tong, "Research on ECM process of micro holes with internal features," *Precision Engineering,* vol. 47, pp. 508-515, 2017.

[13]   A. k Swain, "Preparation of coated microtools for electrochemical machining applications," Master Thesis, University of Nebraska, 2010.

[14]   D. Mi and W. Natsu, "Design of ECM tool electrode with controlled conductive area ratio for holes with complex internal features," *Precision Engineering,* vol. 47, pp. 54-61, 2017.

[15]   K. Weißhaar, M. Weinmann, A. Jung, O. Weber, and H. Natter, "Replication of microstructured tools for electrochemical machining applications," *The International Journal of Advanced Manufacturing Technology,* vol. 82, no. 1, pp. 197-209, 2016.

[16]   F. Wang, J. Zhao, Y. Lv, Z. Yang, W. Gan, and Z. Tian, "Precise vibrating electrochemical machining of a diamond-shaped hole with side-wall insulation," *Proceedings of the Institution of Mechanical Engineers, Part C: Journal of Mechanical Engineering Science,* vol. 232, no. 17, pp. 2987-2997, 2018.

[17]   R. N. Muir, "The parameterisation of electrochemical machining," Dissertation, University of Edinburgh, 2006.

[18]   T. Paczkowski and A. Troszyński, "The effect of multidirectional vibration on electrochemical machining," *Procedia Manufacturing,* vol. 22, pp. 41-48, 2018.

[19] J. Deconinck, G. Maggetto, and J. Vereecken, "Calculation of current distribution and electrode shape change by the boundary element method," *Journal of the Electrochemical Society,* vol. 132, no. 12, p. 2960, 1985.

[20] V. Jain and K. Rajurkar, "An integrated approach for tool design in ECM," *Precision engineering,* vol. 13, no. 2, pp. 111-124, 1991.

[21] O. Narayanan, S. Hinduja, and C. Noble, "The prediction of workpiece shape during electrochemical machining by the boundary element method," *International Journal of Machine Tool Design and Research,* vol. 26, no. 3, pp. 323-338, 1986.

[22] K. Rajurkar *et al.*, "Micro and nano machining by electro-physical and chemical processes," *CIRP annals,* vol. 55, no. 2, pp. 643-666, 2006.

[23] F. Klocke, M. Zeis, S. Harst, A. Klink, D. Veselovac, and M. Baumgärtner, "Modeling and simulation of the electrochemical machining (ECM) material removal process for the manufacture of aero engine components," *Procedia Cirp,* vol. 8, pp. 265-270, 2013.

[24] J. C. da Silva Neto, E. M. Da Silva, and M. B. Da Silva, "Intervening variables in electrochemical machining," *Journal of Materials Processing Technology,* vol. 179, no. 1-3, pp. 92-96, 2006.

[25] N. Jain and V. Jain, "Optimization of electro-chemical machining process parameters using genetic algorithms," *Machining Science and Technology,* vol. 11, no. 2, pp. 235-258, 2007.

[26] R. Muir, D. Curry, F. Mill, A. Sherlock, and A. Mount, "Real-time parameterization of electrochemical machining by ultrasound measurement of the interelectrode gap," *Proceedings of the Institution of Mechanical Engineers, Part B: Journal of Engineering Manufacture,* vol. 221, no. 4, pp. 551-558, 2007.

[27] V. Jain and P. Pandey, "Tooling design for ECM," *Precision engineering,* vol. 2, no. 4, pp. 195-206, 1980.

[28] V. Jain and P. Pandey, "Design and analysis of ECM toolings," *Precision Engineering,* vol. 1, no. 4, pp. 199-206, 1979.

[29] D. Clifton, A. Mount, F. Mill, and P. Howarth, "Characterization and representation of non-ideal effects in electrochemical machining," *Proceedings of the Institution of Mechanical Engineers, Part B: Journal of Engineering Manufacture,* vol. 217, no. 3, pp. 373-385, 2003.

[30] Z. Zeng, Y. Wang, Z. Wang, D. Shan, and X. He, "A study of micro-EDM and micro-ECM combined milling for 3D metallic micro-structures," *Precision Engineering,* vol. 36, no. 3, pp. 500-509, 2012.

[31] R. J. Leese, "Electrochemical machining-new machining targets and adaptations with suitability for micromanufacturing," Dissertation, Brunel University London, 2016.

[32] H. Wendt and G. Kreysa, *Electrochemical engineering: science and technology in chemical and other industries*. Springer Science & Business Media, 1999.

[33] M. E. Inman, E. J. Taylor, A. Lozano-Morales, H. Garich, and T. Hall, "Electrochemical system and method for machining strongly passivating metals," ed: Google Patents, 2011.

[34] B. Bhattacharyya, J. Munda, and M. Malapati, "Advancement in electrochemical micro-machining," *International Journal of Machine Tools and Manufacture,* vol. 44, no. 15, pp. 1577-1589, 2004.

[35] S. Ayyappan and K. Sivakumar, "Experimental investigation on the performance improvement of electrochemical machining process using

oxygen-enriched electrolyte," *The International Journal Of Advanced Manufacturing Technology,* vol. 75, no. 1, pp. 479-487, 2014.

[36] S. Ayyappan and K. Sivakumar, "Investigation of electrochemical machining characteristics of 20MnCr5 alloy steel using potassium dichromate mixed aqueous NaCl electrolyte and optimization of process parameters," *Proceedings of the Institution of Mechanical Engineers, Part B: Journal of Engineering Manufacture,* vol. 229, no. 11, pp. 1984-1996, 2015.

[37] W. Han, "Research on Micro Electrochemical Machining Using Electrostatic Induction Feeding Method," Dissertation, The University of Tokyo, 2016.

[38] X. Wu, N. Qu, Y. Zeng, and D. Zhu, "Modelling of the liquid membrane electrochemical etching of a nano-tip," *The International Journal of Advanced Manufacturing Technology,* vol. 69, no. 1, pp. 723-729, 2013.

[39] D. S. Bilgi, V. Jain, R. Shekhar, and S. Mehrotra, "Electrochemical deep hole drilling in super alloy for turbine application," *Journal of materials processing technology,* vol. 149, no. 1-3, pp. 445-452, 2004.

[40] Z.-W. Fan, L.-W. Hourng, and M.-Y. Lin, "Experimental investigation on the influence of electrochemical micro-drilling by short pulsed voltage," *The International Journal of Advanced Manufacturing Technology,* vol. 61, no. 9, pp. 957-966, 2012.

[41] B. Bhattacharyya and J. Munda, "Experimental investigation on the influence of electrochemical machining parameters on machining rate and accuracy in micromachining domain," *International Journal of Machine Tools and Manufacture,* vol. 43, no. 13, pp. 1301-1310, 2003.

[42] D. S. Bilgi, V. Jain, R. Shekhar, and A. V. Kulkarni, "Hole quality and interelectrode gap dynamics during pulse current electrochemical deep hole drilling," *The International Journal of Advanced Manufacturing Technology,* vol. 34, no. 1, pp. 79-95, 2007.

[43] V. Rathod, B. Doloi, and B. Bhattacharyya, "Experimental investigations into machining accuracy and surface roughness of microgrooves fabricated by electrochemical micromachining," *Proceedings of the Institution of Mechanical Engineers, Part B: Journal of Engineering Manufacture,* vol. 229, no. 10, pp. 1781-1802, 2015.

[44] H. S. Altena, "Precision ECM by process characteristic modelling," Dissertation, Glasgow Caledonian University, 2000.

[45] T. R. Münninghoff, "Mechanismen der anodischen Auflösung von Metallen und Legierungen bei extrem hohen Stromdichten," Dissertation, Heinrich-Heine-Universität Düsseldorf, 2012.

[46] T. Wagner, "High rate electrochemical dissolution of iron-based alloys in NaCl and NaNO3 electrolytes," Dissertation, Universität Stuttgart, 2002.

[47] P. Steuer, "Gepulste elektrochemische Bearbeitung von Kupferelektroden und deren Einsatz zur funkenerosiven Strukturierung von Hartmetall," Dissertation, Universität des Saarlandes, 2015.

[48] A. Rebschläger, "Recording, processing and use of material-specific data in pulse electrochemical machining," Dissertation, Universität des Saarlandes, 2015.

[49] W. Clark and J. McGeough, "Temperature distribution along the gap in electrochemical machining," *Journal of applied electrochemistry,* vol. 7, no. 4, pp. 277-286, 1977.

[50] M. Datta and D. Landolt, "On the role of mass transport in high rate dissolution of iron and nickel in ECM electrolytes—I. Chloride solutions," *Electrochimica Acta,* vol. 25, no. 10, pp. 1255-1262, 1980.

[51]   M. POURBEIX, "Atlas of electrochemical equilibria in aqueous solution," *Corrosion Science,* vol. 10, p. 343, 1966.

[52]   G. Alder, D. Clifton, and F. Mill, "A direct analytical solution to the tool design problem in electrochemical machining under steady state conditions," *Proceedings of the Institution of Mechanical Engineers, Part B: Journal of Engineering Manufacture,* vol. 214, no. 8, pp. 745-750, 2000.

[53]   B. Bhattacharyya, S. Mitra, and A. Boro, "Electrochemical machining: new possibilities for micromachining," *Robotics and Computer-Integrated Manufacturing,* vol. 18, no. 3-4, pp. 283-289, 2002.

[54]   K. Prashanth, D. S. Patel, V. Jain, and J. Ramkumar, "Numerical modelling of ECMM of micro-dimples considering the effect of 3-phase electrolyte," *Journal of Micromanufacturing,* vol. 2, no. 2, pp. 95-109, 2019.

[55]   J. Kozak, K. Rajurkar, and B. Wei, "Modelling and analysis of pulse electrochemical machining (PECM)," 1994.

[56]   K. Rajurkar, J. Kozak, B. Wei, and J. McGeough, "Study of pulse electrochemical machining characteristics," *CIRP annals,* vol. 42, no. 1, pp. 231-234, 1993.

[57]   Y. Chen, M. Fang, and L. Jiang, "Multiphysics simulation of the material removal process in pulse electrochemical machining (PECM)," *The International Journal of Advanced Manufacturing Technology,* vol. 91, no. 5, pp. 2455-2464, 2017.

[58]   J. Kozak, K. Lubkowski, and J. Peronczyk, "Accuracy problems of the pulse electrochemical machining," in *Proceedings of the Twenty-second International Machine Tool Design and Research Conference*, 1982: Springer, pp. 353-360.

[59]   I. Schaarschmidt, M. Hackert-Oschätzchen, G. Meichsner, M. Zinecker, and A. Schubert, "Implementation of the machine tool-specific current and voltage control characteristics in multiphysics simulation of electrochemical precision machining," *Procedia CIRP,* vol. 82, pp. 237-242, 2019.

[60]   V. Savas, C. Ozay, and H. Ballikaya, "Experimental investigation of cutting parameters in machining of 100Cr6 with tangential turn-milling method," *Advances in Manufacturing,* vol. 4, no. 1, pp. 97-104, 2016.

[61]   H. L. Klocke F, Zeis M, Kling A., "Clarification of gap phenomena in precise electrochemical machining by implementing a" virtual sensor," presented at the 13th International Symposium on ElectroChemical Machining Technology, INSECT, Dresden, 2017.

[62]   D. Clifton, "Process characterisation for electrochemical machining," Dissertation, University of Edinburgh, 2001.

[63]   M. Chai, Z. Li, H. Yan, and X. Sun, "Experimental investigations on aircraft blade cooling holes and CFD fluid analysis in electrochemical machining," *Advances in Materials Science and Engineering,* vol. 2019, 2019.

[64]   A. Festas, A. Ramos, and J. P. Davim, "Machining of titanium alloys for medical application-a review," *Proceedings of the Institution of Mechanical Engineers, Part B: Journal of Engineering Manufacture,* vol. 236, no. 4, pp. 309-318, 2022.

[65]   "https://www.voxelinnovations.com/post/pecm-and-orthopedic-devices." (accessed 23.01.2023).

[66]   O. Weber, "Gepulste elektrochemische Auflösung und Oberflächenausbildung von Gusseisenwerkstoffen in $NaNO_3$-Elektrolyten: Charakterisierung und Prozessauslegung," Dissertation, Universität des Saarlandes, 2016.

[67]   A. B. Kamaraj and M. M. Sundaram, "Reducing tool wear in micro electrochemical machining by cryogenic treatment," *International Journal of Manufacturing Research,* vol. 9, no. 3, pp. 333-344, 2014.

[68]   M. S. Park and C. N. Chu, "Micro-electrochemical machining using multiple tool electrodes," *Journal of Micromechanics and Microengineering,* vol. 17, no. 8, p. 1451, 2007.

[69]   Y. Shao, *Electrochemical cells: new advances in fundamental researches and applications.* BoD–Books on Demand, 2012.

[70]   B. N. Popov, J.-W. Lee, and M. B. Djukic, "Hydrogen permeation and hydrogen-induced cracking," in *Handbook of environmental degradation of materials*: Elsevier, 2018, pp. 133-162.

[71]   T. Wirtanen, T. Prenzel, J.-P. Tessonnier, and S. R. Waldvogel, "Cathodic corrosion of metal electrodes—how to prevent it in electroorganic synthesis," *Chemical Reviews,* vol. 121, no. 17, pp. 10241-10270, 2021.

[72]   S. Lynch, "Hydrogen embrittlement phenomena and mechanisms," *Corrosion reviews,* vol. 30, no. 3-4, pp. 105-123, 2012.

[73]   K. L. Tan and S. H. Yeo, "Cavitation erosion study in deionized water containing abrasive particles," in *Ann. DAAAM Proc. Int. DAAAM Symp*, 2015, vol. 26, no. 1, pp. 818-824.

[74]   S. Schmid *et al.*, "Effect of frequency and biofuel E85 on very high cycle fatigue behaviour of the high strength steel X90CrMoV18," *International Journal of Fatigue,* vol. 60, pp. 90-100, 2014.

[75]   H. Shen *et al.*, "Zr/ZrC modified layer formed on AISI 440B stainless steel by plasma Zr-alloying," *Applied Surface Science,* vol. 388, pp. 126-132, 2016.

[76]   "https://www.makeitfrom.com." (accessed 23.01.2023).

[77]   A. F. Torres, F. A. de Almeida, A. P. de Paiva, J. R. Ferreira, P. P. Balestrassi, and P. H. da Silva Campos, "Impact of stochastic industrial variables on the cost optimization of AISI 52100 hardened-steel turning process," *The International Journal of Advanced Manufacturing Technology,* vol. 104, no. 9, pp. 4331-4340, 2019.

[78]   W. Song, C. Drouven, and E. Galindo-Nava, "Carbon redistribution in martensite in high-C steel: Atomic-scale characterization and modelling," *Metals,* vol. 8, no. 8, p. 577, 2018.

[79]   *Operating instructions PEMCenter 8000*, 2011.

[80]   K. Chun, S. Kim, and E. Lee, "Analysis of the relationship between electrolyte characteristics and electrochemical machinability in PECM on invar (Fe-Ni) fine sheet," *The International Journal of Advanced Manufacturing Technology,* vol. 87, no. 9, pp. 3009-3017, 2016.

[81]   "https://www.csg-edelstahl.de/en/fertigungsverfahren/ecm."   (accessed 23.01.2023).

[82]   D. Bähre, A. Rebschläger, O. Weber, and P. Steuer, "Reproducible, fast and adjustable surface roughening of stainless steel using pulse electrochemical machining," *procedia CIRP,* vol. 6, pp. 384-389, 2013.

[83]   S. Loebel, M. Zinecker, P. Steinert, and A. Schubert, "Transient simulation of electrochemical machining processes for manufacturing of surface structures in high-strength materials," *Engineering Reports,* vol. 4, no. 7-8, p. e12360, 2022.

[84]   A. Elhoud, N. C. Renton, and W. F. Deans, "Hydrogen embrittlement of super duplex stainless steel in acid solution," *International journal of hydrogen energy,* vol. 35, no. 12, pp. 6455-6464, 2010.

[85] W. H. Johnson, "On some remarkable changes produced in iron and steel by the action of hydrogen and acids," *Nature,* vol. 11, no. 281, p. 393, 1875.

[86] Z. Shirband, M. R. Shishesaz, and A. Ashrafi, "Hydrogen degradation of steels and its related parameters, a review," *Phase Transitions,* vol. 84, no. 11-12, pp. 924-943, 2011.

[87] I. M. Robertson *et al.*, "Hydrogen embrittlement understood," *Metallurgical and Materials Transactions A,* vol. 46, no. 6, pp. 2323-2341, 2015.

[88] T. J. Carter and L. A. Cornish, "Hydrogen in metals," *Engineering Failure Analysis,* vol. 8, pp. 113-121, 2001.

[89] S. V. Brahimi, S. Yue, and K. R. Sriraman, "Alloy and composition dependence of hydrogen embrittlement susceptibility in high-strength steel fasteners," *Philosophical Transactions of the Royal Society A: Mathematical, Physical and Engineering Sciences,* vol. 375, no. 2098, p. 20160407, 2017.

[90] Q. Gao, "Investigations on Hydrogen Embrittlement of Advanced High Strength Steels for Automotive Applications," Dissertation, Rheinisch-Westfälischen Technischen Hochschule Aachen, 2017.

[91] J. Rehrl, "Wasserstoffversprödung in hochfesten, mikrolegierten Stählen," Dissertation, Technische Universität München, 2014.

[92] H.-J. Christ, M. Decker, and S. Zeitler, "Hydrogen diffusion coefficients in the titanium alloys IMI 834, Ti 10-2-3, Ti 21 S, and alloy C," *Metallurgical and Materials Transactions A,* vol. 31, no. 6, pp. 1507-1517, 2000.

[93] D. Rudomilova, T. Prošek, and G. Luckeneder, "Techniques for investigation of hydrogen embrittlement of advanced high strength steels," *Corrosion Reviews,* vol. 36, no. 5, pp. 413-434, 2018.

[94] S. K. Dwivedi and M. Vishwakarma, "Hydrogen embrittlement in different materials: A review," *International Journal of Hydrogen Energy,* vol. 43, no. 46, pp. 21603-21616, 2018.

[95] D. Ulutan, B. E. Alaca, and I. Lazoglu, "Analytical modelling of residual stresses in machining," *Journal of Materials Processing Technology,* vol. 183, no. 1, pp. 77-87, 2007.

[96] L. Wan *et al.*, "Hydrogen embrittlement controlled by reaction of dislocation with grain boundary in alpha-iron," *International Journal of Plasticity,* vol. 112, pp. 206-219, 2019.

[97] J. Wang, D. Zhang, B. Wu, and M. Luo, "Residual stresses analysis in ball end milling of nickel-based superalloy Inconel 718," *Materials Research,* vol. 20, pp. 1681-1689, 2017.

[98] N. Lyubenova *et al.*, "Impact of the Process Parameters, the Measurement Conditions and the Pre-Machining on the Residual Stress State of Deep Rolled Specimens," *Journal of Manufacturing and Materials Processing,* vol. 3, no. 3, p. 56, 2019.

[99] K. Lyon, T. Marrow, and S. Lyon, "Influence of milling on the development of stress corrosion cracks in austenitic stainless steel," *Journal of Materials Processing Technology,* vol. 218, pp. 32-37, 2015.

[100] M. Brown *et al.*, "Non-destructive detection of machining-induced white layers through grain size and crystallographic texture-sensitive methods," *Materials & Design,* vol. 200, p. 109472, 2021.

[101] M. Brown *et al.*, "Quantitative characterization of machining-induced white layers in Ti–6Al–4V," *Materials Science and Engineering: A,* vol. 764, p. 138220, 2019.

[102] B. Griffiths, "Mechanisms of white layer generation with reference to machining and deformation processes," *Journal of Tribology,* vol. 109/525, 1987.

[103] N. Zhou, "Influence of grinding operations on surface integrity and chloride induced stress corrosion cracking of stainless steels," Master thesis, KTH Royal Institute of Technology, 2016.

[104] A. Gomez-Gallegos, F. Mill, A. Mount, S. Duffield, and A. Sherlock, "3D multiphysics model for the simulation of electrochemical machining of stainless steel (SS316)," *The International Journal of Advanced Manufacturing Technology,* vol. 95, no. 5, pp. 2959-2972, 2018.

[105] M. L. Martin, M. J. Connolly, F. W. DelRio, and A. J. Slifka, "Hydrogen embrittlement in ferritic steels," *Applied physics reviews,* vol. 7, no. 4, p. 041301, 2020.

[106] J. Venezuela, Q. Liu, M. Zhang, Q. Zhou, and A. Atrens, "A review of hydrogen embrittlement of martensitic advanced high-strength steels," *Corrosion Reviews,* vol. 34, no. 3, pp. 153-186, 2016.

[107] B. Li, X. Zhang, and S. Zhang, "Microstructure investigation of dynamic recrystallization in hard machining: From thermodynamic irreversibility perspective," *Frontiers of Mechanical Engineering,* vol. 16, no. 2, pp. 315-330, 2021.

[108] Z. Yang *et al.*, "Multimodal microstructure and mechanical properties of AZ91 Mg alloy prepared by equal channel angular pressing plus aging," *Metals,* vol. 8, no. 10, p. 763, 2018.

[109] T. Tsuru, Y. Huang, M. R. Ali, and A. Nishikata, "Hydrogen entry into steel during atmospheric corrosion process," *Corrosion science,* vol. 47, no. 10, pp. 2431-2440, 2005.

[110] Z. Ahmad, *Principles of corrosion engineering and corrosion control*. Elsevier, 2006.

[111] K. Wienerová, M. Kouřil, and P. Novák, "Corrosion rate of cathodically" protected" steel in carbonate environment," *KOM–Corrosion and Material Protection Journal,* vol. 56, no. 1, pp. 15-18, 2012.

[112] "https://commons.wikimedia.org." (accessed 23.01.2023).

[113] A. Trautmann, G. Mori, M. Oberndorfer, S. Bauer, C. Holzer, and C. Dittmann, "Hydrogen uptake and embrittlement of carbon steels in various environments," *Materials,* vol. 13, no. 16, p. 3604, 2020.

[114] G. Comes and C. Cravero, "Theoretical modeling, design and simulation of an innovative diverting valve based on coanda effect," *Fluids,* vol. 3, no. 4, p. 103, 2018.

[115] A. Karimi and J. Martin, "Cavitation erosion of materials," *International Metals Reviews,* vol. 31, no. 1, pp. 1-26, 1986.

[116] E. Jurewicz, B. Gireń, and J. Steller, "Cavitation erosion–a possible cause of the mass loss within thrust zones in the Tatra Mts., Poland," *Acta Geologica Polonica,* vol. 57, no. 3, pp. 305-323, 2007.

[117] G. E. Totten *et al.*, "ASM Handbook W," *Materials Park, Ohio,* pp. 44073-0002, 2017.

[118] C. E. Banks and R. G. Compton, "Voltammetric exploration and applications of ultrasonic cavitation," *ChemPhysChem,* vol. 4, no. 2, pp. 169-178, 2003.

[119] A. Ruszaj, M. Zybura-Skrabalak, S. Skoczypiec, and R. Żurek, "Electrochemical machining supported by electrode ultrasonic vibrations," in *13th International Symposium for Electromachining, ISEM, Spain, May*, 2001, pp. 9-11.

[120] J. Wisniak, "The history of mercury. From discovery to incommodity," *Revista CENIC. Ciencias Químicas,* vol. 39, no. 3, pp. 147-157, 2008.

[121] H. Davy, "II. The Bakerian Lecture for 1809. On some new electrochemical researches, on various objects, particularly the metallic bodies, from the alkalies, and earths, and on some combinations of hydrogene," *Philosophical Transactions of the Royal Society of London,* no. 100, pp. 16-74, 1810.

[122] C. Reed, "A remarkable electrolytic phenomenon," *Journal of the Franklin Institute,* vol. 139, no. 4, pp. 283-286, 1895.

[123] G. Bredig and F. Haber, "Ueber Zerstäubung von Metallkathoden bei der Elektrolyse mit Gleichstrom," *Berichte der deutschen chemischen Gesellschaft,* vol. 31, no. 3, pp. 2741-2752, 1898.

[124] F. Haber, "Über Legierungspotentiale und Deckschichtenbildung; zugleich ein Nachtrag zu der Mitteilung¨ber Kathoden-Auflockerung und Zerstäubung," *Zeitschrift für Elektrochemie,* vol. 8, no. 32, pp. 541-552, 1902.

[125] M. Sack, "Über die Entstehung und Bedeutung von Natriumlegierungen bei der kathodischen Polarisation," *Zeitschrift für anorganische Chemie,* vol. 34, no. 1, pp. 286-352, 1903.

[126] B. Kabanov, I. Astakhov, and I. Kiseleva, "Formation of crystalline intermetallic compounds and solid solutions in electrochemical incorporation of metals into cathodes," *Electrochimica Acta,* vol. 24, no. 2, pp. 167-171, 1979.

[127] I. Leontyev, A. Kuriganova, Y. Kudryavtsev, B. Dkhil, and N. Smirnova, "New life of a forgotten method: Electrochemical route toward highly efficient Pt/C catalysts for low-temperature fuel cells," *Applied Catalysis A: General,* vol. 431, pp. 120-125, 2012.

[128] W. Huang, S. Chen, J. Zheng, and Z. Li, "Facile preparation of Pt hydrosols by dispersing bulk Pt with potential perturbations," *Electrochemistry communications,* vol. 11, no. 2, pp. 469-472, 2009.

[129] J. Liu, W. Huang, S. Chen, S. Hu, F. a. Liu, and Z. Li, "Facile electrochemical dispersion of bulk Rh into hydrosols," *Int J Electrochem Sci,* vol. 4, no. 9, pp. 1302-1308, 2009.

[130] A. I. Yanson, P. Rodriguez, N. Garcia-Araez, R. V. Mom, F. D. Tichelaar, and M. T. Koper, "Cathodic corrosion: a quick, clean, and versatile method for the synthesis of metallic nanoparticles," *Angewandte Chemie International Edition,* vol. 50, no. 28, pp. 6346-6350, 2011.

[131] P. Strasser, M. Gliech, S. Kuehl, and T. Moeller, "Electrochemical processes on solid shaped nanoparticles with defined facets," *Chemical Society Reviews,* vol. 47, no. 3, pp. 715-735, 2018.

[132] H. Salzberg and F. Mies, "Cathodic disintegration of tin," *Journal of The Electrochemical Society,* vol. 105, no. 2, p. 64, 1958.

[133] L. Gastwirt and H. Salzberg, "Disintegration of Lead Cathodes, II," *Journal of The Electrochemical Society,* vol. 104, no. 12, p. 701, 1957.

[134] H. W. Salzberg, "Cathodic lead disintegration and hydride formation," *Journal of The Electrochemical Society,* vol. 100, no. 4, p. 146, 1953.

[135] B. N. Kabanov, I. I. Astakhov, and I. Kiseleva, "Electrochemical implantation of alkali metals," *Russian Chemical Reviews,* vol. 34, no. 10, p. 775, 1965.

[136] B. Kabanov, "Incorporation of alkali metals into solid cathodes," *Electrochimica Acta,* vol. 13, no. 1, pp. 19-25, 1968.

[137] P. Rodriguez, F. D. Tichelaar, M. T. Koper, and A. I. Yanson, "Cathodic corrosion as a facile and effective method to prepare clean metal alloy nanoparticles," *Journal of the American Chemical Society,* vol. 133, no. 44, pp. 17626-17629, 2011.

[138] U. Gangal, M. Srivastava, and S. K. S. Gupta, "Mechanism of the breakdown of normal electrolysis and the transition to contact glow discharge electrolysis," *Journal of the Electrochemical Society,* vol. 156, no. 10, p. F131, 2009.

[139] L. Chiacchiarelli, Y. Zhai, G. Frankel, A. Agarwal, and N. Sridhar, "Cathodic degradation mechanisms of pure Sn electrocatalyst in a nitrogen atmosphere," *Journal of Applied Electrochemistry,* vol. 42, no. 1, pp. 21-29, 2012.

[140] M. Kliškić, J. Radošević, and S. Gudić, "Yield of hydrogen during cathodic polarisation of Al–Sn alloys," *Electrochimica acta,* vol. 48, no. 28, pp. 4167-4174, 2003.

[141] W. Huang, L. Fu, Y. Yang, S. Hu, C. Li, and Z. Li, "Simultaneous fabrications of nanoparticles and 3D porous films of Sn or Pb from pure electrodes," *Electrochemical and Solid-State Letters,* vol. 13, no. 5, p. K46, 2010.

[142] T. J. Hersbach, I. T. McCrum, D. Anastasiadou, R. Wever, F. Calle-Vallejo, and M. T. Koper, "Alkali metal cation effects in structuring Pt, Rh, and Au surfaces through cathodic corrosion," *ACS applied materials & interfaces,* vol. 10, no. 45, pp. 39363-39379, 2018.

[143] T. J. Hersbach and M. T. Koper, "Cathodic corrosion: 21st century insights into a 19th century phenomenon," *Current Opinion in Electrochemistry,* vol. 26, p. 100653, 2021.

[144] D. S. Patel, V. Sharma, V. Jain, and J. Ramkumar, "Sustainable electrochemical micromachining using atomized electrolyte flushing," *Journal of The Electrochemical Society,* vol. 168, no. 4, p. 043504, 2021.

[145] C. Vargel, *Corrosion of aluminium.* Elsevier, 2020.

[146] C. Örnek, C. Leygraf, and J. Pan, "On the Volta potential measured by SKPFM–fundamental and practical aspects with relevance to corrosion science," *Corrosion Engineering, Science and Technology,* vol. 54, no. 3, pp. 185-198, 2019.

[147] S. Esmailzadeh, M. Aliofkhazraei, and H. Sarlak, "Interpretation of cyclic potentiodynamic polarization test results for study of corrosion behavior of metals: a review," *Protection of metals and physical chemistry of surfaces,* vol. 54, no. 5, pp. 976-989, 2018.

[148] H. Wan, Y. Cai, D. Song, and C. Chen, "Effect of Cr/Mo carbides on corrosion behaviour of Fe_Mn_C twinning induced plasticity steel," *Corrosion Science,* vol. 167, p. 108518, 2020.

[149] X. Zhang *et al.*, "The influence of stored energy on grain boundary chemistry and intergranular corrosion development in AA2024-T3 alloy," *Materials,* vol. 11, no. 11, p. 2299, 2018.

[150] R. Avci, B. H. Davis, N. Rieders, K. Lucas, M. Nandasiri, and D. Mogk, "Role of metallurgy in the localized corrosion of carbon steel," *Journal of Minerals and Materials Characterization and Engineering,* vol. 6, no. 6, pp. 618-646, 2018.

APPENDIX

DRAWN
m.ghasemiansafaei | 12/5/2019

CHECKED

QA

MFG

APPROVED

Norm | mm

TITLE
Part 1 in Figure 5-9, Figure 5-10, Figure 5-11, and Figure 5-12

Allgemeintoleranze: ISO 2768-fH
Amount: 1X
Material: 1.4571

SIZE A4 | DWG NO | REV

SCALE 1 : 1 | SHEET 1 OF 1

35.00
105.00
20.00
R1.00
R1.00
M6
20.00
13.98

Part 2 in Figure 2-21, Figure 2-23, Figure 5-11, and Figure 5-12
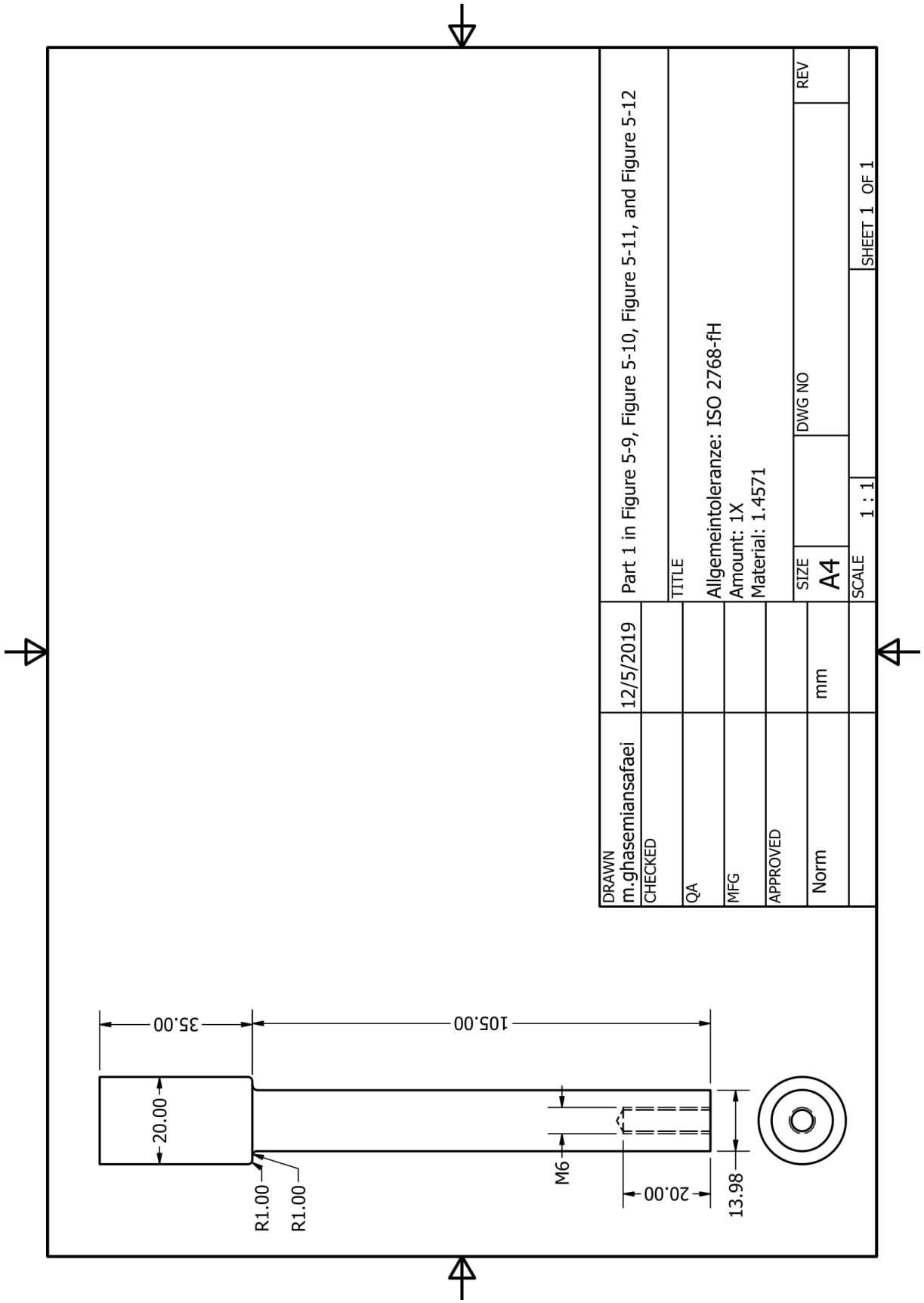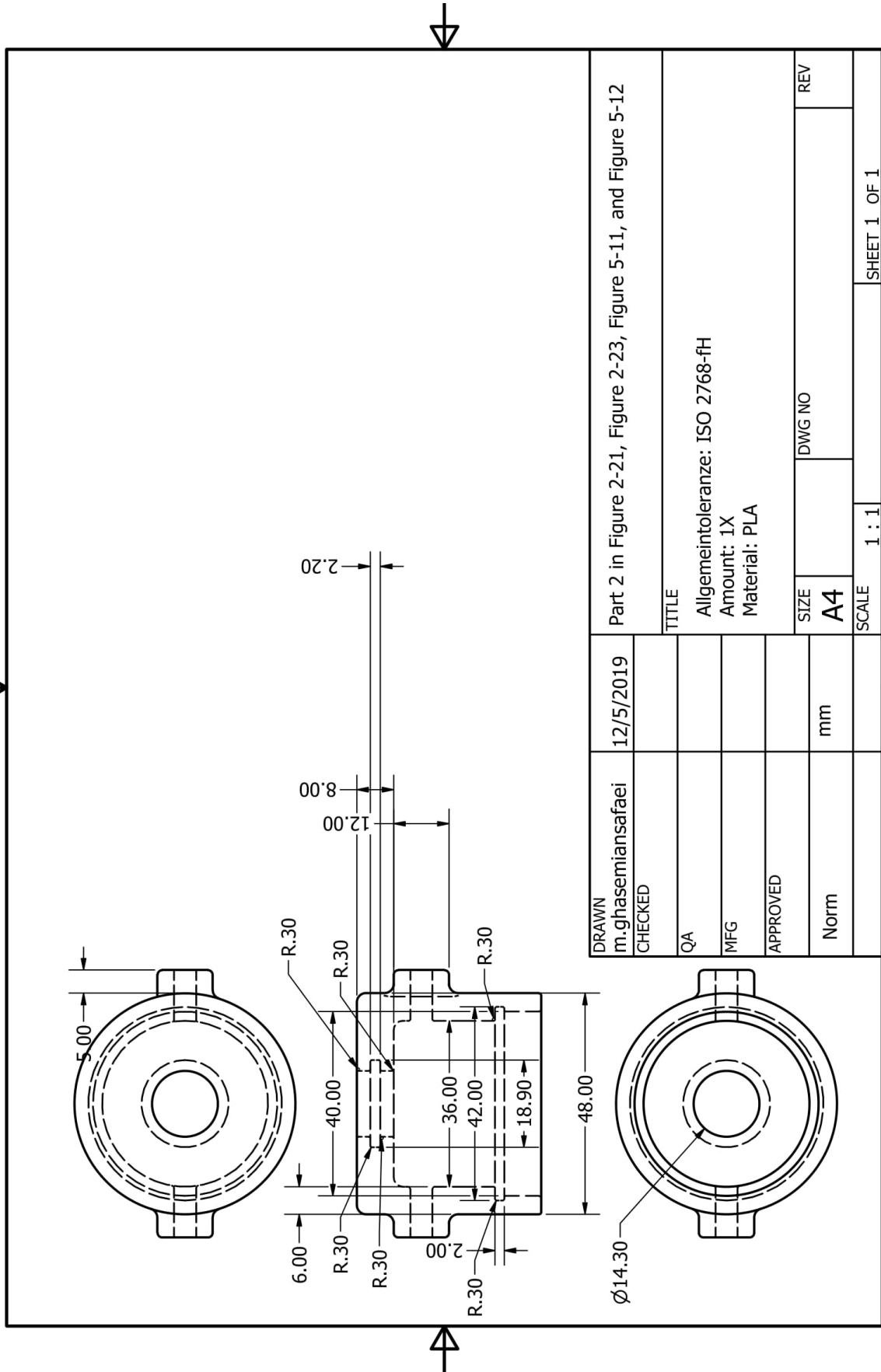
DRAWN m.ghasemiansafaei	12/5/2019		Part 2 in Figure 2-21, Figure 2-23, Figure 5-11, and Figure 5-12		REV
CHECKED		TITLE			
QA		Allgemeintoleranze: ISO 2768-fH Amount: 1X Material: PLA			
MFG					
APPROVED				DWG NO	
Norm	mm	SIZE A4			SHEET 1 OF 1
		SCALE 1 : 1			

Part 3 in Figure 2-21, Figure 2-22, Figure 2-23, Figure 5-11, and Figure 5-12

TITLE

Allgemeintoleranze: ISO 2768-fH
Amount: 1X
Material: 1.4571

DRAWN	12/3/2022		DWG NO		REV
Mandana					
CHECKED					
QA					
MFG					
APPROVED		SIZE A4			
Norm	mm	SCALE 1 : 1		SHEET 1 OF 1	

Ø42,00

Ø22,00

R31,00

14,00

5,00

10,00

10,00

70,00

M6

M6

Part 4 in Figure 2-21, Figure 2-23, Figure 5-9, Figure 5-11, and Figure 5-12

Allgemeintoleranze: ISO 2768-fH
Amount: 5X
Material: 1.4112

Ø20.00
Ø14.00
M6Ø4.92
Ø8.00
45.0°
5.00
7.00
2.00
3.00

DRAWN m.ghasemiansafaei	4/29/2019	TITLE	REV
CHECKED			
QA			
MFG		DWG NO	
APPROVED			
Norm	mm	SIZE A4	
		SCALE 3 : 1	SHEET 1 OF 1

Part 5 in Figure 5-21, Figure 2-22, Figure 2-23, Figure 5-9, Figure 5-11, and Figure 5-12

TITLE

Allgemeintoleranze : ISO2768-fH

Amount: 1X

Material: 1.3505

DRAWN	4/3/2019		REV
m.ghasemiansafaei			
CHECKED			
QA		DWG NO	
MFG			
APPROVED			
Norm	mm	SIZE A4	SHEET 1 OF 1
		SCALE 1 : 1	

Ø40.00

Ø18.00

65.00

65.00

Part 6 in Figure 2-22, and Figure 2-23

Allgemeintoleranze : ISO2768-fH
Amount: 1X
Material: 1.4571

Part 7 in Figure 5-7

DRAWN Mandana	6/23/2021	TITLE		
CHECKED		Allgemeintoleranze: Iso 2768-fH		
QA		Amount: 1X		
MFG		Material: PVC		
APPROVED		Unit: mm		
		SIZE A4	DWG NO	REV
		SCALE 1 / 2		SHEET 1 OF 1

Ø15,00
8,50
Ø100,00
Ø80,00
10,00
80,00
14,00
1,00
R2,00
22,00

Part 8 in Figure 2-21, and Figure 2-23,

TITLE

Allgemeintoleranze: ISO 2768-fH
Unit: mm
Menge: 1X
Material: 1.4571

DRAWN
Mandana 1/25/2022
CHECKED
QA
MFG
APPROVED

REV

DWG NO

SIZE A4

SCALE 1 : 1

SHEET 1 OF 1

ØM4
4,00
Ø14,00 K6
ØM6
20,00
145,00

Part 9 in Figure 5-10, Figure 5-11, and Figure 5-12

TITLE

Allgemeintoleranze: ISO 2768-fH
Unit: mm
Menge: 1X
Material: PVC

DRAWN
Mandana
1/25/2022
CHECKED
QA
MFG
APPROVED

SIZE
A4

DWG NO

SCALE 1 / 2

REV

SHEET 1 OF 1

Ø62,00 H7
Ø50,00 H7
Ø12,00 H7
Ø70,00

10,00
60,00
30,00
10,00
80,00

Part 10 in Figure 5-10, and Figure 5-12

TITLE

Allgemeintoleranze: ISO 2768-fH
Unit: mm
Menge: 1X
Material: PVC

DRAWN
Mandana
CHECKED

QA

MFG

APPROVED

1/24/2022

SIZE
A4

DWG NO

REV

SCALE 1 : 1

SHEET 1 OF 1

DRAWN Mandana | 1/25/2022

CHECKED

QA

MFG

APPROVED

TITLE: Part 11 in Figure 5-10, and Figure 5-12

Allgemeintoleranze: ISO 2768-fH
Unit: mm
Menge: 1X
Material: PVC

SIZE A4 | DWG NO | REV

SCALE 1 : 1 | SHEET 1 OF 1

Ø50,00 k6

Ø14,00 H7

15,00

Part 12 in Figure 5-11, and Figure 5-12

TITLE

Allgemeintoleranze: ISO 2768-fH
Unit: mm
Material: 1.4571

DRAWN | Mandana | 4/12/2022
CHECKED
QA
MFG
APPROVED

SIZE A4

DWG NO

REV

SCALE 3 : 1

SHEET 1 OF 1

20,00   15,00

ØM6   Ø6,00 k6

Part 13 in Figure 5-11, and Figure 5-12

TITLE
Allgemeintoleranze: ISO 2768-fH
Unit: mm
Material: PVC

DRAWN	Mandana	4/12/2022
CHECKED		
QA		
MFG		
APPROVED		

SIZE **A4**

DWG NO

REV

SCALE 3 : 1

SHEET 1 OF 1

Ø10,00 p7
Ø6,00 H7
20,00

TITLE: Part 14 in Figure 5-11, and Figure 5-12

Allgemeintoleranze: ISO 2768-fH
Unit: mm
Menge: 1X
Material: 1.4571

SIZE	DWG NO	REV
A4		
SCALE 1 : 1		SHEET 1 OF 1

DRAWN Mandana 1/25/2022
CHECKED
QA
MFG
APPROVED

Ø40,00
Ø60,00
Ø30,00

30,00
ØM6
10,00
21,00
5,00
8,00
M6
Ø10,00
15,00
10,00 5,00